1C02C

PEER Project 1C02, Task 1: Earthquake ground motion

Validation of 1-D Numerical Simulation Procedures of the 1999 Turkey and Taiwan earthquakes

Final Technical Report

August 29, 2002

Yuehua Zeng
Seismological Lab, University of Nevada - Reno

Introduction

As part of the PEER lifeline projects, our goal is to develop a new near-field attenuation relation that includes effect of rupture directivity using both synthetic and observed near-field ground motion data. Before applying any synthetics to the regression analysis, the procedures for synthetic calculation need to be thoroughly validated through comparison between synthetic simulations with observations of passed earthquakes. The objective of this study is to continue validating our numerical and simulation methods for ground motion calculation using the composite source model. The validation will use strong ground motion data of the 1999 Turkey and Taiwan earthquakes. We will first determine specific composite source models for those earthquakes that match the long period velocity records wiggle for wiggle and the resulting slip distribution of those source models will be consistent with that obtained in other inversions. Based on those specific composite source models, we will predict the broadband strong ground motions at given sites with recorded accelerograms. As part of the validation, we will determine the statistical parameters of the models to best match the observed near-field ground accelerations.

Over the past years, we have focused our efforts to develop and improve the numerical simulation procedure to compute synthetic strong motion seismogram using a composite source model (Zeng et al., 1994). The method has been successful in generating realistic strong motion seismograms. The realism is demonstrated by comparing synthetic strong motions with observations from the recent California earthquakes at Landers, Loma Prieta (Su et al., 1994a,b, Zeng and Anderson, 2000) and Northridge (Zeng and Anderson, 1996; Anderson and Yu, 1996; Su et al., 1998), earthquakes in the eastern US (Ni et al., 1999) and earthquakes in Guerrero, Mexico (Zeng et al., 1994; Johnson, 1999), Turkey (Anderson et al., 2001) and India (Khattri et al, 1994; Zeng et al, 1995). We have also successfully applied the method for earthquake engineering applications to compute the ground motion of scenario earthquakes. During the process of continuing development, we have included scattering waves from small scale heterogeneity structure of the earth, site specific ground motion prediction using weak motion site amplification, and nonlinear soil response using the geotechnical engineering model. In one

of our previous PEER research projects, we evaluated the numerical procedure for simulating near-fault long-period ground motions and rupture directivity. In that study, we revisited the earthquake events, including Loma Prieta, Landers and Northridge. We also tested its ability to predict the near-fault ground motion observation from the 1979 Imperial Valley earthquake and the 1995 Kobe event (Zeng and Anderson, 2000).

The Kocaeli, Turkey and Chi-Chi, Taiwan earthquakes were the two largest events in 1999. Both were very well recorded by dense strong motion arrays, especially the Chi-Chi event. The wealth of ground motion data from these two earthquakes has provided us the opportunity to further calibrate our near-field strong ground motion simulation procedure, and to understand the relation between the composite source model parameters and the observed high-frequency source radiation for large earthquakes. In addition, the ground deformations of these two earthquakes were well recorded by GPS measurements. This provides additional constraints to our source modeling and ground motion simulation.

Method

Composite Source Model

We developed a composite source model (Zeng et al., 1994) for realistic synthetic ground motion computation. The method uses synthetic Green's functions, which characterize wave propagation in a flat-layered medium, convolved with the composite source time functions. The source is a superposition of circular subevents with constant stress drop. The number of subevents and their radius follows a power law given by

$$\frac{dN}{d(\ln R)} = pR^{-D} \tag{1}$$

where D is the fractal dimension that equals twice the b-value, N is the number of subevents, and p is a constant of proportionality. The random nature of the heterogeneities on a complex fault is achieved by distributing the subevents randomly on the fault plane. Rupture propagates from the hypocenter, and each subevent radiates a displacement pulse of a crack model when rupture front reaches the subevent. The heterogeneous nature of the composite earthquake faulting is apparently characterized by the maximum subevents size, the subevents stress drop and subevents rupture velocity, which can be constrained by other independent geophysical data.

For the displacement pulse radiated from each subevent, we first modeled it as a Brune's pulse (Zeng et al., 1994) and then substituted it by a Sato and Hirasawa's circular crack pulse (Zeng and Anderson, 1996) to take into account of the long period rupture directivity. Recently, we introduced an asymmetric circular rupture to improve the subevent source radiation (Zeng, 2001). This asymmetric circular rupture assuming the Eshelby's (1957) elastic circular crack solution under uniform shear stress at every successive instant of rupture. Instead of assuming a symmetrical growing crack nucleated from the center of the crack (Sato and Hirasawa, 1973), Zeng (2001) hypothesized that rupture breaks at any given location inside the crack. The rupture velocity at any point inside the crack depends on the azimuth angle between the axis connecting the nucleation location to the point and the axis connecting the nucleation location to the center of the crack. Obviously the solution of the the Sato and Hirasawa's symmetric growing crack model is a special case of this asymmetic circular rupture when rupture nucleates at the center of the crack. The resulting ground motion calculated using this improved subevent ruptures gives

better rupture directivity than our previous study in comparison with the observation from Landers, Loma Prieta, Northridge, Imperial Valley and Kobe earthquakes. This is done by using the near-fault directivity model of Somerville et al. (1997) to test the synthetic prediction of the rupture directivity effect of those earthquake ground motions in terms of fault normal and fault parallel components.

The synthetic Green's function has been modified to consider the effect of the random lateral heterogeneity of the earth by adding scattered waves into the Green's function (Zeng, 1995). The solution is then convolved with a plane wave propagation function through a near surface 1-D velocity layering as complex as that suggested by sonic well logs. Thus the complex high-frequency waveform of our simulation is generated from a combination of a heterogeneous source (Figure 1a), wave reverberation in a stratified crustal structure (Figure 1b) and scattering from lateral inhomogeneity of the earth (Figure 1c).

Earthquake source Imaging Using Genetic Algorithm

Zeng and Anderson (1996) used a genetic algorithm to find a specific composite source model that best fit the observed waveform data for the Northridge earthquake. The Genetic Algorithm works by mimicking the process of natural selection principle of survival of the fittest. By analogy with the natural behavior, it starts with an initial "population" of "individuals" (e.g., models of the subevent locations, subevent rupture velocity, etc), each representing a possible solution. A fitness score is assigned to each individual. Individuals with higher fitness are given better opportunities to "crossbreed" with others in the population to produce "offspring" that form a new population the same size as the original. The algorithm iterates by taking those offspring as a new generation and repeats the process until a satisfactory solution is obtained.

Following Zeng and Chen (2001), the modified fitness function for strong motion waveform inversion is defined as,

$$F(m^i) = \sum_{Stations}\left[\sum_{components}\frac{\min(\dot{u}^o_{\max},\dot{u}^s_{\max})}{\max(\dot{u}^o_{\max},\dot{u}^s_{\max})}\frac{\sum_l \dot{u}^o_l \dot{u}^s_l}{\sqrt{\sum_l \dot{u}^o_l \dot{u}^o_l}\sqrt{\sum_l \dot{u}^s_l \dot{u}^s_l}} - \delta\left|\log\frac{\dot{u}^s_{\max}}{\dot{u}^o_{\max}}\right|\right] \quad (2)$$

where m^i is the ith model; $\dot{u}^o_l$, l = 1, 2, ..., is the observed velocity seismogram; $\dot{u}^s_l$, l = 1, 2, ..., is the corresponding synthetic velocity seismogram; $\dot{u}^o_{\max}$ and $\dot{u}^s_{\max}$ are the peak velocities of the observed and synthetic seismograms, respectively. The first term on the right-hand side of equation (2) is a weighted cross-correlation coefficient between observed and synthetic seismograms. The weight penalizes the cross-correlation coefficient when the synthetics and observations have similar waveforms but different amplitudes. The disadvantage of such a weight is that the inversion sometimes conveniently maximizes this amplitude difference when it is difficult to match the phases of the waveforms. To overcome this, we introduce a second term, $\delta\left|\log(\dot{u}^o_{\max}/\dot{u}^o_{\max})\right|$, in equation (2) to improve our original weighting procedure. The fitness function for the static GPS data inversion uses a simple l-1 norm. Since the static deformation decays rapidly with distance, the l-1 norm improves weighting to distant stations than that using the least squares function, thus provides better resolutions for source image at larger depth.

After we compute a fitness value for each individual, we start the next phase of crossbreed to produce offspring. We pick two individuals as "parents" for a reproduction event using the so-called roulette wheel selection scheme. The two parents are used to generate two offspring by recombining their "chromosomes" using the mechanisms of cross-over and mutation. The chromosomes in our case are the subevent locations and subevent rupture velocities, subfault rakes and rupture times. The subevents of both models are divided randomly into 10 groups, and their chromosomes are copied into their offspring according to a randomly generated "cross-over mask". Mutation is applied to each offspring individually after cross-over. It is done by randomly altering the chromosomes of each subevent with a probability of 0.01.

Kocaeli, Turkey Earthquake

Earthquake information and data analysis

The Kocaeli, Turkey earthquake (Mw7.4) occurred on Aug. 17, 1999. The event ruptured the North Anatolian Fault Zone, one of the most prominent active fault in Turkey and source of numerous large earthquakes throughout the history. The earthquake was located at an epicenter of 40.70°N and 29.91°E (the Earthquake Research Department of the Directorate for Disaster Affairs of the Ministry of Public Works, Turkey). The focal depth is about 15.9 km. Field observations suggest that the earthquake ruptured for over 140 km from Golcuk to Melen and produced surface breaks up to 4 or 5 m along its eastern section of the epicenter. The earthquake was particularly destructive because the fault ruptured through densely developed urban areas and resulted in over 15,000 fatilities. The estimated economic losses have exceeded $16 billion of US dollars.

The North Anatolian fault in Turkey is a good analog of the San Andreas fault system in California. Understanding the characteristics of the Kocaeli source rupture will undoubtedly improves our ability to predict the ground motion of this sized earthqukae should it occurs on the San Andreas. Aftershock activity of the Kocaeli earthquake has been located in an east-west region bounded by 40.5~40.8N and 28.8~31.2E (Figure 2), thus extending bilaterally from the epicenter. Preliminary observations of the surface faulting, however, suggest that the fault rupture was predominantly unilateral towards the east. Figure 3 shows the surface trace of the earthquake fault model used for this study. The surface trace was modified from the fault model of Reilinger et al. (2000). The pink circles and blue triangles are GPS and strong motion stations, respectively. We used 51 3-component GPS measurements and 11 strong motion waveform records for this investigation. Table 1 lists the names and locations of those strong motion stations. By carefully examing the strong motion records near the fault, we find that there are some very strong low-frequency pulses, which may have been caused by some component of the rupture going towards the station. For example, the Izmit station shows some very strong low-frequency pulses on the horizontal components. In Sakarya, there was about 10 seconds of strong motion which occurred as the rupture propagated past the station. The record from Duzce may have maximum directivity, as it is near the east end of the rupture. A second pulse, roughly 30 seconds after the first burst of energy, is a relatively inconsequential aftershock since it does not have significant amounts of low frequency energy and is very small on the velocity and displacement records. In general, peak accelerations are no larger than about 30-40% of gravity. The distribution of stations along the fault is relatively sparse, but the data is of enormous significance, sampling strong ground motion of the rupture at several intervals along the fault.

Table 1

Station names and locations for the Kocaeli earthquake

Name	Latitude	Longitude	Site Class
ARC	29.3607	40.8236	B
BRS	29.131	40.183	A
CNA	28.7594	41.0238	D
DZC	31.1489	40.8437	D
GBZ	29.4494	40.7862	A
GYN	30.784	40.385	B
DHM	28.8199	40.9823	D
IST	29.013	41.058	B
IZT	29.9175	40.7664	A
IZN	29.7172	40.4416	D
SKR	30.3793	40.7372	B
YPT	29.762	40.7639	D

The static deformation data for this inversion study was obtained from the GPS observation made available at the Burgmann's website at the University of California, Berkeley. The strong motion data was collected from USGS (Celebi et al., 2001) and PEER strong motion database. We filtered all the seismograms using a 4^{th} order non-causal Butterworth filter with a passband specified between 0.1 to 0.8 Hz. The S-wave arrival times of the strong motion records were picked and matched with the theoretical calculations based on a flat-layered crustal velocity model of the region. The crustal velocity model was modified from Sekiguchi and Iwata (2002). The modification reduces the number of layers in the original model by grouping several middle crustal layers into fewer layers. We also modified the velocity structure of the top layer at station SKR and YPT according to the study of array observations of microtremors and aftershocks by Kudo et al. (2002). Based on those models, we calculated the Green's function at low frequency with the same frequency bandwidth applied to the data analysis and compute the source inversion to determine the source rupture process of the Kocaeli earthquake.

Earthquake Source Inversion and Discussion

For the Kocaeli earthquake, we have constructed the rupture fault according to the surface trace (Figure 3) modified from Reilinger et al. (2000). The fault extends for a total of 160 km in length and 20 km in depth with a 90^{o} dipping angle. Rupture nucleated from the hypocenter at a depth of 15.9 km and propagated bilaterally along the fault at an initial rupture velocity of 3.0 km/sec. For each subfault, we assume a variable rake for the slip and a rupture time delay Δt relative to the time derived from the shortest distance to the hypocenter along the fault plane divided by a constant rupture velocity of 3.0 km/sec. The rake was constrained within a range of 180 ± 45 degree. The rupture time delay Δt varies from -3 to 3 second. The rise time is modeled by allowing each subevent with a variable subevent rupture velocity ranging from 0.5 to 2.0 km/sec. The range of the subevent rupture velocity was chosen by a trial and errors approach to fit the synthetic ground motion velocity pulses to the observations. For the composite source model, we have determined the maximum subevent radius as 6.0 km and subevent stress drops of 50 bars after some trail and errors. The total seismic moment of this earthquake is estimated to be 2.1×10^{27} dyne-cm.

Using the genetic algorithm, we inverted the combined GPS ground deformation and strong motion waveform data to obtain the source rupture processes of the Kocaeli earthquake. Figure 4 plots the earthquake slip distribution of the composite source model, the slip vector distribution, and the rupture time distribution over the fault plane. The result indicates a complex earthquake rupture process. Most slip occurred above a depth of 15 km. This is very similar to large earthquake ruptures that have occurred in California. There is a large slip zone to the west of the hypocenter at distances ranging from 10 to 25 km. Another large slip zone occurred to the east of the hypocenter at distances ranging from 15 to 50 km. Over all the slip is dominated by right-lateral strike slip mechanism with slight change in rake angle. There are significant normal slip components at distances ranging from 20 to 35 km. This appears at place when fault starts to bend slightly southeast. Simple stress analysis indicates that the geometrical bending has resulted in a pull-apart fault zone and an increase in tensional stress. The location also coincides with a supershear rupture zone near the SKR station. At distance of 60 km east of the hypocenter, there is a larger fault bending northeast. Rupture diminished to nearly zero slip amplitude. Slip picked up again when rupture propagated through this geometrical barrier. Thus it appears that the fault geometrical irregularity has contributed significantly to the complexity in fault slip distribution and rupture velocity distribution.

Figure 5 compares the synthetic static ground deformations computed using the source model determined from the inversion solution. It is seen that the synthetic deformations agree very well with the observation for all stations. Figure 6 compares the synthetic and observed ground velocity waveforms. The traces within each panel correspond to different components of velocity seismograms. The observed seismograms are plotted above the synthetics for each station. The peak velocities (in cm/sec) are shown to the right of the seismograms followed by their station names and the orientation (in degrees) of components measured from north. There are some discrepancies in the north-south direction for station DZC and GNY. For all other stations, the synthetic waveforms match very well with the observed waveforms. The improvement to the final fitness function for the waveform inversion is above 54% over the average value of the fitness functions calculated from the starting models.

High Frequency Analysis

In order to take into account of the site effect for the broadband ground motion simulation, the synthetics were then propagated through a 30 meters low velocity soil layer on top of the original velocity models to accommodate the site response at each station. We have used DESRA2 program (Lee and Finn, 1982) to compute the soil response. When the amplitude of the ground motion is high, it will result in non-linear site response. The parameters for determining the possible nonlinear site response are specified according to EPRI (1993) guideline for soil properties. The site classifications for all strong motion stations are provided by Silva (2002, personal communication) and were listed in Table 1. The average shear wave velocity of the top 30 meters surface layer is assigned according to the USGS published site classification using shear wave velocities.

Based on the inversion solution, we have extrapolated the waveform calculation to a frequency range up to 25 Hz. The result shows an overall underestimation of the high frequency radiation. As we have mentioned earlier, the rupture velocity for the subevent of the composite source model varies from 0.5 to 2.0 km/sec. This can be translated into a subevent rise time ranging from 2 to 12 seconds for subevents with radii of 1.0 to 6.0 km. For the several large slip zones, the rise time of the inversion is estimated around 10 seconds. As a result of this long rise

time and slow rupture of the subevent, it generates very low high frequency amplitudes. In order to overcome this problem, we have introduced a variable rupture velocity model for the subevent of the composite sources. For example, a subevent rupture velocity increase with time will produce basically the same low frequency waveform but higher amplitude for the high frequency radiation. By trial and errors, we found that an increase of subevent rupture velocity from v_1 to v_2, where v_1 varies from 0.5 to 2.0 km/sec and v_2=2.0 km/sec, produces enough high frequency energies that the final simulations are unbiased through the entire frequency band. Figure 7 plots the misfit between the observation and synthetic prediction for the horizontal components and the vertical component (including Duzce earthquake). The misfit is quantified based on biases and standard errors. The middle line in each top panel shows the biases versus periods with the 90% confidence limits envelopes of the biases. The standard errors are plotted in the lower panel. Average errors are 0.52 and 0.55 for the horizontal and vertical components, respectively.

Figure 8 compares the observed and synthetic ground acceleration, velocity and displacement at station SKR. The synthetics agree quite well with the observations. Figure 9 plots the comparison of acceleration time history and their Fourier amplitude between the synthetics and the observation for all stations. For each component, the synthetic seismograms are plotted below the observation. The observed spectra are plotted in solid line and the synthetics are in dotted lines. In general, the synthetic accelerations agree with the observation in their peak values and duration, so the composite source model indeed does a very good job in describing a broadband earthquake source processing. A further improvement of the synthetic strong motion accelerograms is to consider 3-D velocity structure to simulate potential basin response at some stations.

Chi-Chi, Taiwan Earthquake

Earthquake information and data analysis

The September 21, 1999 Chi-Chi, Taiwan earthquake (M_w=7.6) and subsequent large aftershocks (Mw>6) were well recorded by a dense strong motion network operated by the Central Weather Bureau of Taiwan (CWB). These are the best-recorded seismic events of any modern disastrous earthquakes. The mainshock was recorded at more than 700 strong motion stations across the island with 65 near-field (<20 kilometers from the epicenter) ground motion records. Tremendous ground deformation associated with this earthquake faulting caused major destruction to buildings and lifelines across a wide area of Taiwan. The large inland thrust caused a ground deformation of up to 9 meters and ground velocity above 3 m/sec. The wealth of ground motion data that resulted from this earthquake sequence has provided us a good opportunity to understand the near-field ground deformation and ground motions of large thrusting earthquake and to model the source rupture processes.

The epicenter of the Chi-Chi earthquake is located at 23.78N and 120.81E, near the town of Chi-Chi in the western part of Taiwan. The earthquake rupture was associated with the Chelungpu fault, and nucleated at a depth of 7 km. The fault trace extends for more than 90 km, in a nearly NS direction, but changes course to nearly EW trend at its northern end. The fault plane is mainly an east-dipping thrust with significant left-lateral strike-slip component. Field observations demonstrate that the earthquake ruptured all the way to the surface. The slip at the surface was enormous, up to 9 meters or more in someplaces. It has formed a new waterfall on a major river coming out of the mountains and crossing the fault. Besides the mainshock, over 12

aftershocks greater than magnitude 6.0 occurred in the area. Figures 10 shows examples of the strong motion records from the mainshock. Recordings near the epicenter area show more high frequency energy than recordings near the northern end of the rupture zone. The ground displacement on the hanging wall appears much larger than that on the footwall. There are many stations on the hanging wall that recorded the strong motion of the mainshock. Those are extremely valuable records for earthquake engineering study to compare near ground motion between the hanging wall and footwall. They are also important for earthquake source study as the data are less contaminated by effect of wave propagation in the complicated structures of the sedimentary basin west of the fault trace.

Data and Model

For the Chi-Chi mainshock, the surface break was well mapped by the Taiwan Central Geological Survey along the Chelungpu fault. According to their surface rupture data, we have constructed a 3-D fault model. Figure 11 shows the observed fault surface trace and the surface trace distribution of the fault model (red line). The fault model consists of eight segments. The total rupture length of those segments at the surface is 96 km. The fault width extends 40 km down dip. The fault dips overall at 27.5° to the east. We divide the fault into 4 km by 4 km equally spaced subfaults. The hypocenter depth of the model is determined by projecting the epicenter location of the Chi Chi earthquake determined by the Taiwan Central Weather Bureau down to the curved fault plane. For a constant rupture velocity, Figure 12 shows the rupture time distribution along the flattened fault plane with a 2-sec time interval between adjacent contour lines.

For each subfault, we assume a variable rake for the slip and a rupture time delay Δt relative to the time derived from the shortest distance to the hypocenter along the fault plane divided by a constant rupture velocity of 2.5 km/sec. The rake was constrained within a range of 70 ± 45 degree, where the average rake determined from the USGS fault plane solution is 70 degree. The rupture time delay Δt varies from 0 to 4 second. By trials and errors, we found that a subevent rupture velocity ranging between 0.5 to 2.0 km/sec has produce good overall fit to the velocity amplitudes between the observation and the synthetics over the frequency band used for the data analysis.

The static deformation data for this inversion study were obtained from the GPS observation made by the Institute of Earth Science, Taiwan Academic Sinica. The cross symbols in Figure 11 show the distribution of GPS stations. A total of 130 stations of three component static deformation measurements were used for the inversion. We also selected 15 strong motion stations (green solid circle in Figure 11) for waveform inversion analysis. The station names and coordinates are also listed in Table 2. Most of the stations are distributed on the hanging-wall of the Chelungpu fault. We used all three component observations for the static deformation analysis but only the horizontal component data for the waveform study. The acceleration waveforms were integrated to velocity seismograms. All the waveforms were bandpass-filtered between 0.05 to 0.25 Hz. Because of lack of correct timing for many stations, we picked S-wave arrival times for all the selected strong motion stations and aligned them with the synthetic predicted S-wave arrival times calculated from the stations to the hypocenter. We did not further adjust those arrival times during the inversion.

Table 2

Station names and locations for the Chi-Chi earthquake

Name	Latitude	Longitude
T078	23.8123	120.8455
T046	24.4687	120.8540
T071	23.9860	120.7882
C025	23.7800	120.5142
T079	23.8397	120.8942
T074	23.9607	120.9617
T072	24.0392	120.8577
T064	24.3460	120.6095
T051	23.1887	121.0168
H056	24.1795	121.5077
C102	23.2455	120.6138
T089	23.9037	120.8565
H035	23.7302	121.4445
H024	23.3522	121.2970
I067	24.4400	121.3728

The velocity model for Taiwan is taken from Chen et al. (1998). Their model was based on modeling the generation and propagation of short-period surface waves in the island, a large quantity of high quality S-wave arrival times, and local geological structure. We took their vertical velocity structure under each station as the layered crustal structure to compute Green's functions between all the subfaults and the station. A map view of the velocity model with examples of vertical velocity profile was shown in Figure 13.

Result and Discussion

Based on the earth structure and source model discussed in the previous section, we compute the inverse solution of the Chi-Chi earthquake composite source rupture using a combined GPS and strong motion data set. Figure 14 compares the synthetic static ground deformations computed using the source model derived from the inversion with the observations. For the horizontal component, the synthetic deformations agree very well with the observation, especially for stations located in the southern part of the fault. Discrepancy between synthetics and observations increases for stations around the northern end of the fault. Earthquake faulting near the northern end may not consist of a single rupture plane and our subfault division is still too coarse to accurately describe the rotation in rake angle near the area. Although the vertical component static deformation is not plotted here, there are few stations to the southeast of the fault with vertically downward ground deformation in comparison to the upward ground deformation for stations to the west. Synthetic test shows that it occurs only when earthquake rupture stops at least east of those stations.

Figure 15 compares the synthetic and observed ground velocity waveforms. The traces at each panel correspond to different components of velocity seismograms. The observed seismograms are plotted above the synthetics for each station. The peak velocities (in cm/sec) are shown to the right of the seismograms followed by their station names and the orientation (in degrees) of components measured from north. For most stations, the synthetic waveforms match very well with the observations. Both horizontal components of C025 and the north component of T064 were underpredicted by the synthetics, especially at large lapse time, as we have expected for the two basin staitons. The waveform fitting to station T046 critically depends on the east-west striking fault segment to the end of the northern fault bend. Iwata et al. (2001)

found that the waveform match at station T046 could be improved by introducing a fault segment with a shallower dipping angle based on the aftershock distribution. Their shallow dipping fault could have produced the same radiation effect compared to our extended fault segment at the northern end of the fault. The improvement to the final fitness function for the waveform inversion is above 50% over the average value of the fitness functions calculated from the starting models.

Figure 16 shows the final slip amplitude and slip vector distribution of the Chi-Chi earthquake composite soruce model. Overall the slip amplitude distribution appears in a reversed triangular shape with an average slip of 4.6 m over the triangularly shaped fault zone. The total moment of the earthquake was estimated at 2.9×10^{27} dyn-cm. This value agrees very well with the USGS and Harvard moment tensor solution of 2.7×10^{27} dyn-cm. On average, the slip vector rotates from predominantly vertical dip-slip in the south to oblique thrust in the north, except the east-west striking segment near the northern end of the fault. This is expected from the dynamics of a thrust fault close to the free surface with non-vertical dip-slip (Oglesby and Day, 2000). There is relatively little slip near the hypocenter, as has been found for many other large earthquakes (i.e., Kocaeli, Northridge, Landers, Loma Prieta, etc). There was, however, more high frequency radiation observed in or south of the epicenter area than around the northern section of the fault (Figure 10). This suggests that rupture started small but with a very strong and short scale inhomogeneous slip process near the hypocenter. As it propagated to the north, rupture gradually became smoother. The slip distribution of the composite source model is comparable to the other source model inversion solution of Zeng and Chen (2001). In that study, they found an inverse correlation between the aftershock distribution and the mainshock slip, suggesting that the mainshock released stresses in the rupture area and transferred the stress concentration to its surrounding neighbors where aftershock has taken place.

High Frequency Analysis

Following the same procedure as with the Kocaeli earthquake ground motion modeling, we have modeled the site effect by propagating the synthetic ground motion calculated using the crustal velocity model discussed earlier through a 30 meters thick layer of low velocity soil at each station using the DESRA2 program (Lee and Finn, 1982). The average shear wave velocity for the top 30 meters soil structure is determined according to the USGS published site classification using shear wave velocities and the parameters for any nonlinear site response are specified according to EPRI (1993). The site classifications for all strong motion stations are provided by Silva (2002, personal communication) and are listed in Table 3.

Table 3

Station names and locations for the Chi-Chi earthquake

Name	Latitude	Longitude	Site Class
T046	24.4683	120.8543	B
T039	24.4917	120.7837	C
T128	24.4162	120.7607	C
T036	24.4488	120.6963	D
T087	24.3482	120.7733	C
T103	24.3098	120.7072	D
T068	24.2720	120.7658	D
T102	24.2493	120.7208	D

T136	24.2603	120.6518	C
T060	24.2247	120.6440	D
T052	24.1980	120.7430	D
T049	24.1790	120.6902	D
T082	24.1475	120.6760	D
T057	24.1732	120.6107	C
T067	24.0912	120.7200	D
T063	24.1083	120.6158	D
T065	24.0588	120.6912	D
T109	24.0848	120.5713	D
T075	23.9827	120.6778	D
T071	23.9855	120.7883	D
T072	24.0407	120.8488	D
T074	23.9622	120.9618	D
T120	23.9803	120.6130	C
T123	24.0187	120.5437	D
T138	23.9223	120.5955	D
T076	23.9077	120.6757	D
T089	23.9037	120.8565	C
T084	23.8830	120.8998	B
T079	23.8395	120.8942	D
T078	23.8120	120.8455	D
T116	23.8568	120.5803	E
T122	23.8128	120.6097	D
C024	23.7570	120.6062	D
C025	23.7795	120.5137	E
C101	23.6862	120.5622	D
C028	23.6320	120.6052	D
C006	23.5815	120.5520	D
C041	23.4388	120.5957	D
C034	23.5212	120.5443	D
C029	23.6135	120.5282	C
C010	23.4653	120.5440	D

In order to test the ability of the composite source model to predict the near-field ground motion, we selected 41 stations. Most of those stations were not included in the previous inversion analysis. Figure 17 plots the distribution of those stations. Based on the inversion solution, we computed the broadband synthetic ground motion for the frequency range of 0 to 25 Hz at all 41 near-field stations. For a subevent rupture velocity that varies from 0.5 to 2.0 km/sec, the result shows an overall underestimation of the high frequency radiation. This is similar to what we have found for the Kocaeli earthquake ground motion simulation. Following what we have done for the Kocaeli earthquake, we assumed a variable rupture velocity model for the subevents of the Chi-Chi earthquake composite source model. By trial and errors, we found that an increase of subevent rupture velocity from v_1 to v_2, where v_1 varies from 0.5 to 2.0 km/sec and v_2=2.5 km/sec, produces unbiased high frequency ground motion in comparison with the Chi-Chi earthquake observations. Figure 18 plots the misfit between the observation and synthetic prediction for the horizontal components and the vertical component. The misfit is quantified based on biases and standard errors. The middle line (red) in each top panel shows the biases versus periods with the 90% confidence limits envelopes of the biases. The standard errors are plotted in the lower panel. The average errors are 0.60 and 0.65 for the horizontal and vertical components, respectively.

Figure 19 compares the observed and synthetic ground acceleration, velocity, and displacement time histories at station T052. Observation at this site has shown large static deformation and velocity pulses. The large static deformation with slow rise time is sometimes call fault fling step. Though the effect of fault fling on building structure has not been well quantified, it is believed that damages caused by the fault fling step may be significantly lower than expected by simple extrapolation using the peak ground velocity values. For the displacement and velocity time series, synthetics agree quite well with the observations at the site. The synthetic accelerations appear more complicated than the observation. But their peak values are still in very good agreement. Figure 20 plots the comparison of acceleration time histories and their Fourier amplitudes between the synthetics and the observations for all 41 stations. For each component, the synthetic seismograms are plotted below the observation. The observed spectra are plotted in solid line and the synthetics are in dotted lines. For stations to the north of the epicenter, the simulation in general agree well with the observation in their peak values and duration. For stations to the south of the epicenter, there is a systematic underprediction of the recorded ground motions. This feature may be better explained by a dynamic fault rupture model, for example, differences in friction parameters for the southern and northern segment of the fault. Figure 21 plotted the biases and 90% confidence limits for the 27 northern stations. As expected there are slight overprediction of the high frequency ground motion for those stations.

Conclusion

We have computed a joint GPS static deformation and strong motion waveform inversion for the Kocaeli earthquake and the Chi-Chi earthquake to obtain the composite source rupture processes of the events. The genetic algorithm procedure developed by Zeng and Anderson (1996) was used to calculate the inverse solution. For both earthquakes, we used a fault model with a curved fault plane based on the field surface rupture data. We found evidence of supershear rupture velocity for the Kocaeli earthquake fault rupture. For both events, the subevent of the composite sources shows significant slow rupture or long rise time comparing with other earthquakes we have previous studied. The total moment is 2.1×10^{27} dyne-cm for the Kocaeli earthquake and 2.9×10^{27} dyne-cm for the Chi-Chi earthquake.

We found that a variable rupture velocity for the subevent rupture of the composite sources provided an overall unbiased fit to the observed ground motion response spectra in the frequency range of 0.1 to 25 Hz. For the Kocaeli earthquake, the subevent rupture velocity increases from v_1 to v_2, where v_1 varies from 0.5 to 2.0 km/sec and v_2=2.0 km/sec. For the Chi-Chi earthquake, the subevent rupture velocity increases from v_1 to v_2, where v_1 varies from 0.5 to 2.0 km/sec and v_2=2.5 km/sec. In general, we found that the composite source model has generated very realistic ground motion in comparison with the observations. For the Chi-Chi earthquake, there is systematic underprediction for stations to the south of the epicenter and slight overprediction for stations to the north of the epicenter. Overall, the composite source simulations agree very well with the observations over a broad frequency band for the ground motion amplitudes and duration.

Reference

Anderson , J. G. and G. Yu (1996). Predictability of strong motions from the Northridge, California, earthquake, Bull. Seism. Soc. Am. No. 86, 1B, S100-S114.

Anderson, J. G., Y. Zeng and H. Sucuoglu (2001). Analysis of accelerations from the Dinar, Turkey earthquake, *Bull. Seis. Soc. Am.*, **91**, 1433-1445.

Celebi, M., S. Akkar, U. Gulerce, A. Sanli, H. Bundock, and A. Salkin (2001). Main Shock and Aftershock Records of the 1999 Izmit and Duzce, Turkey Earthquakes, USGS Open-File Report 01-163.

Chen, C.-H., T.-L. Teng and Y.-C. Gung (1998). Ten-second Love wave propagation and stong ground motions in Taiwan, J. Geophy. Res., 103, 21253-21273.

EPRI, Guidelines for determining design basic ground motions. Volume 1: Method and guidelines for estimating earthquake ground motion in Eastern North America, report, EPRI TR-102293, Nov. (1993).

Eshelby, J. D. (1957). The determination of the elastic field of an ellipsoidal inclusion, and related problems, Proceedings of the Royal Society of London A241:376-396.

Iwata, T., H. Sekiguchi, and K. Irikura (2001). Rupture process of the 1999 Chi Chi, Taiwan, earthquake and its near-source strong ground motions, submitted to *Bull. Seism. Soc. Am.*

Johnson, M. (1999). Composite source model parameters for large earthquakes (M>5.0) in the Mexican subduction zone, M. S. thesis, University of Nevada, Reno.

Khattri, K. N., Y. Guang, J. G. Anderson, J. N. Brune and Y. Zeng (1994). Seismic hazard estimation using modelling of earthquake strong ground motions: A brief analysis of 1991 Uttarkashi earthquake, Himalaya and prognostication for a great earthquake in the region, *Current Science*, 67, 343-353

Kudo, K., T. Kanno, H. Okada, O. Ozel, M. Erdik, T. Sasatani, S. Higashi, M. Takahashi, and K. Yoshida (2002). Site-Specific Issues for Strong Ground Motions during the Kocaeli, Turkey, Earthquake of 17 August 1999, as Inferred from Array Observations of Microtremors and Aftershocks, Bulletin of the Seismological Society of America, 92, 448–465.

Lee, M. K. W. and W. D. L. Finn (1982). Dynamic effective stress response analysis of soil deposites with energy transmitting boundary including assessment of liquefaction potential, Rev., Dept. of Civil Eng., Soil Mechanics Serirs No. 38, the Univ. of British Columbia, Vancouver, Canada.

Ni., S.-D., J. G. Anderson, Y. Zeng (1999). Comparison of strong ground motions from the 1988 Seguenay earthquake with the synthetic simulations using the composite source model, in preparation.

Oglesby, D. D., and S.M. Day, (2000) Fault geometry and the 1999 Chi-Chi (Taiwan) Earthquake, *Seism. Res. Lett.*, **71**, 226.

Reilinger, R.E., S. Ergintav, R. Bürgmann, S. McClusky, O. Lenk, A. Barka, O. Gurkan, L. Hearn, K. L. Feigl, R. Cakmak, B. Aktug, H. Ozener, M.N. Töksoz (2000). Coseismic and postseismic fault slip for the 17 August 1999, M=7.5, Izmit, Turkey Earthquake, *Science* , *289*, 1519-1524.

Sato, T. and T. Hirasawa (1973). Body wave spectra from propagating shear cracks, *J. of Phys. of the Earth*, **21**, 415-431.

Sekiguchi, H. and T. Iwata (2002). Rupture Process of the 1999 Kocaeli, Turkey, Earthquake Estimated from Strong-Motion Waveforms, Bulletin of the Seismological Society of America, 92, 300–311.

Somerville, P. G., N. F. Smith, R. W. Graves, and N. A. Abrahamson (1997). Modefication of empirical strong ground motion attenuation relations to include the amplitude and duration effects of rupture Directivity, Seism. Res. Lett., 68, 199-222.

Su, Feng, Y. Zeng and J. G. Anderson (1994a). Simulation of the Loma Prieta earthquake strong ground motion using a composite source model, EOS, Trans. A.G.U., **75**, 44, p448.

Su, F., Y. Zeng and J. G. Anderson (1994b). Simulation of Landers earthquake strong ground

motion using a composite source model, Seism. Res. Lett., **65**, p52.

Su, F., J. G. Anderson and Y. Zeng (1998). Study of weak and strong motion including nonlinearity in the Northridge, California, earthquake sequence, submitted to *Bull. Seis. Soc. Am.* **88**, 1411-1425.

Zeng, Y., J. G. Anderson and G. Yu (1994). A composite source model for computing realistic synthetic strong ground motions, *J. Res. Lett.*, **21**, 725-728.

Zeng, Y., J. G. Anderson and Feng Su (1995). Subevent rake and scattering effects in realistic strong ground motion simulation, *Geophy. Res. Lett*, **22**, 17-20.

Zeng, Y. (1995). A realistic synthetic Green's function calculation using a combined deterministic and stochastic modeling approach, *EOS, Trans. A.G.U.*, **76**, F357.

Zeng, Y. and J. G. Anderson (1996). A composite source modeling of the 1994 North-ridge earthquake using Genetic Algorithm,Bull. Seism. Soc. Am. 86, No. 1B, 71-83.

Zeng, Y. and J. G. Anderson (2000). Earthquake source and near-field directivity modeling of several large earthquakes, EERI Proceedings for the Sixth International Conference on Seismic Zonation.

Zeng, Y. (2001). Validation and modeling of earthquake strong ground motion using a composite source model, *EOS, Trans. A.G.U.*, **82**, F869.

Zeng, Y. and C. H. Chen (2001). A combined GPS measurements and strong motion waveform inversion of the source rupture process during the 1999 Chi Chi, Taiwan earthquake, *Bull. Seis. Soc. Am.* **91**, 1088-1098.

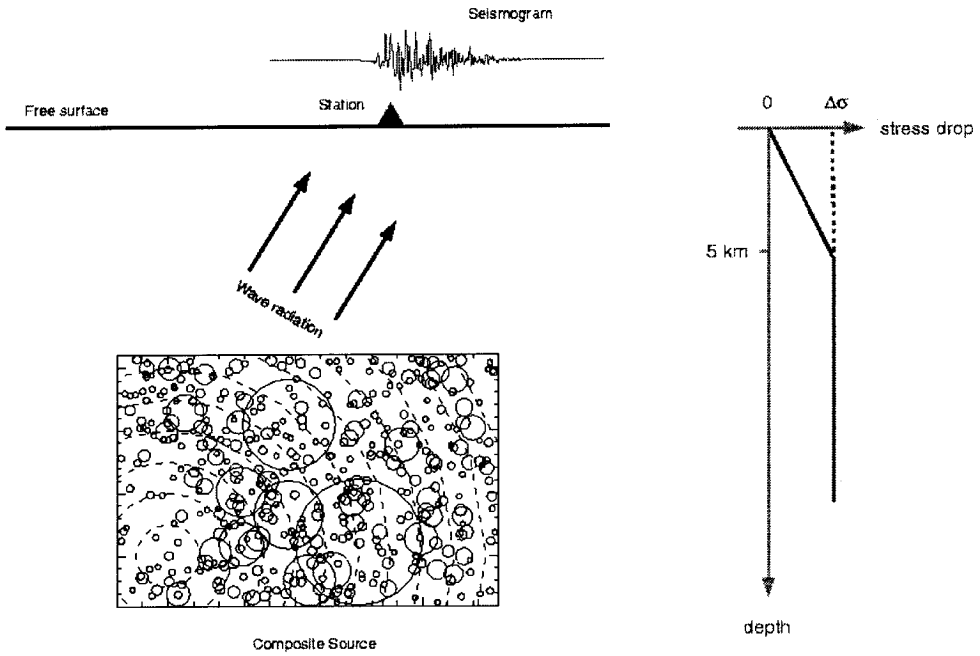

Figure 1(a). Schematic of source model in Composite Source Procedure.

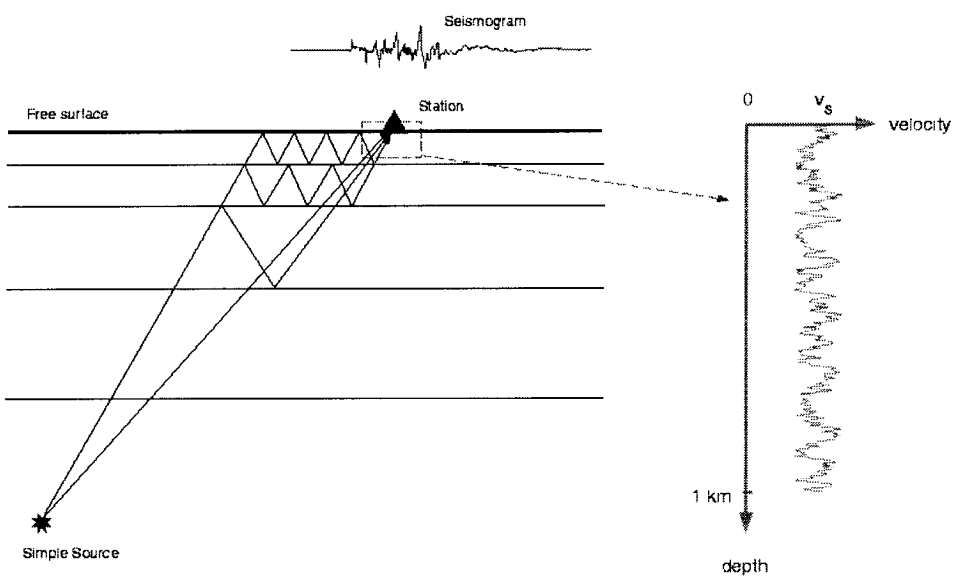

Figure 1(b). Schematic of flat-layered medium used for analysis of Green's functions in Composite Source Procedure.

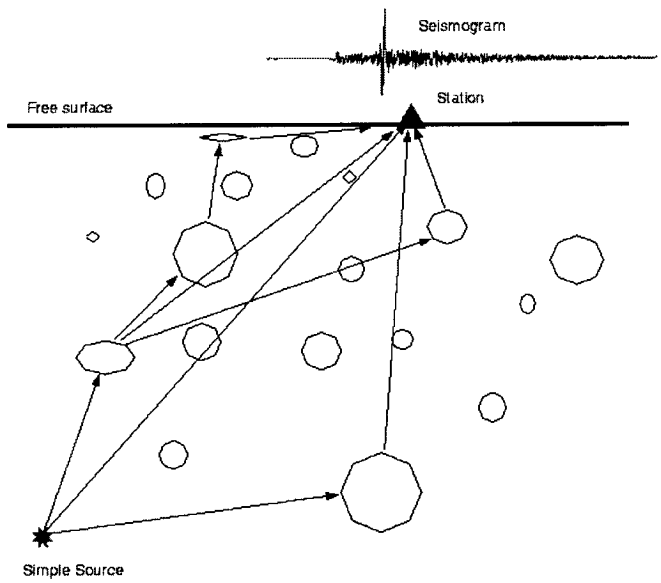

Figure 1(c). Schematic wave scatting model used to simulate effects of lateral crustal heterogeneity in Composite Source Procedure.

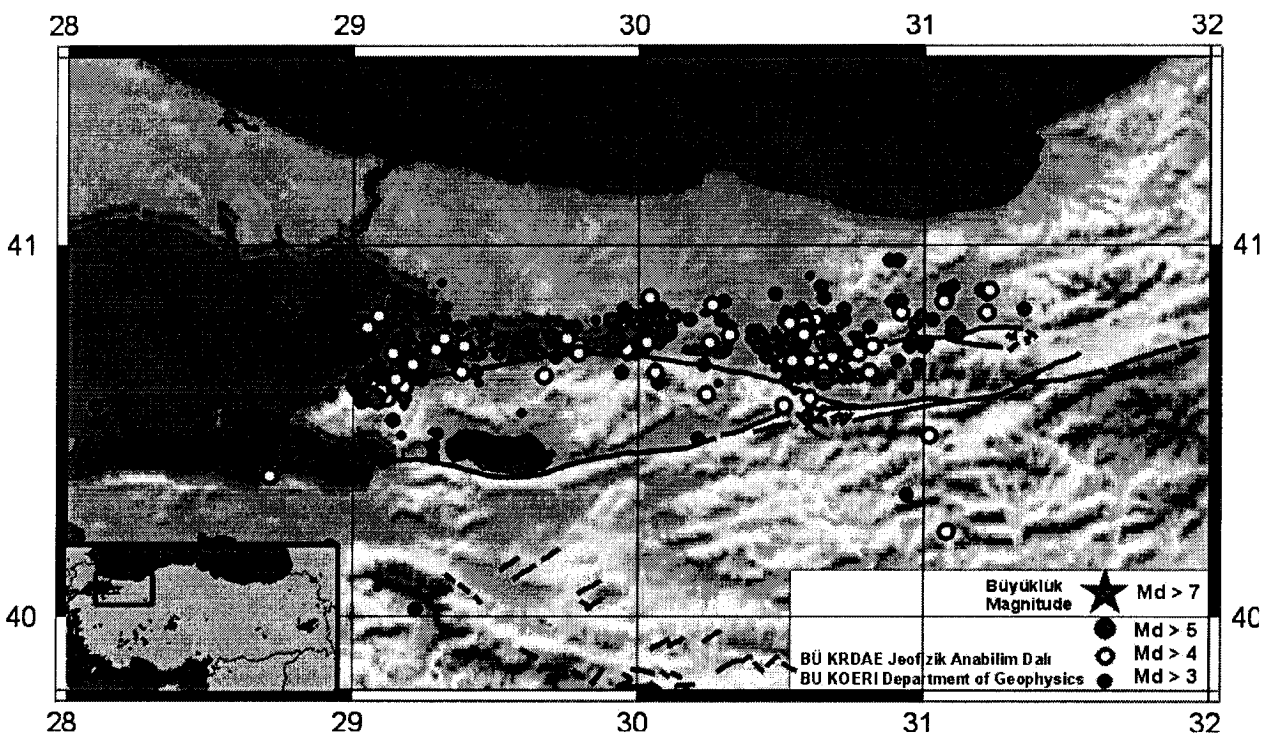

Figure 2. Map view of the ftershock distribution of the 1999 Kocaeli, turkey earthquake.

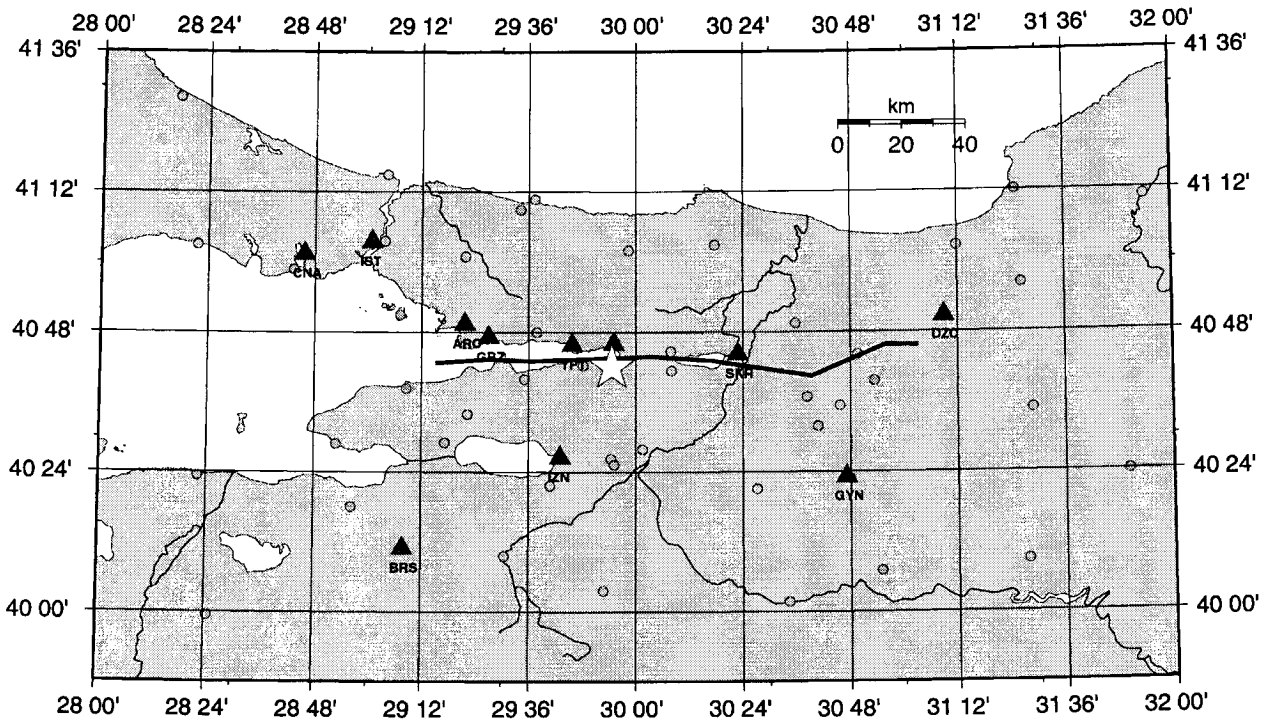

Figure 3 Map view of the surface trace of the Kocaeli earthquake fault used for this study. Star is the earthquake epicenter. The pink circles and blue triangles are GPS and strong motion stations, respectively.

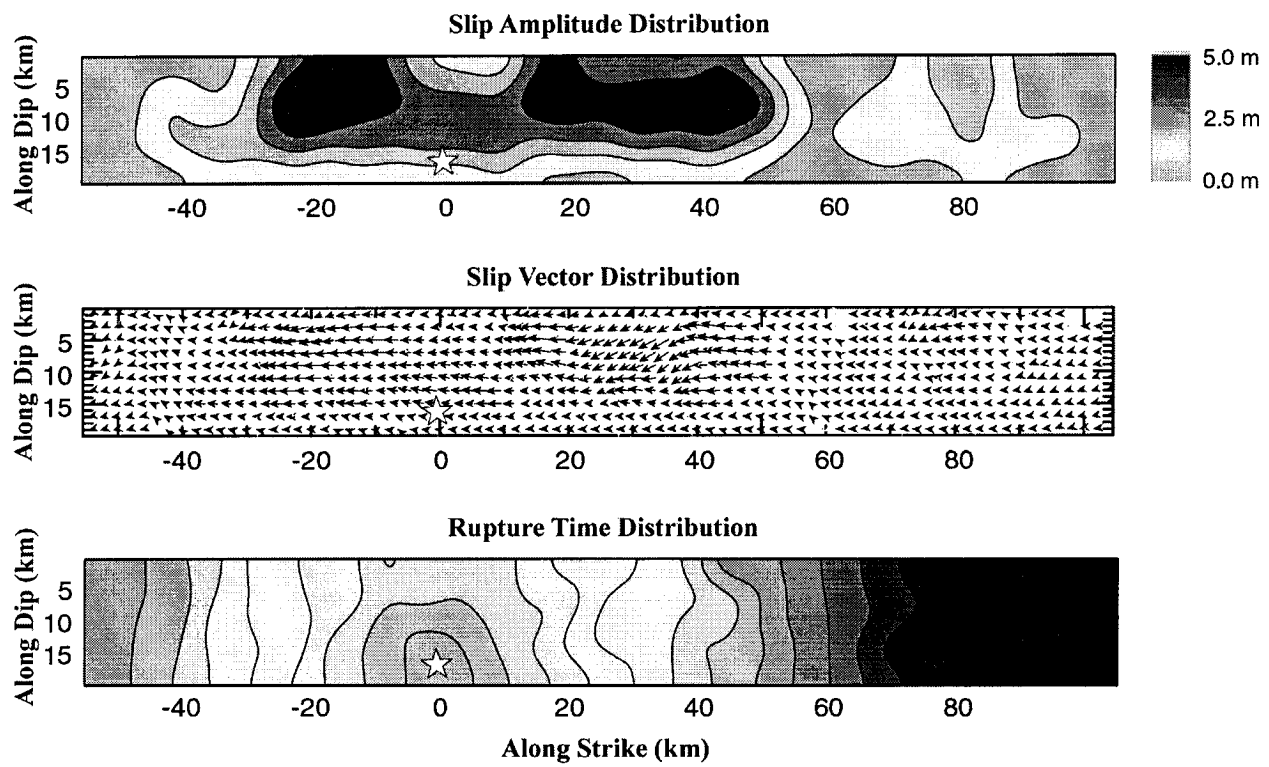

Figure 4. The Kocaeli earthquake composite source slip amplitude, slip vector, and rupture time distributions over the fault plane.

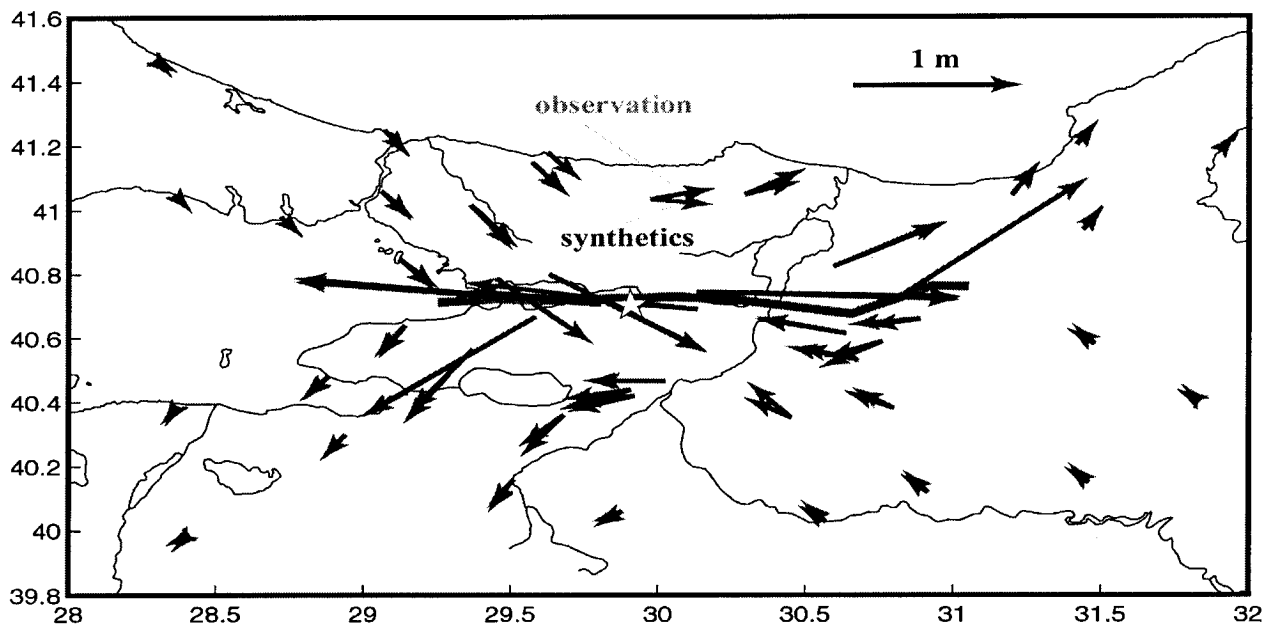

Figure 5. Comparison between the synthetic static ground deformations (red) computed using the source model determined from the inversion and the observed GPS measurements (blue).

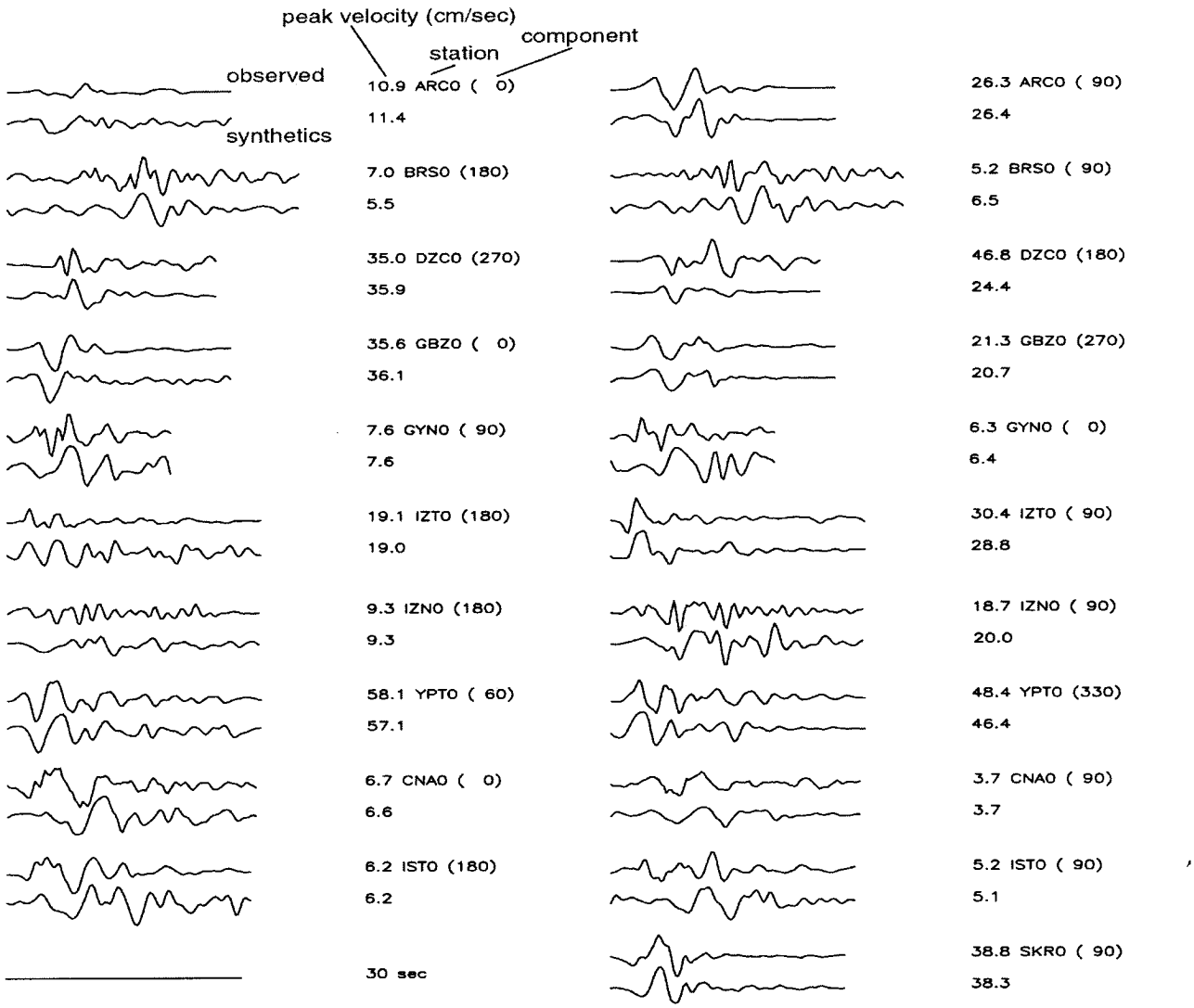

Figure 6. Comparison between synthetic and observed ground velocity waveforms. The traces within each panel correspond to different components of velocity seismograms. The observed seismograms are plotted above the synthetics for each station. The peak velocities (in cm/sec) are shown to the right of the seismograms followed by their station names and the orientation (in degrees) of components measured from north.

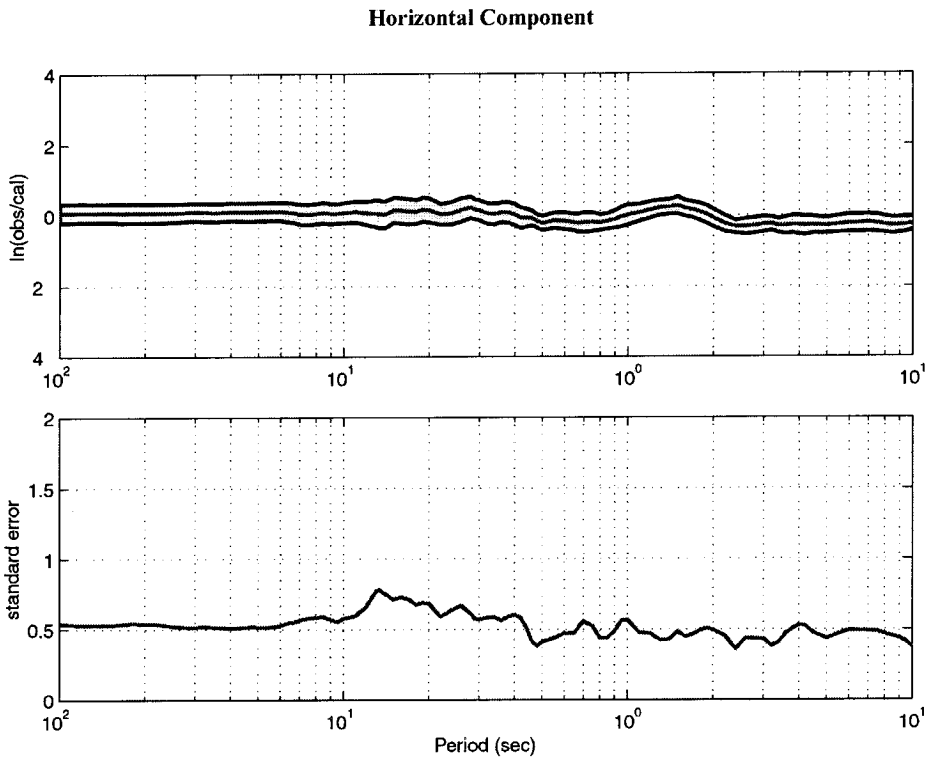

Figure 7a. The upper panel plots biases (red) and its 90% confidence limits (black) of the prediction for the horizontal component. The lower panel plots the standard errors.

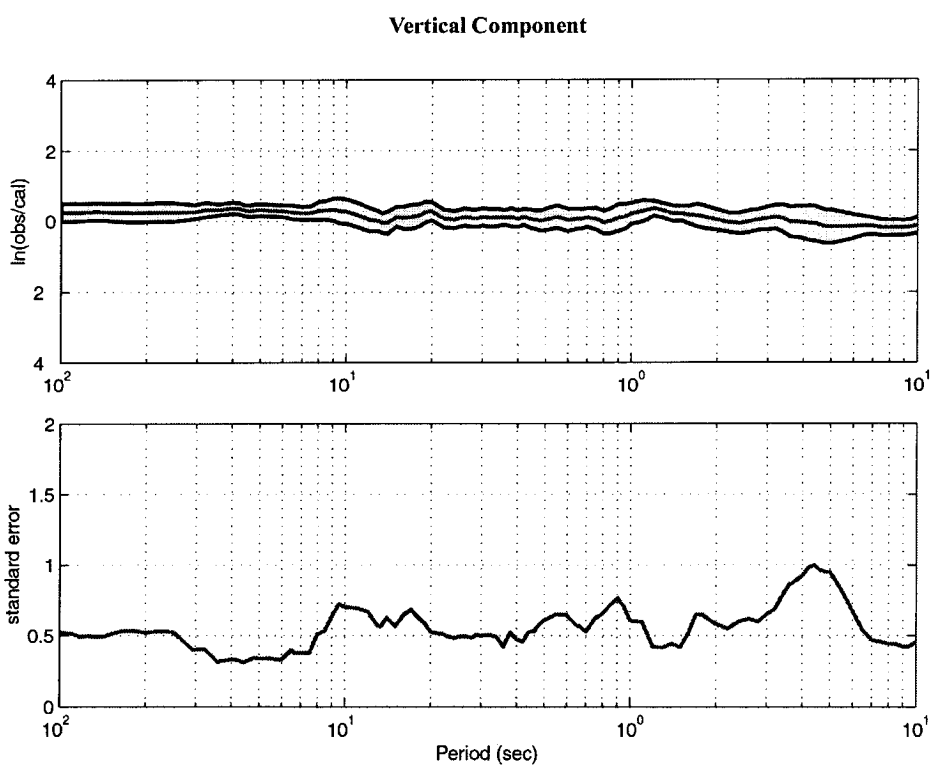

Figure 7b. Same as Figure7a but for the vertical component.

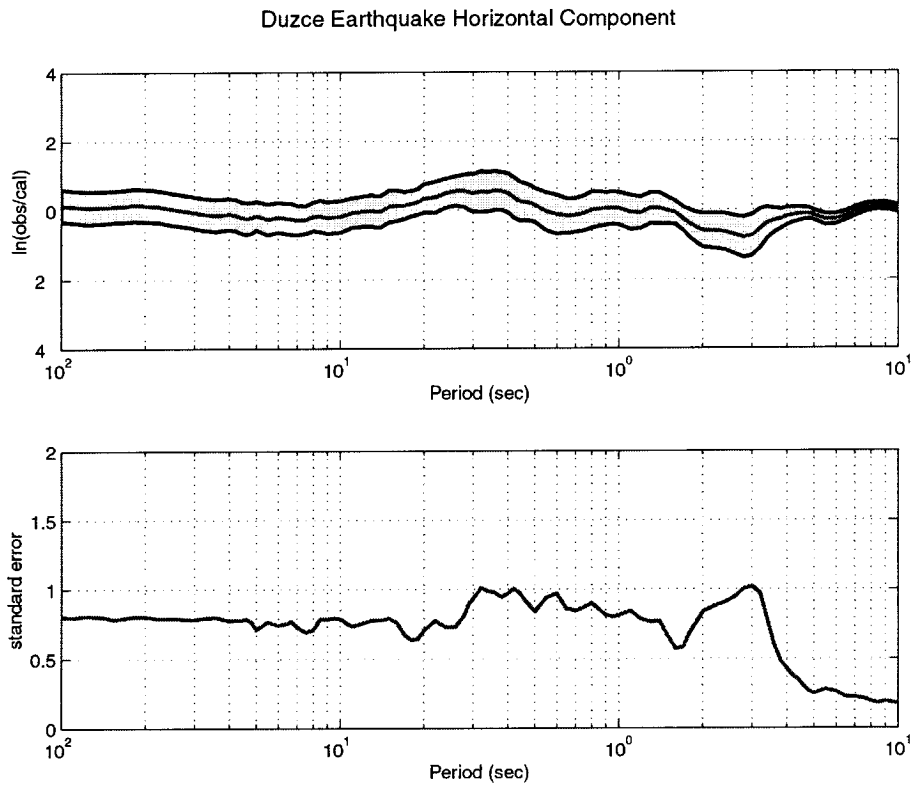

Figure 7c. The upper panel plots biases (red) and its 90% confidence limits (black) of the Duzce prediction for the horizontal component. The lower panel plots the standard errors.

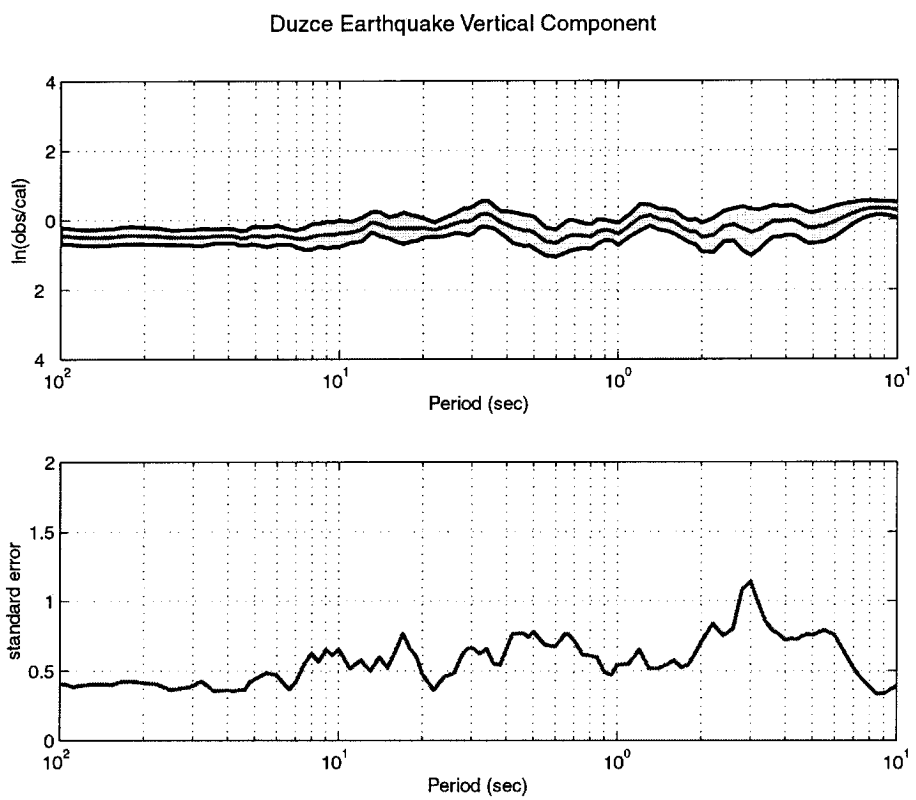

Figure 7d. Same as Figure7a but for the vertical component.

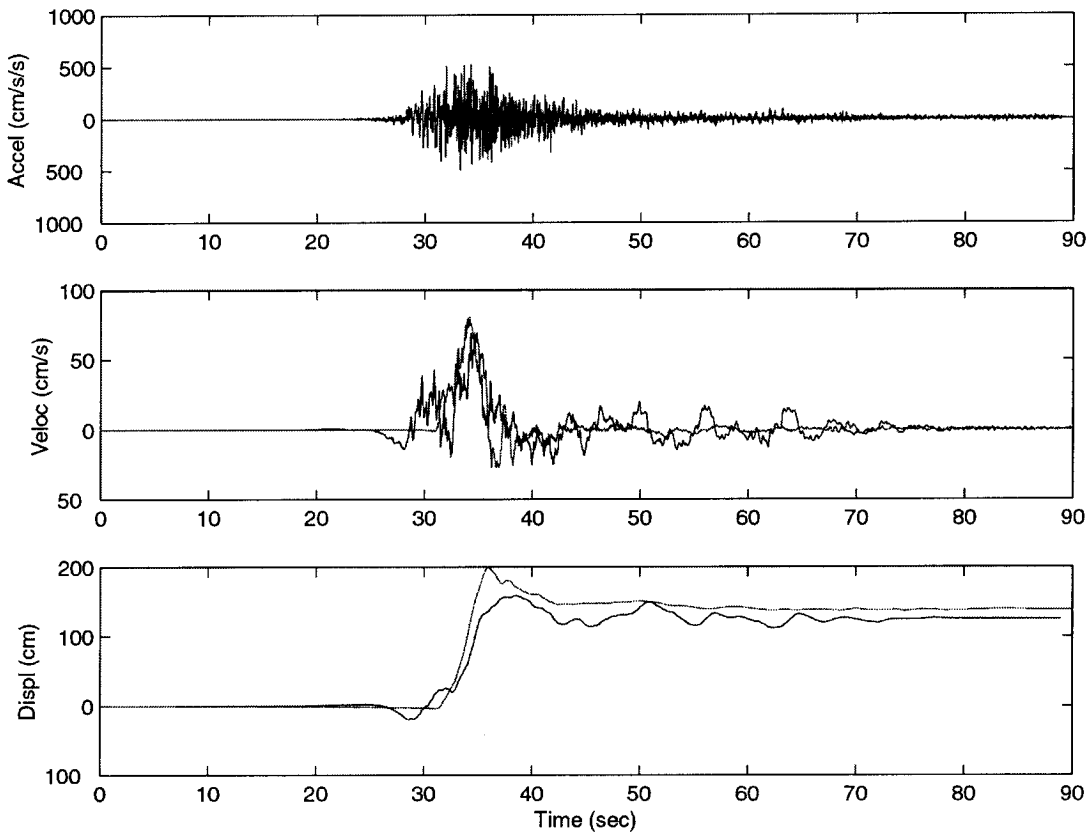

Figure 8. Comparison between the observed and synthetic ground acceleration, velocity and displacement at station SKR for the east horizontal component.

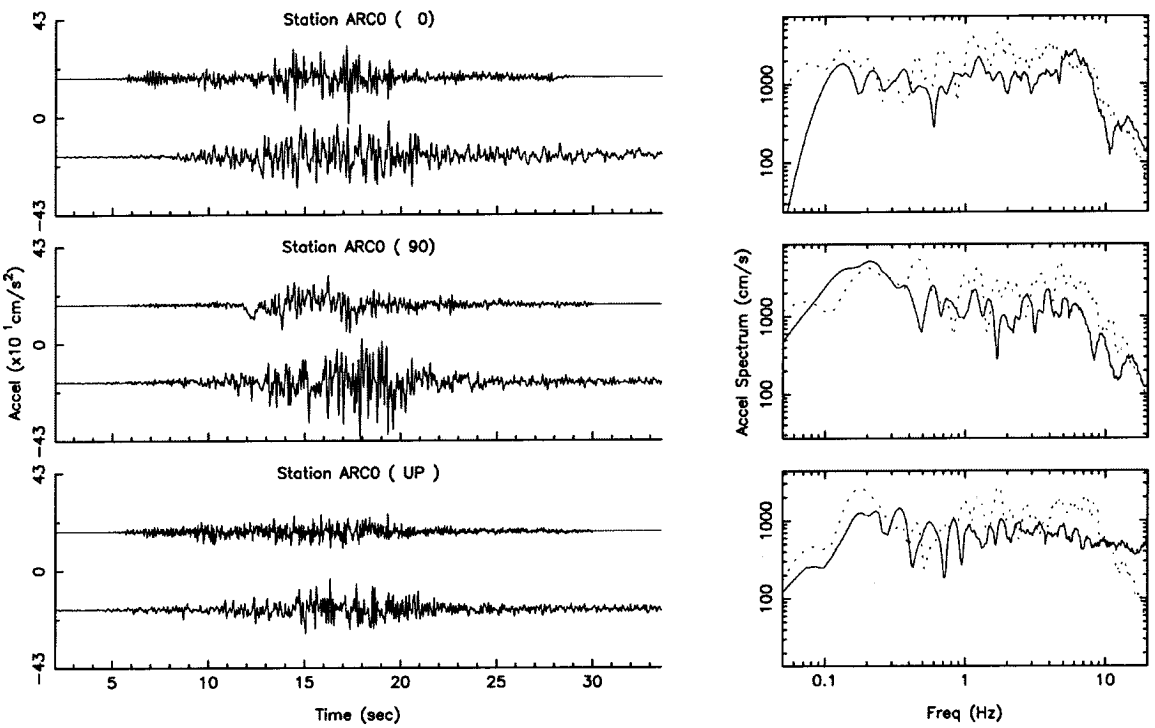

Figure 9. Comparison of acceleration time series and their Fourier amplitudes between the synthetics and the observation for all stations. For each component, the synthetic seismograms are plotted below the observation. The observed Fourier spectra are plotted in solid lines and the synthetics are plotted in dotted lines.

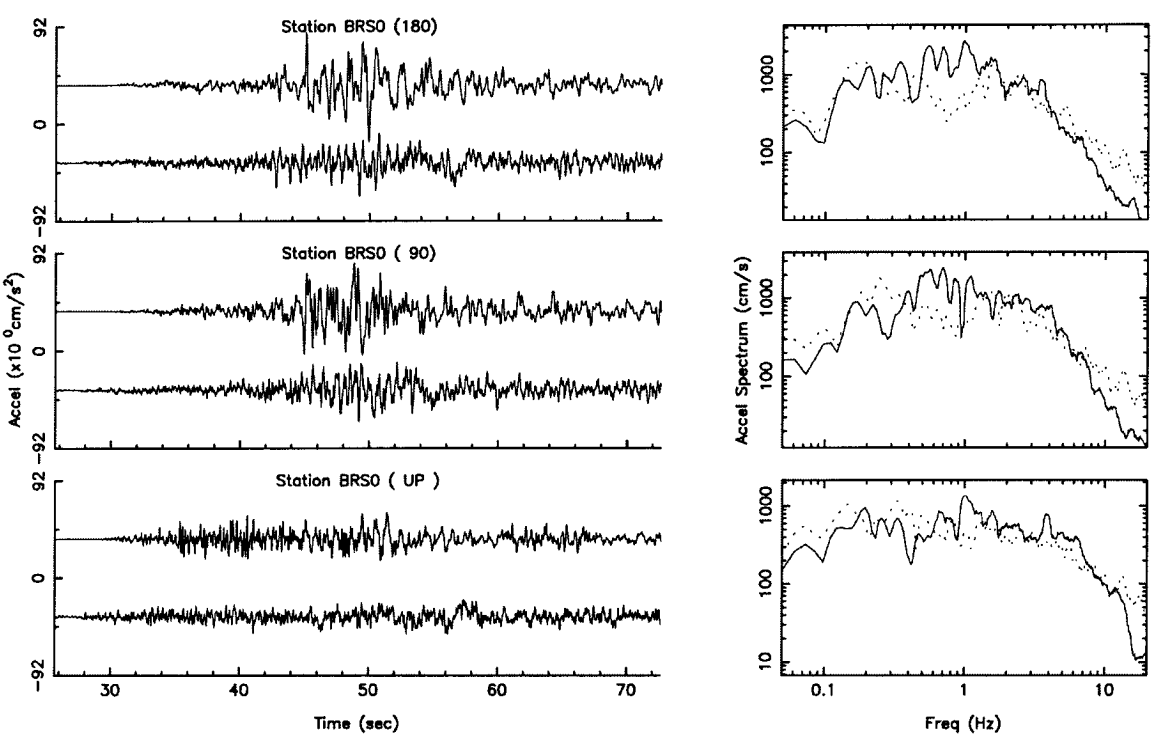

Figure 9. Continue.

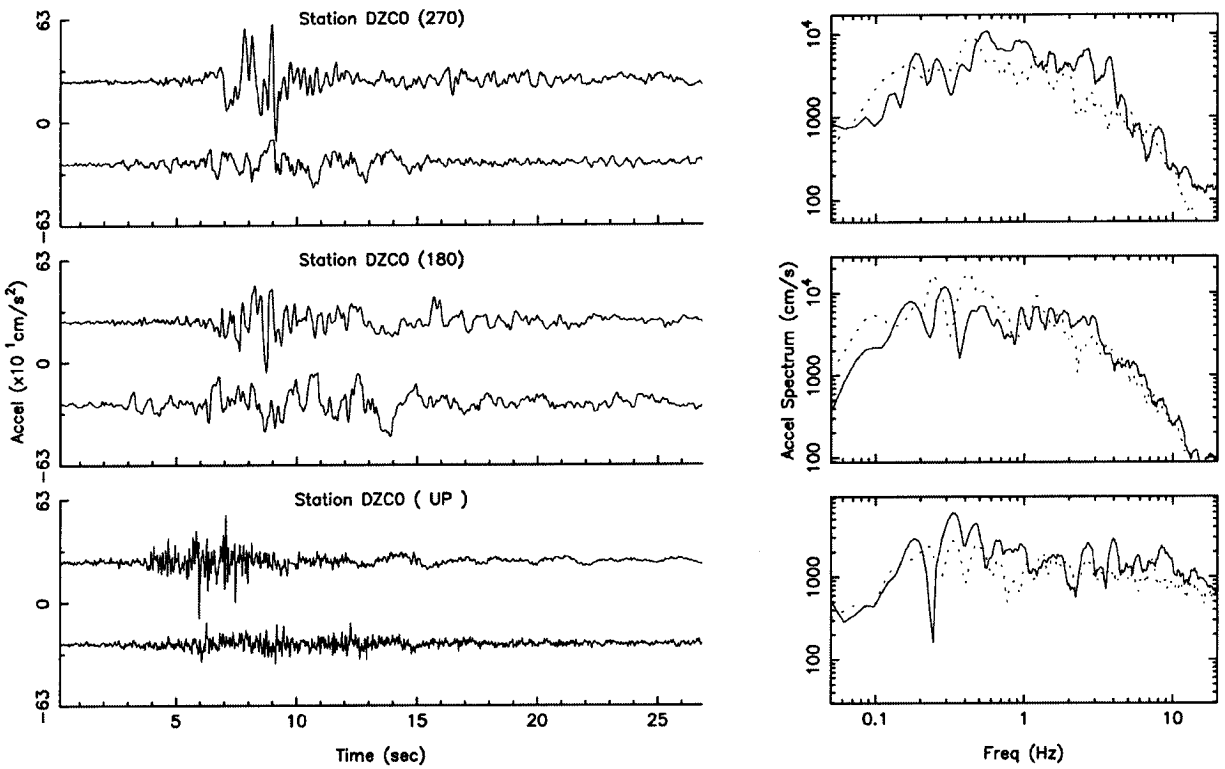

Figure 9. Continue.

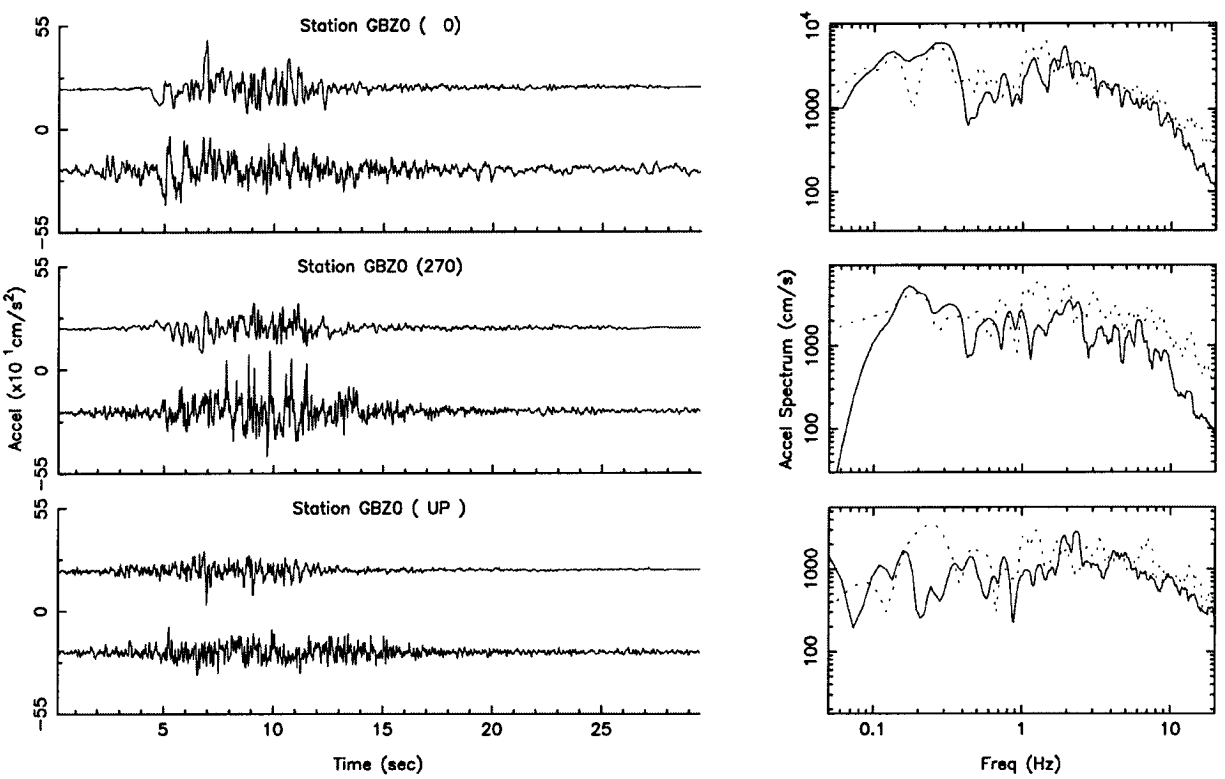

Figure 9. Continue.

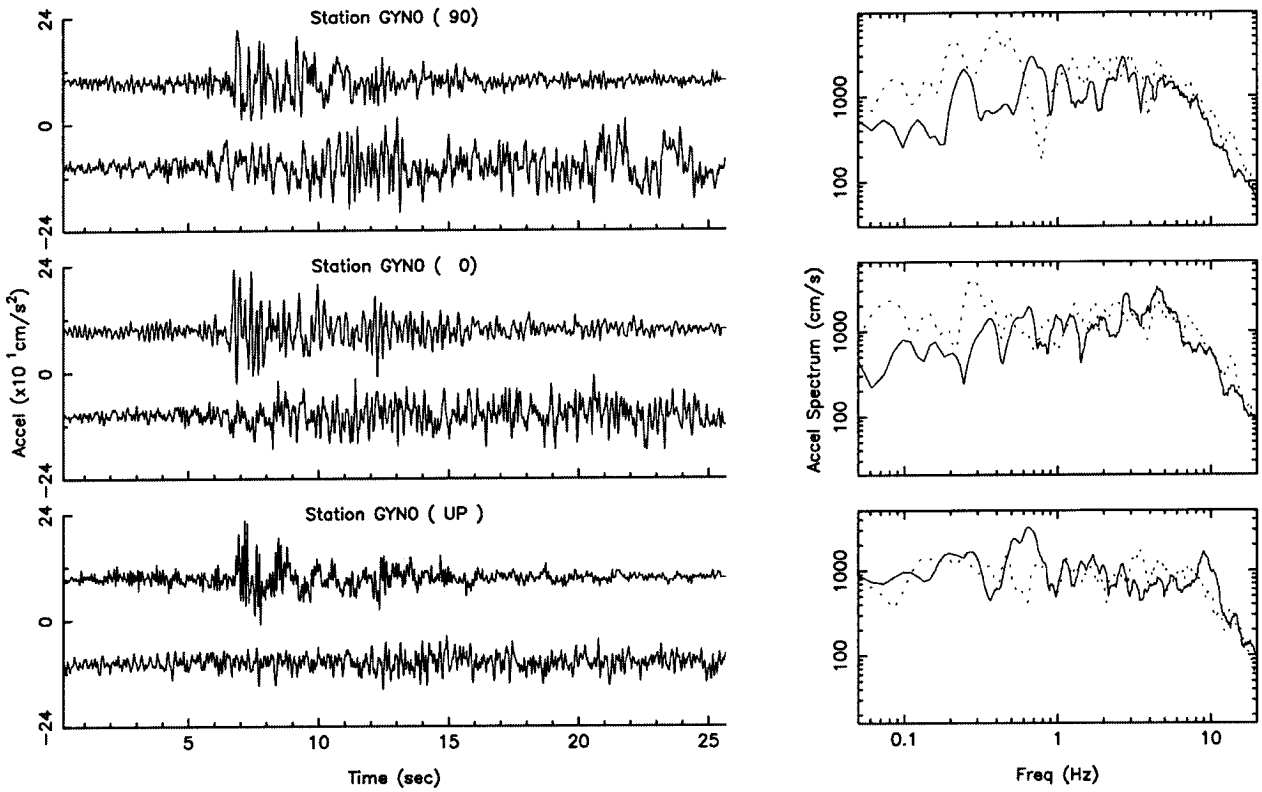

Figure 9. Continue.

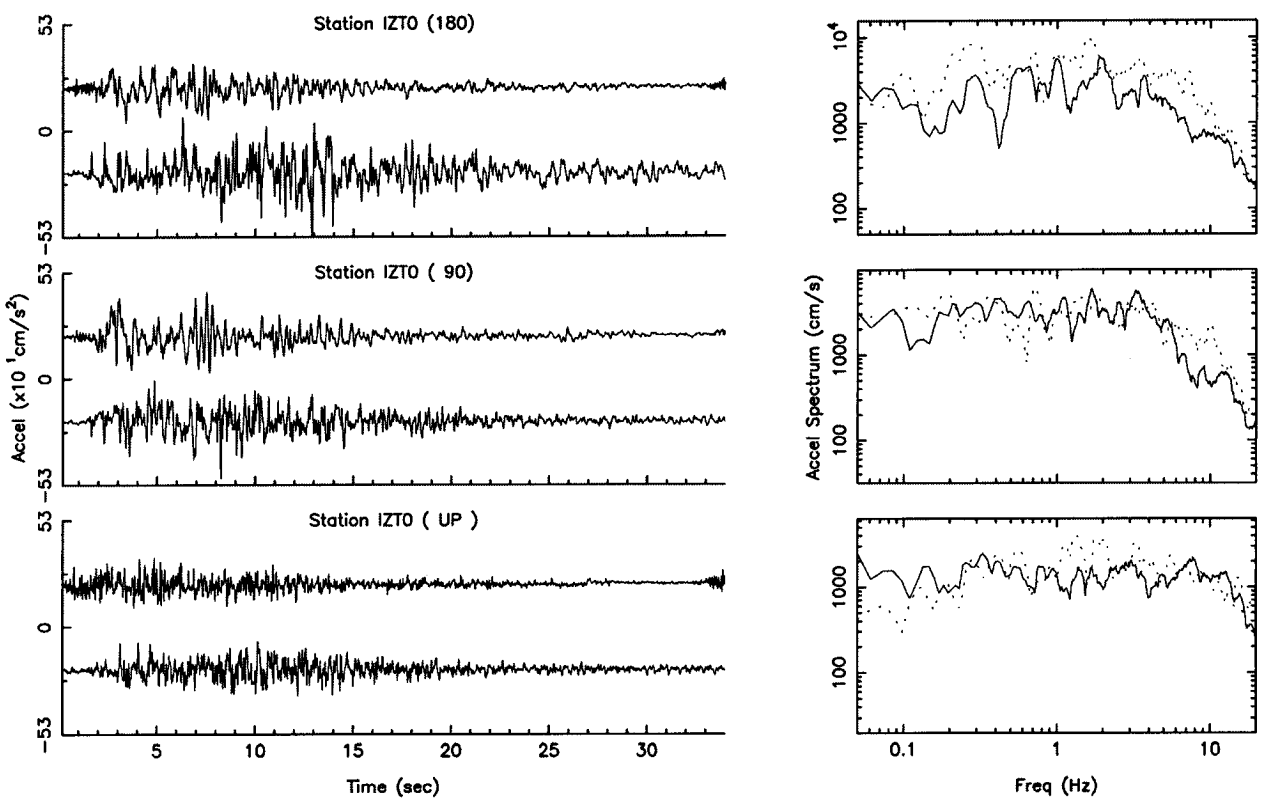

Figure 9. Continue.

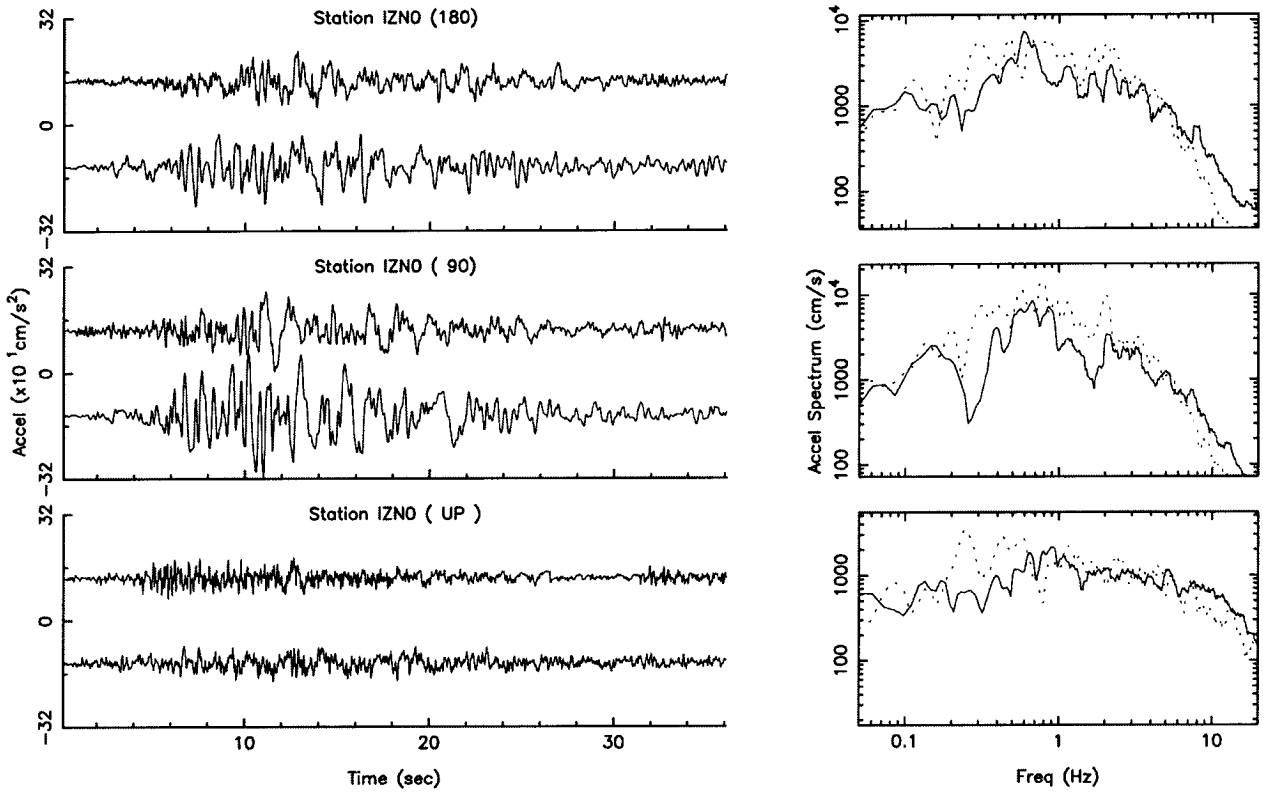

Figure 9. Continue.

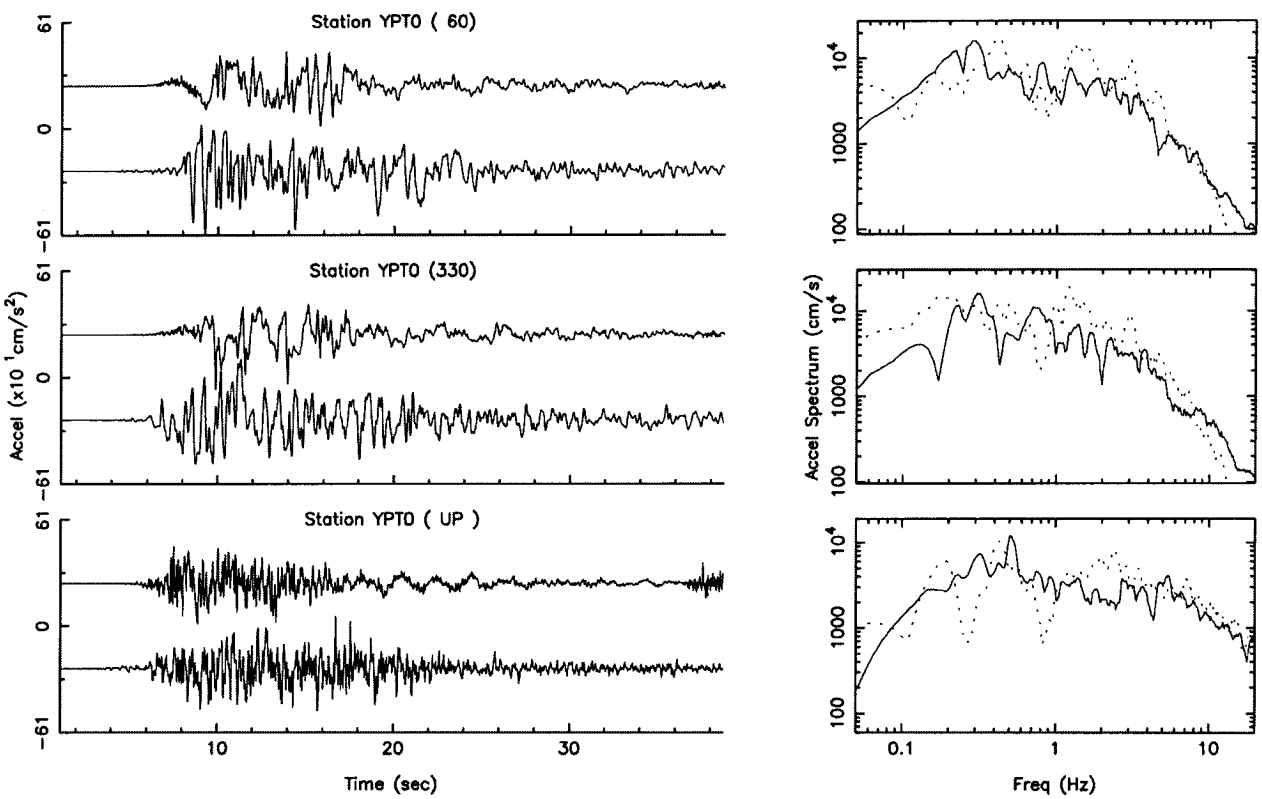

Figure 9. Continue.

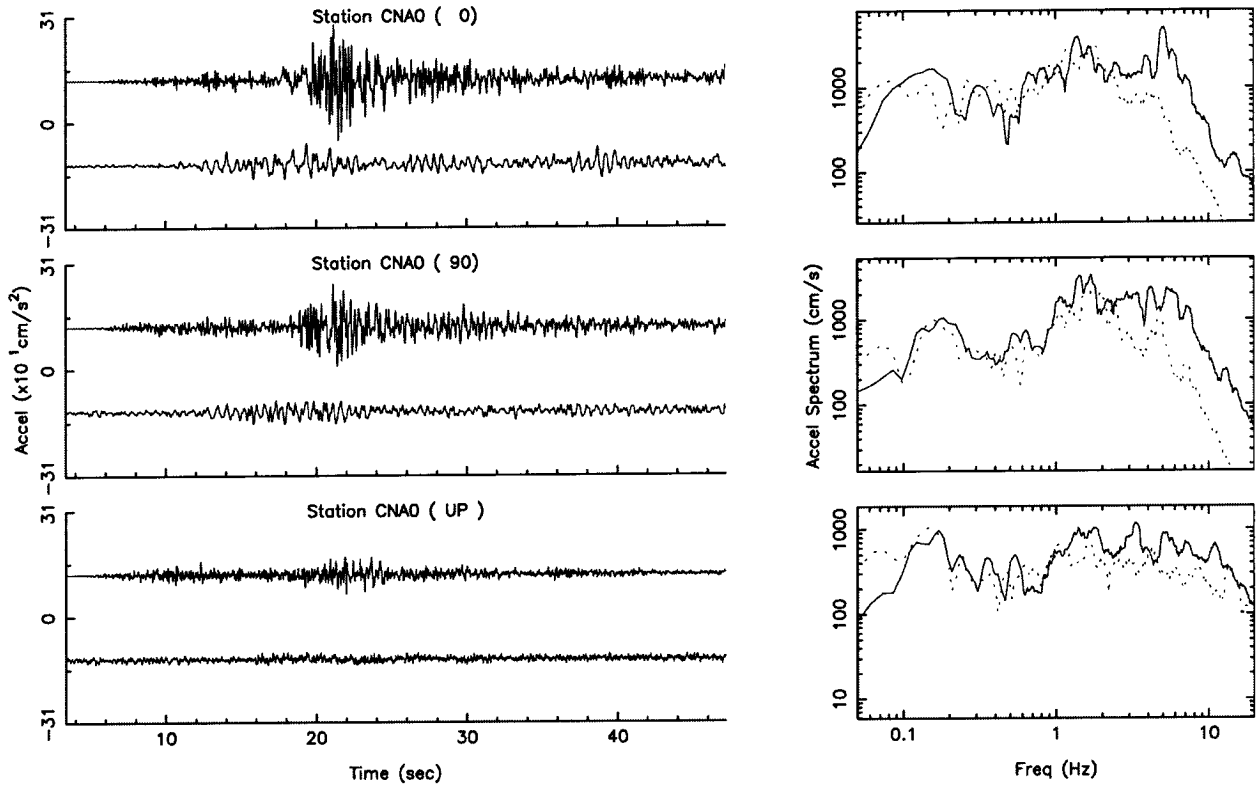

Figure 9. Continue.

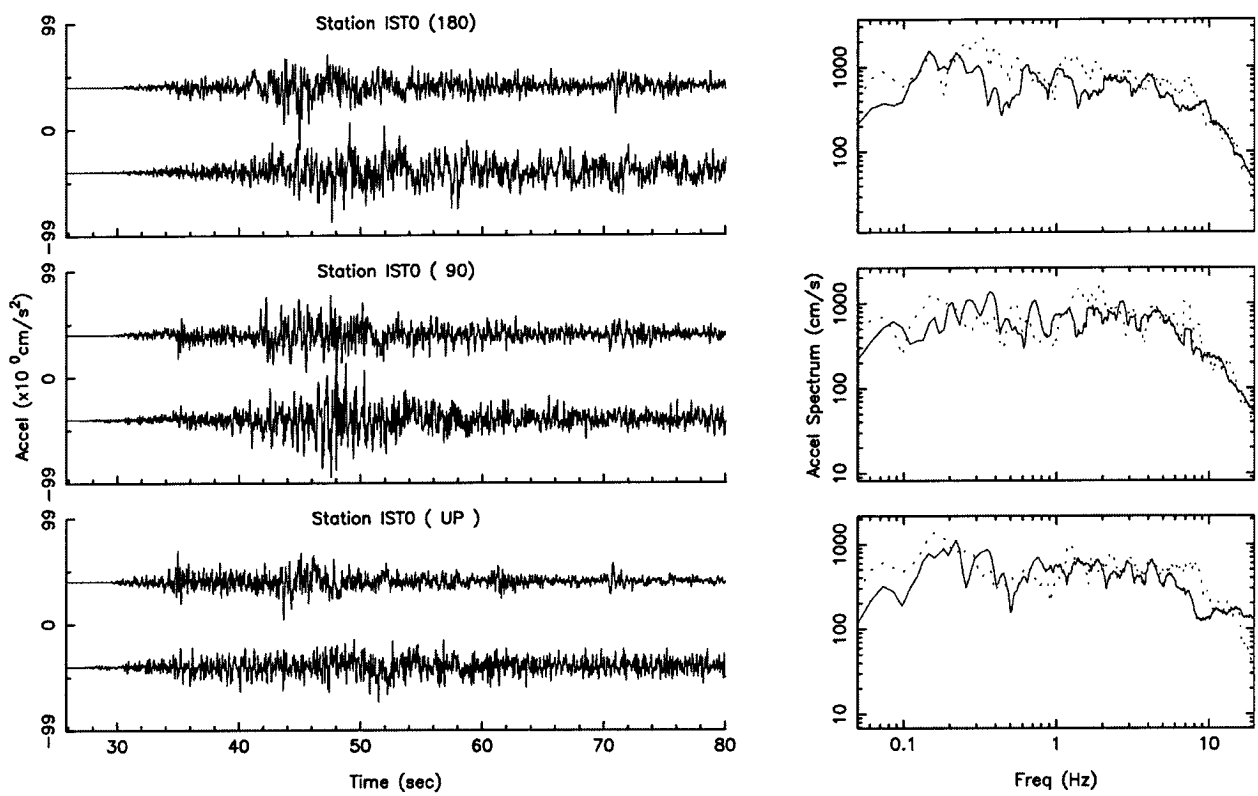

Figure 9. Continue.

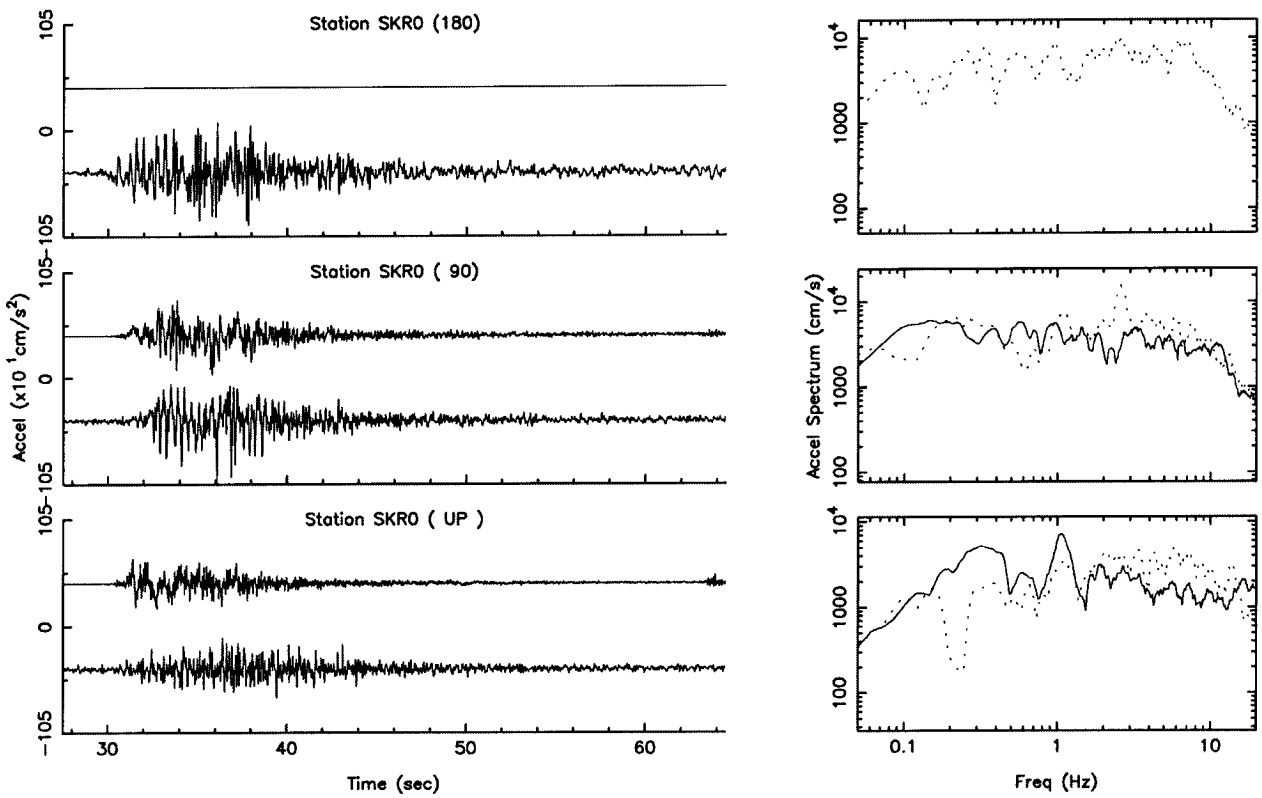

Figure 9. Continue.

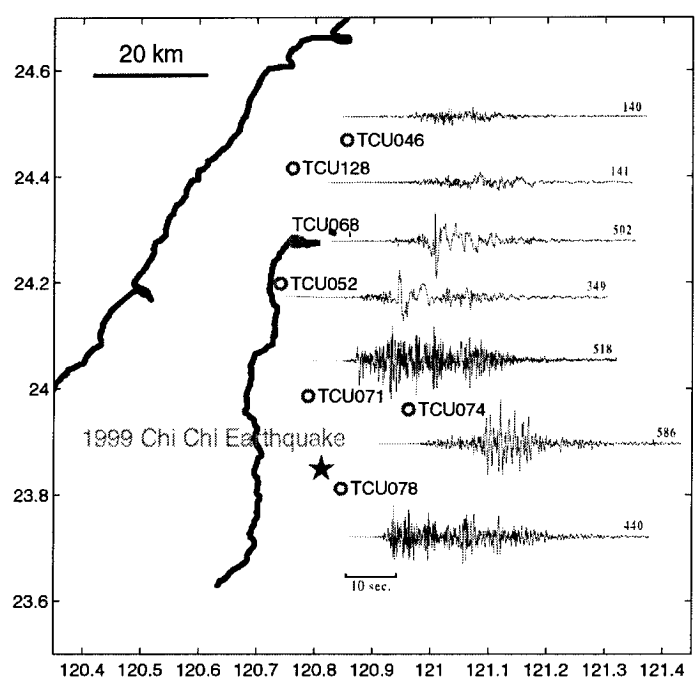

Figure 10. Examples of the strong motion accelerations from the Chi-Chi mainshock. Open circles are station locations followed by the station names. Numbers on the records indicate maximum accelerations.

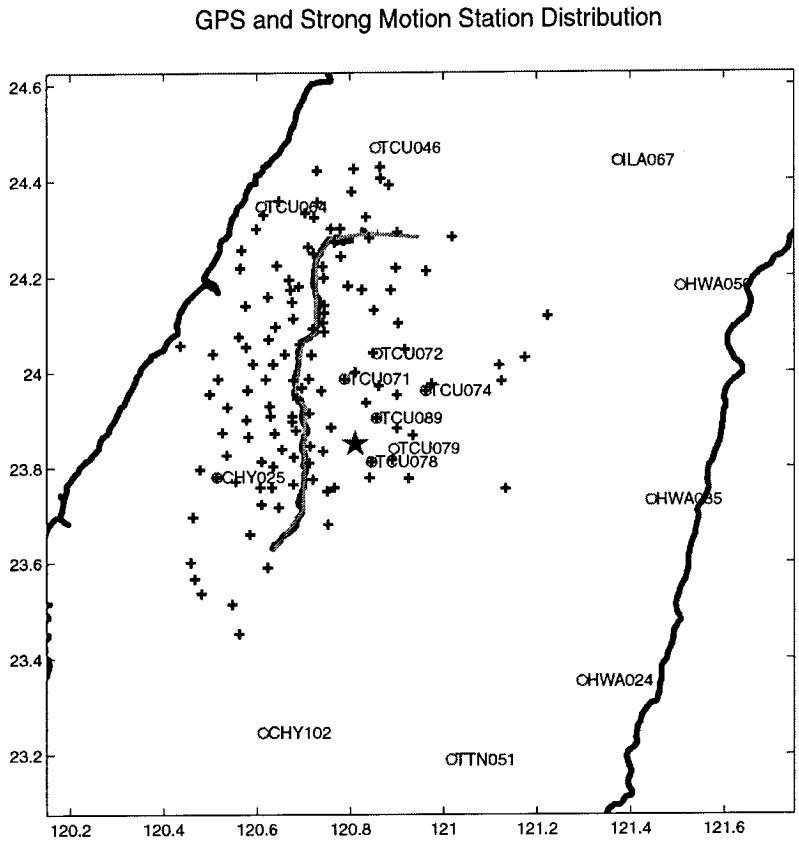

Figure 11. Map view of the surface fault trace and GPS (crosses) and strong motion station (green open circles) distributions.

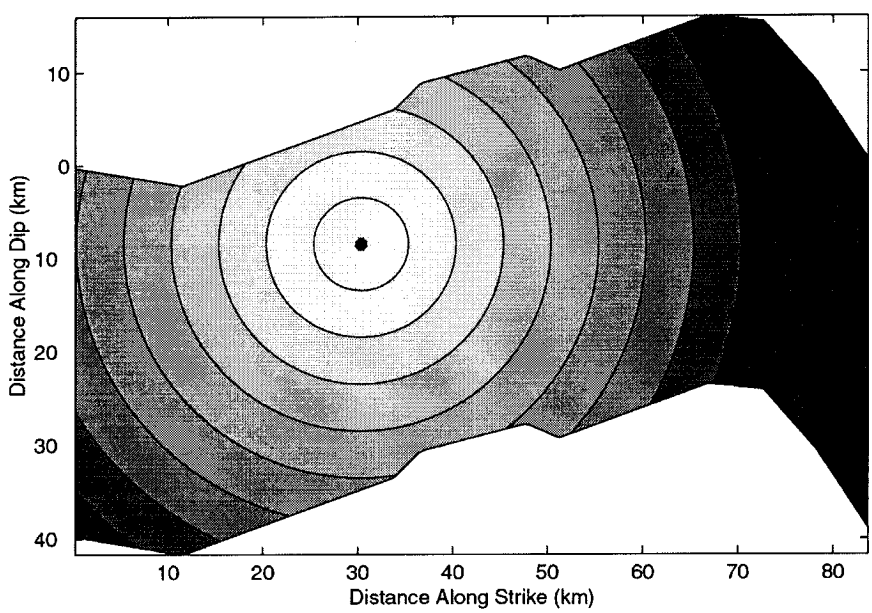

Figure 12. Rupture time contours along the 3-D curved fault for an initial model of constant rupture velocity. The time interval between adjacent contours is 2 seconds.

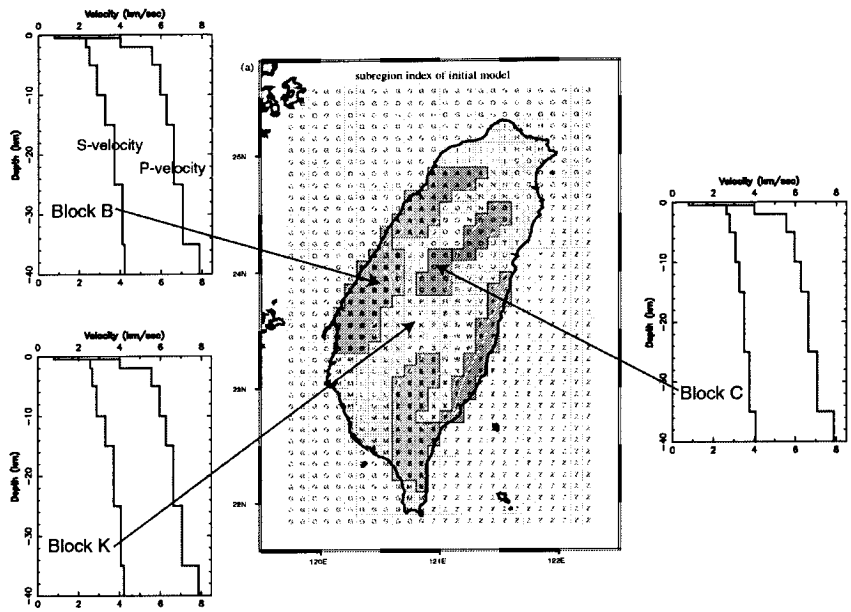

Figure 13. Velocity model for the Taiwan island (Chen et al., 1998)

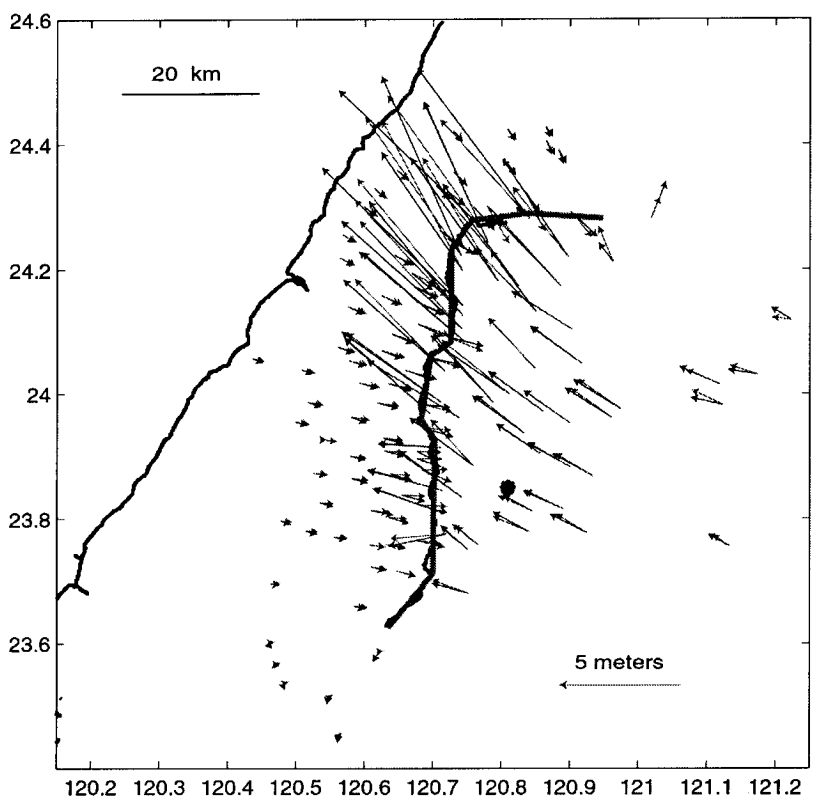

Figure 14. Comparison between observed (GPS and Strong Motion) and synthetic horizontal static ground deformation of the Chi Chi earthquake.

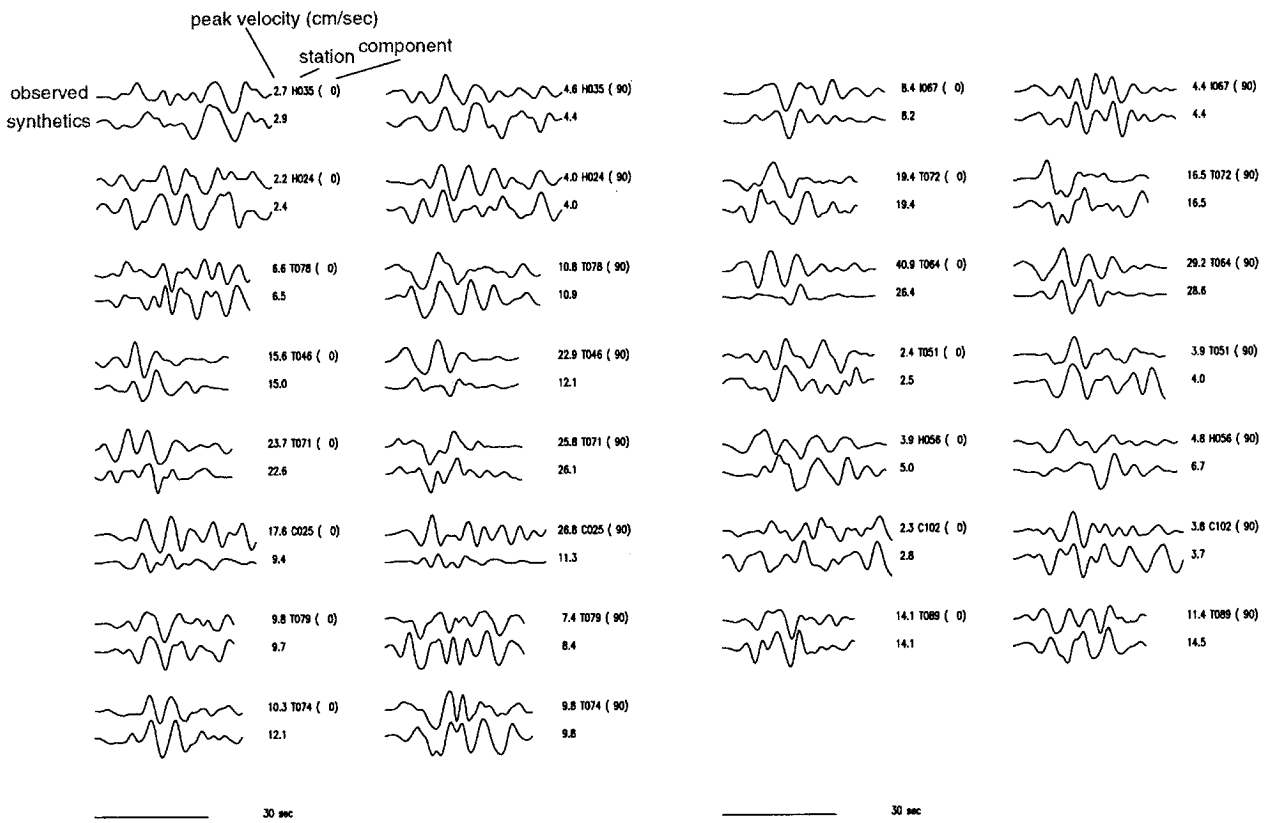

Figure 15. Comparison between synthetic and observed ground velocity waveforms. The traces within each panel correspond to different components of velocity seismograms. The observed seismograms are plotted above the synthetics for each station. The peak velocities (in cm/sec) are shown to the right of the seismograms followed by their station names and the orientation (in degrees) of components measured from north.

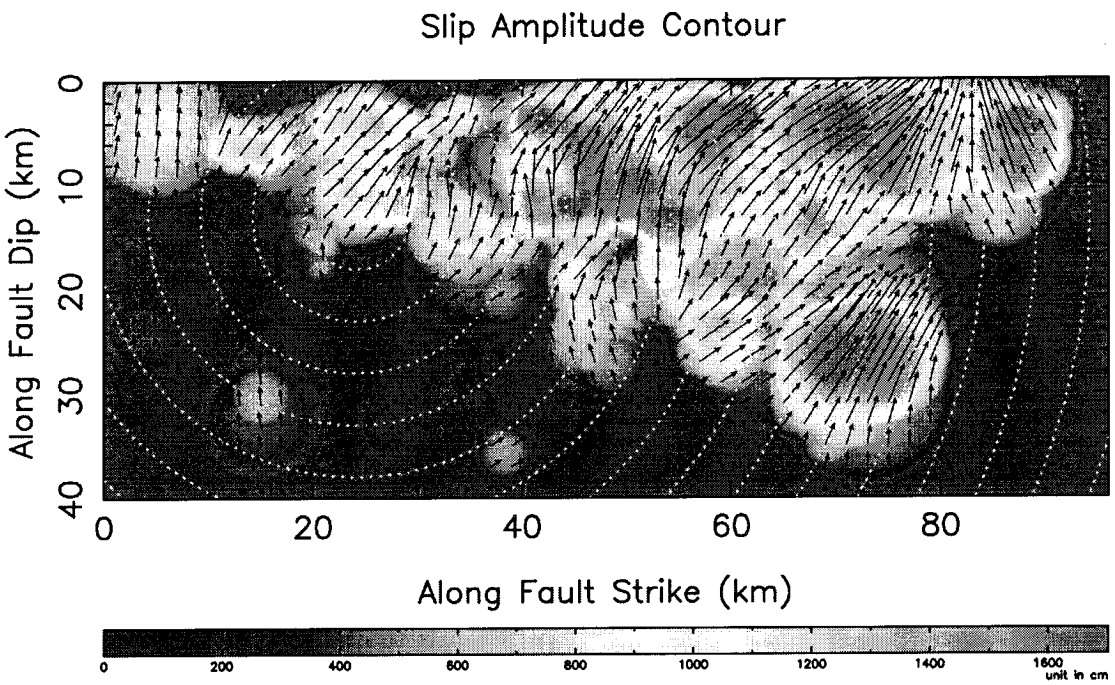

Figure 16. The final slip amplitude and slip vector distributions of the Chi-Chi earthquake composite soruce model.

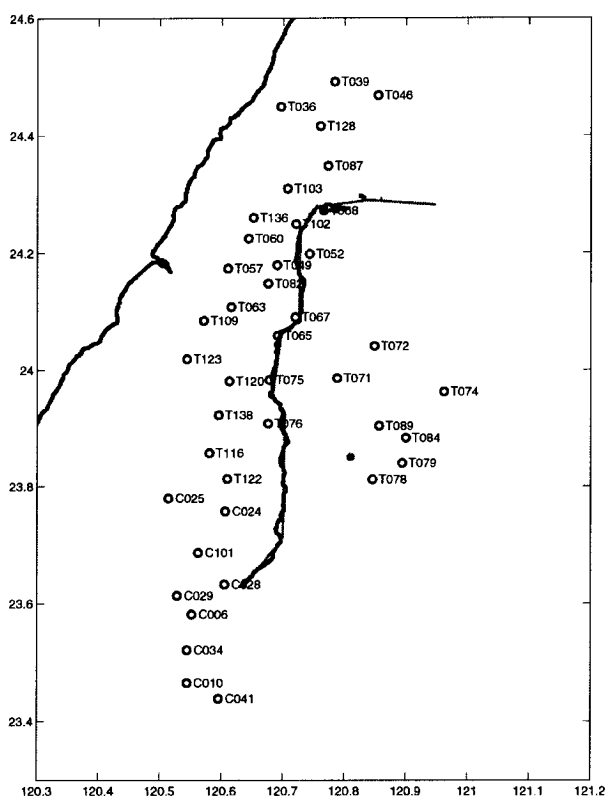

Figure 17. Map view of the strong motion station distribution. These stations are used for predicting the near-field ground motion using the Chi-Chi composite source model.

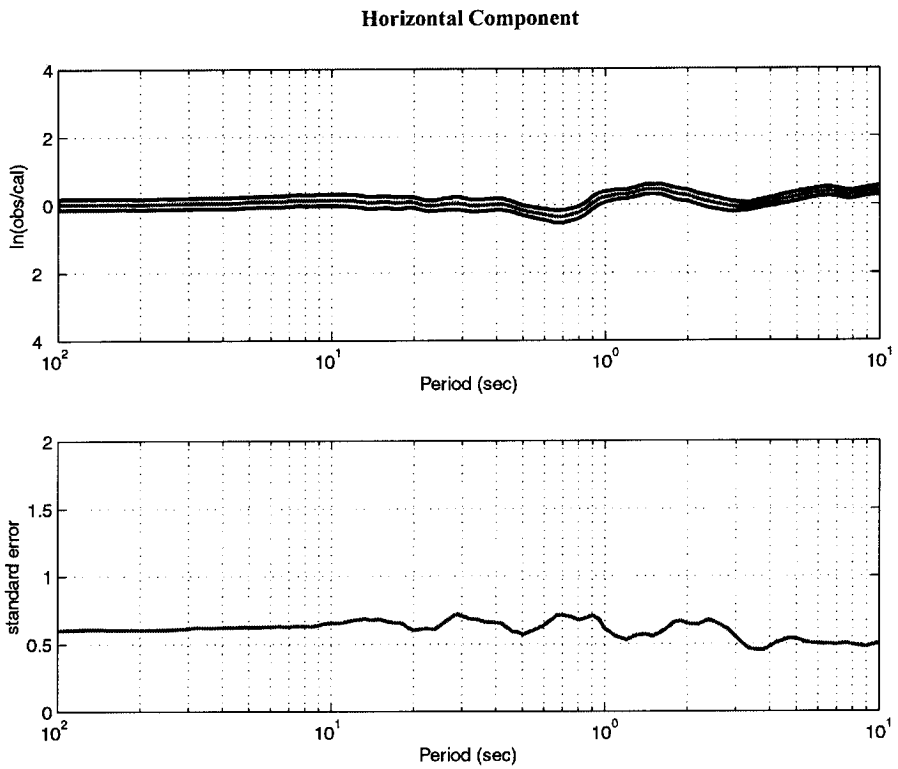

Figure 18a. The upper panel plots biases (red) and its 90% confidence limits (black) of the prediction for the horizontal component. The lower panel plots the standard errors.

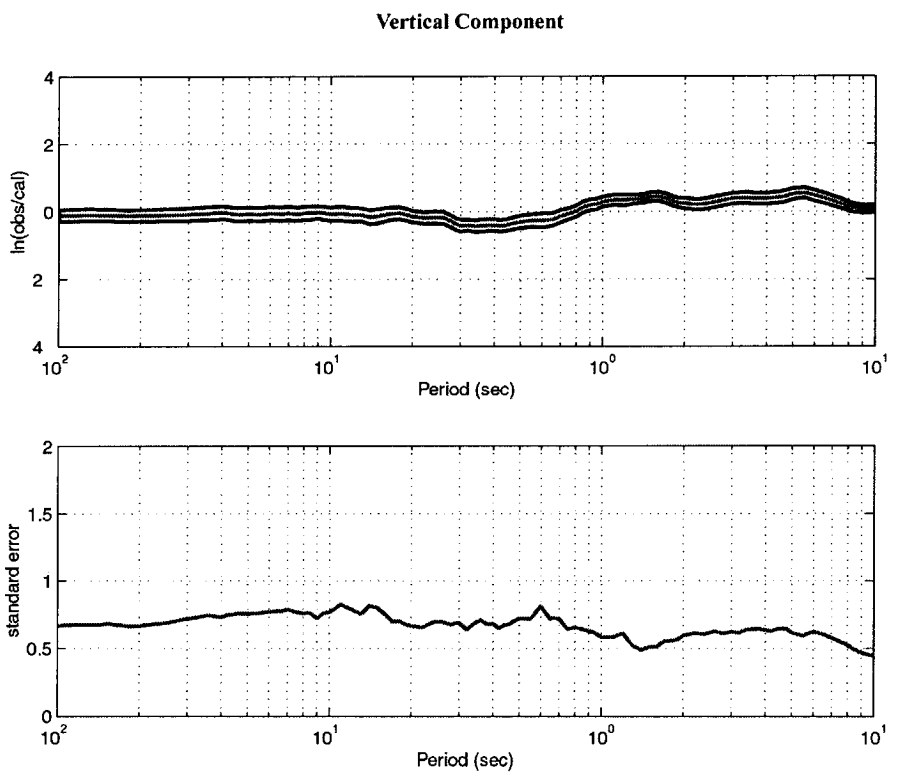

Figure 18b. Same as Figure 18a but for the vertical component.

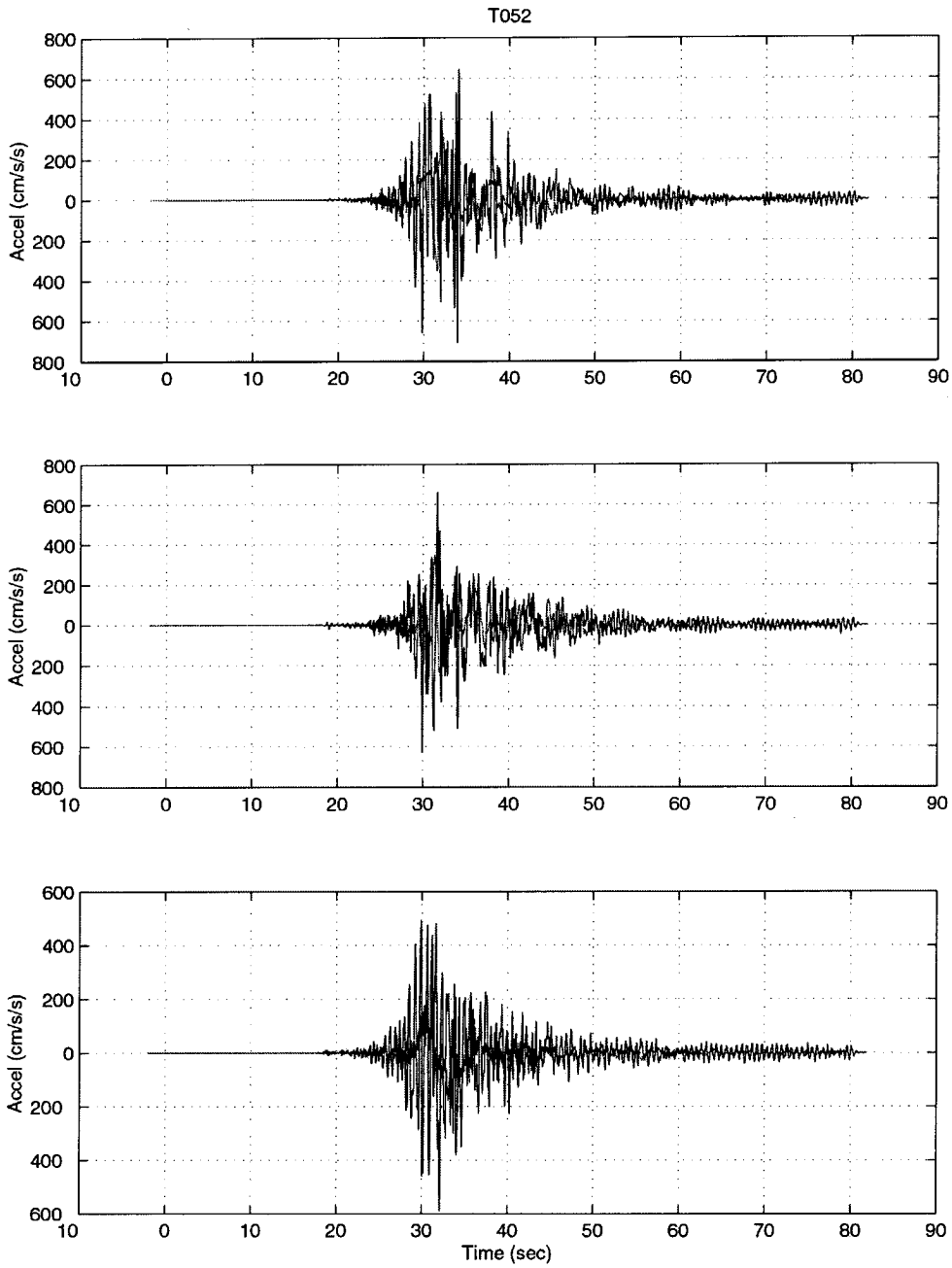

Figure 19a. Comparison between the observed (red) and synthetic (blue) ground accelerations at station T052. Top panel is for the NS component. Middle panel is for the EW component. Bottom panel is for the vertical component.

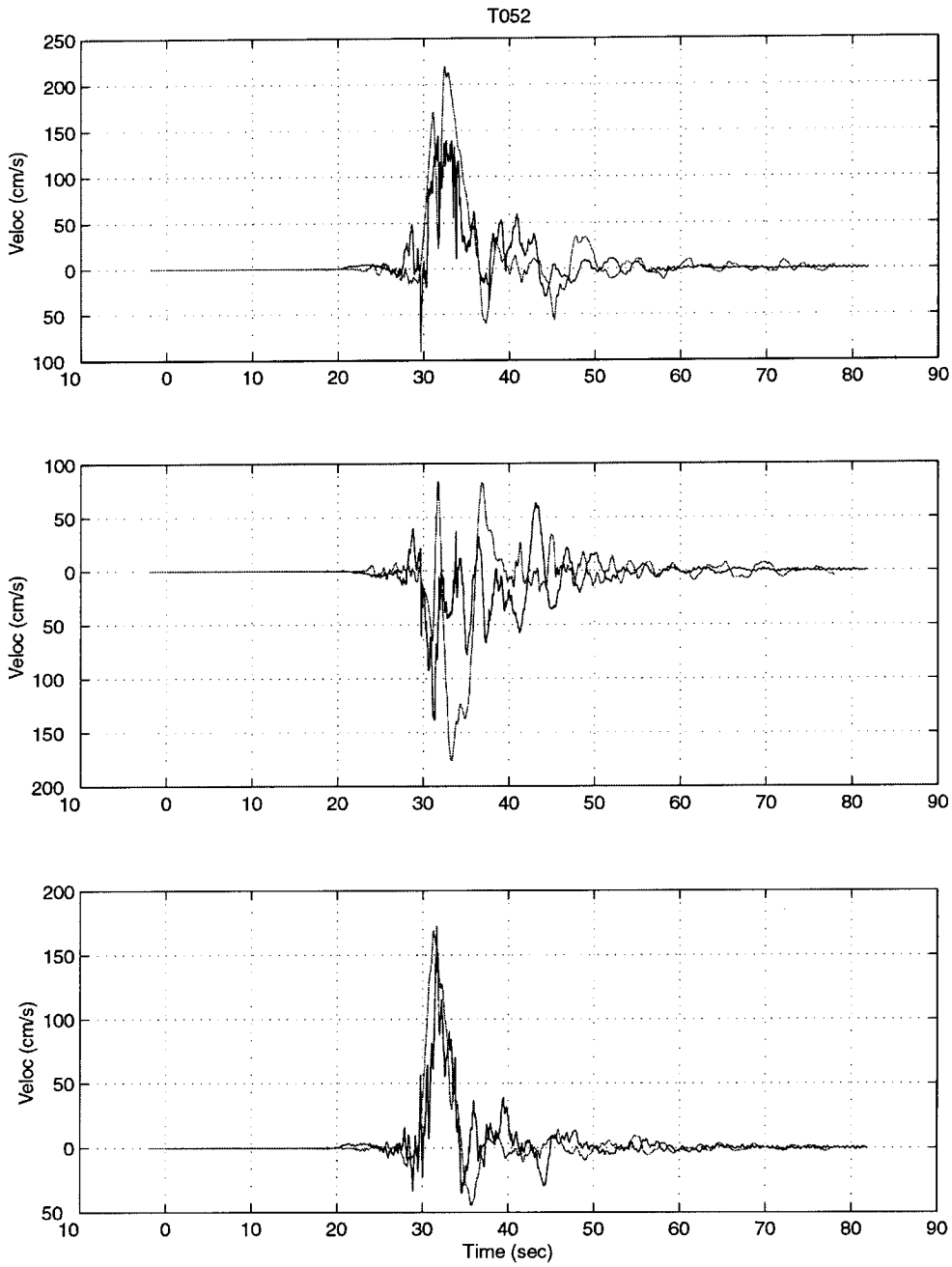

Figure 19b. Same as Figure 19a but for the ground velocities.

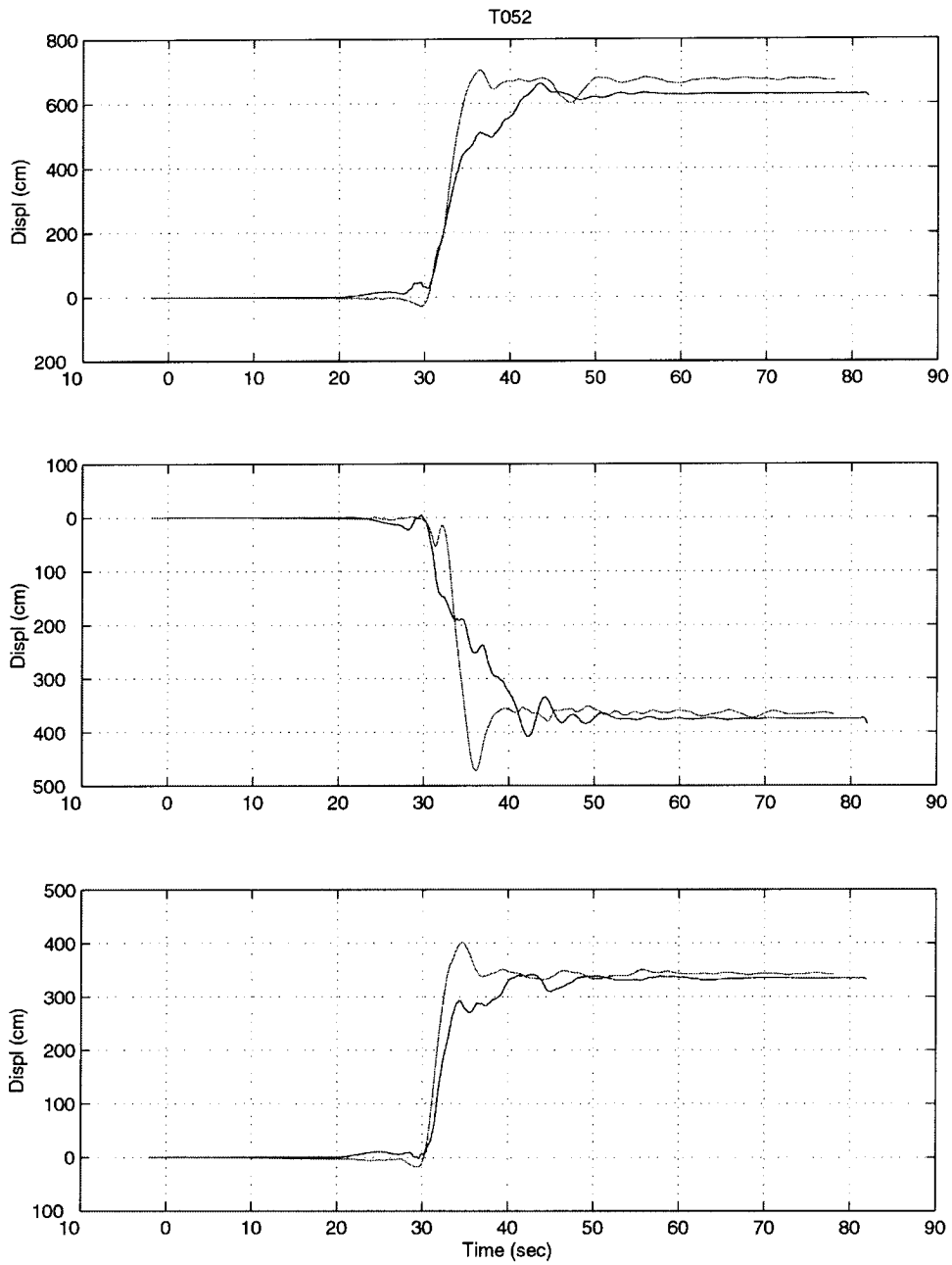

Figure 19c. Same as Figure 19a but for the ground displacements.

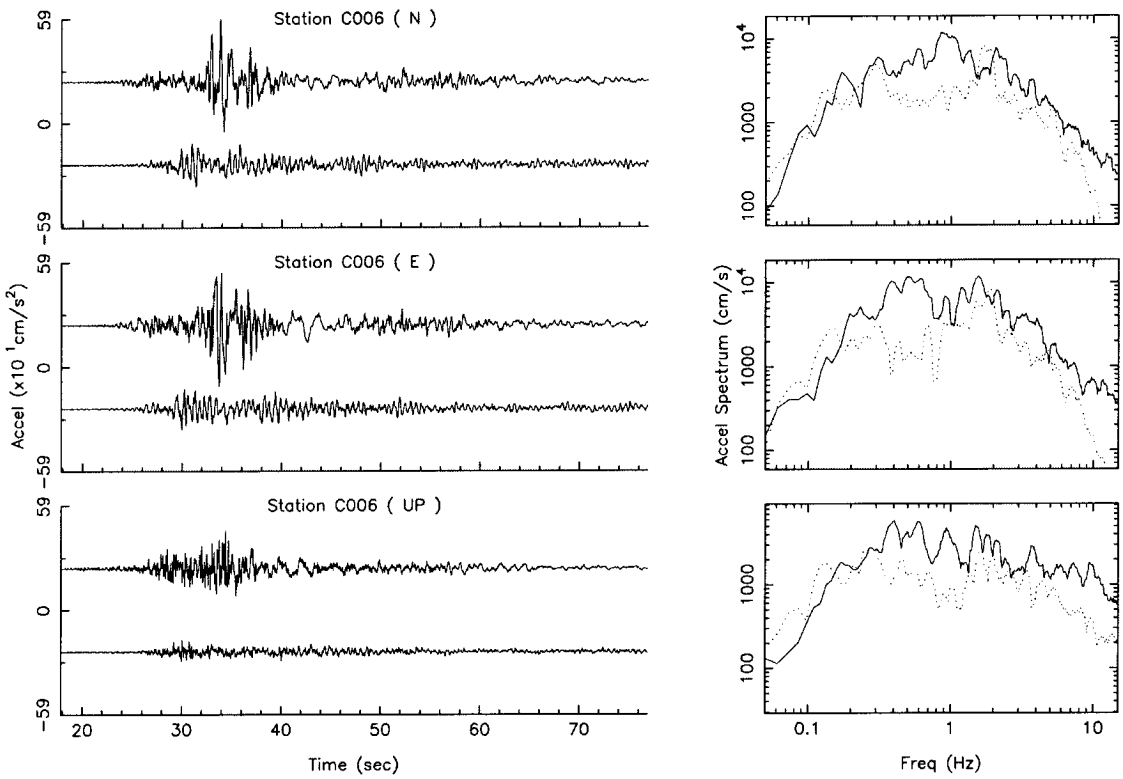

Figure 20. Comparison of acceleration time series and their Fourier amplitudes between the synthetics and the observation for all stations. For each component, the synthetic seismograms are plotted below the observation. The observed Fourier spectra are plotted in solid lines and the synthetics are plotted in dotted lines.

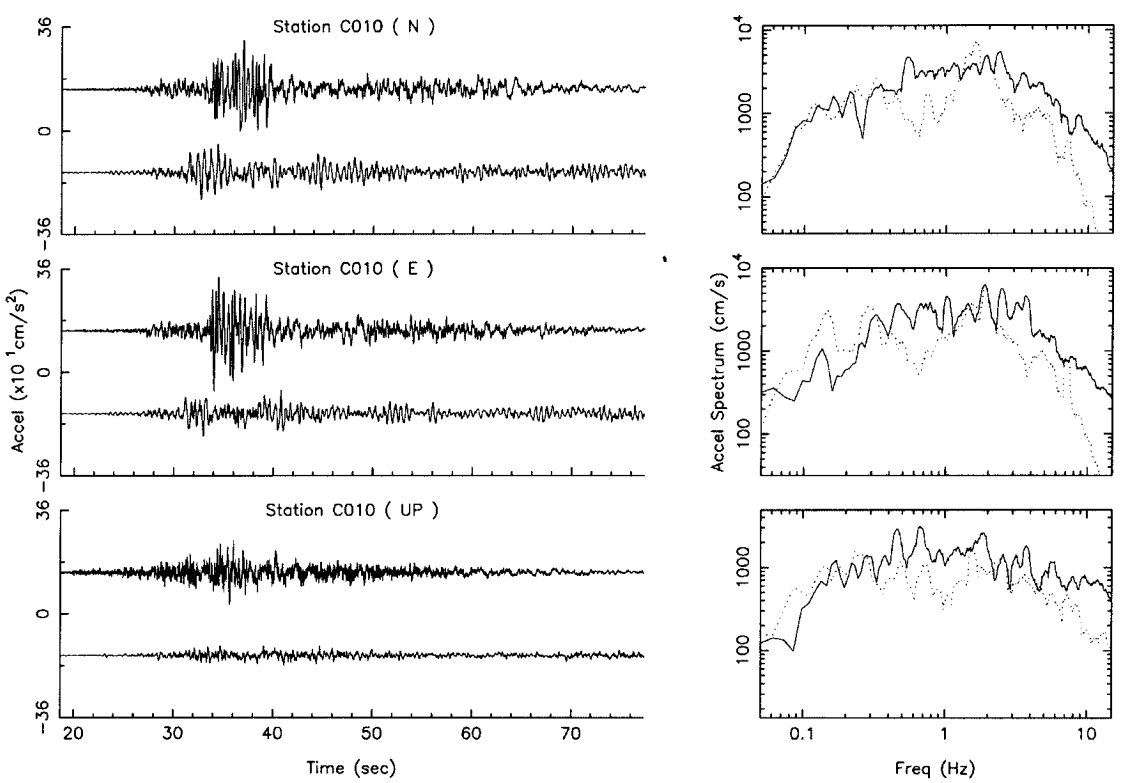

Figure 20. Continue.

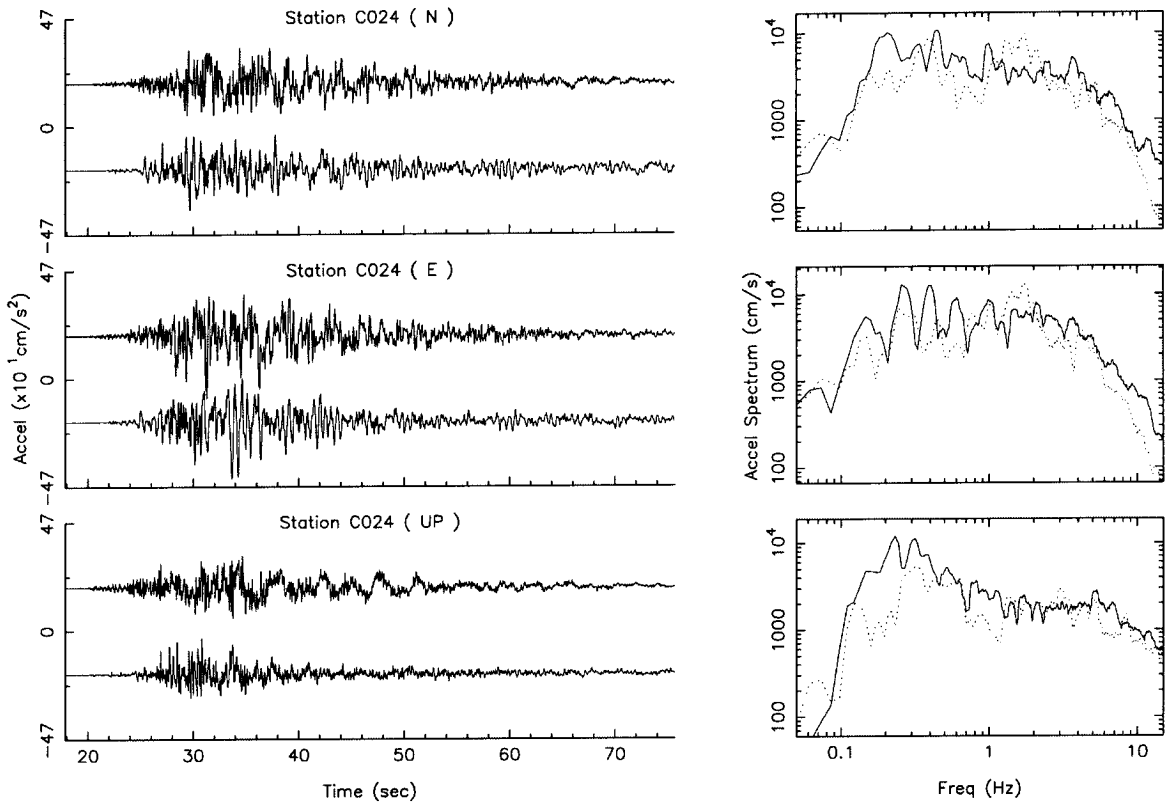

Figure 20. Continue.

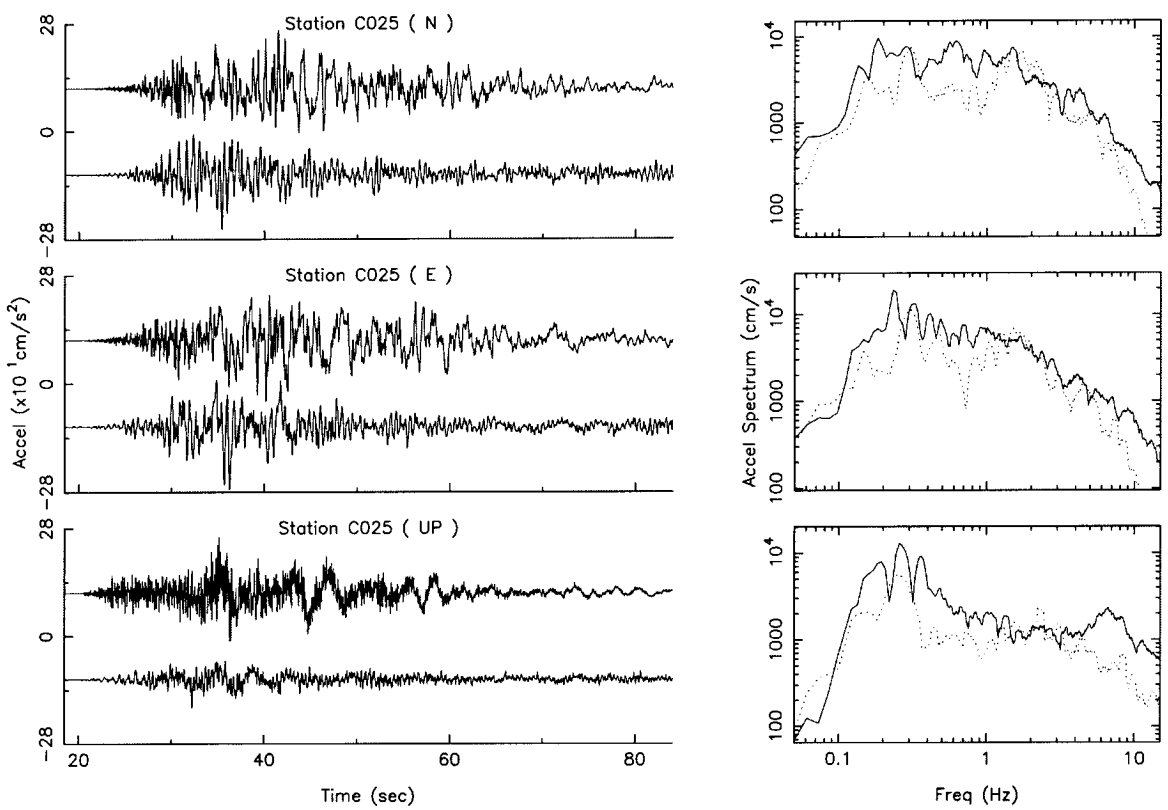

Figure 20. Continue.

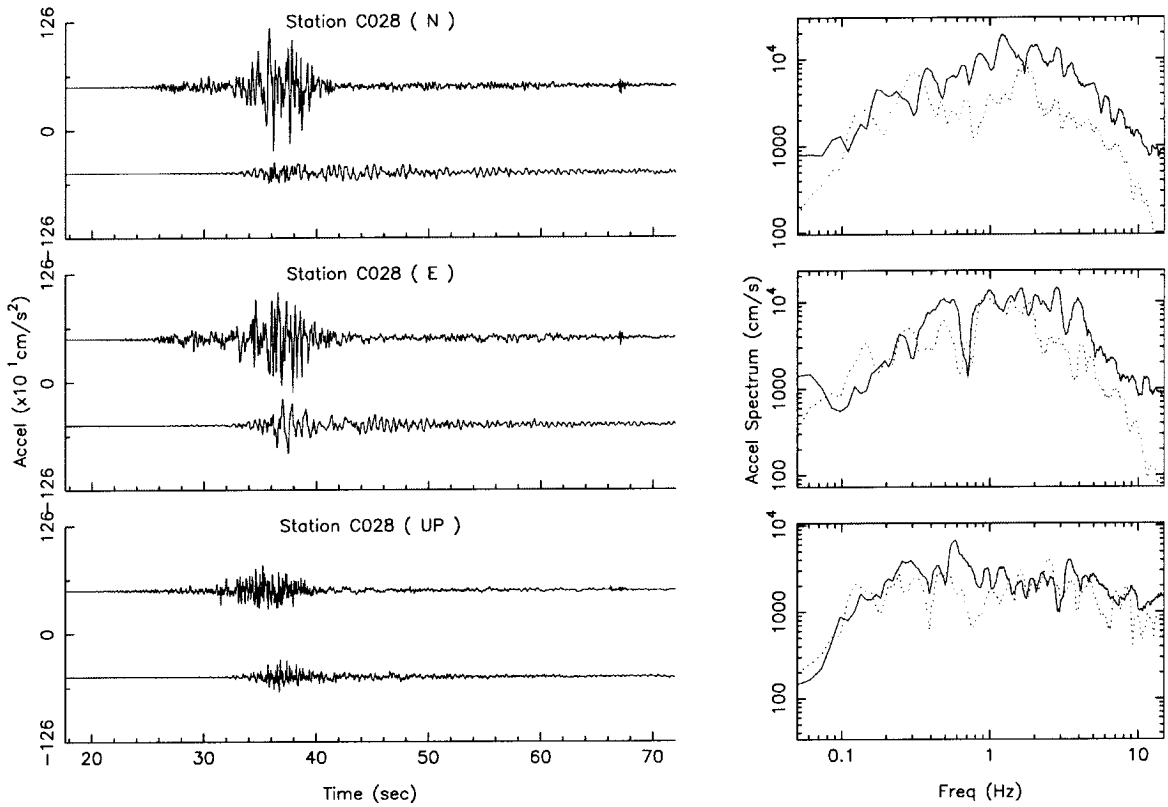

Figure 20. Continue.

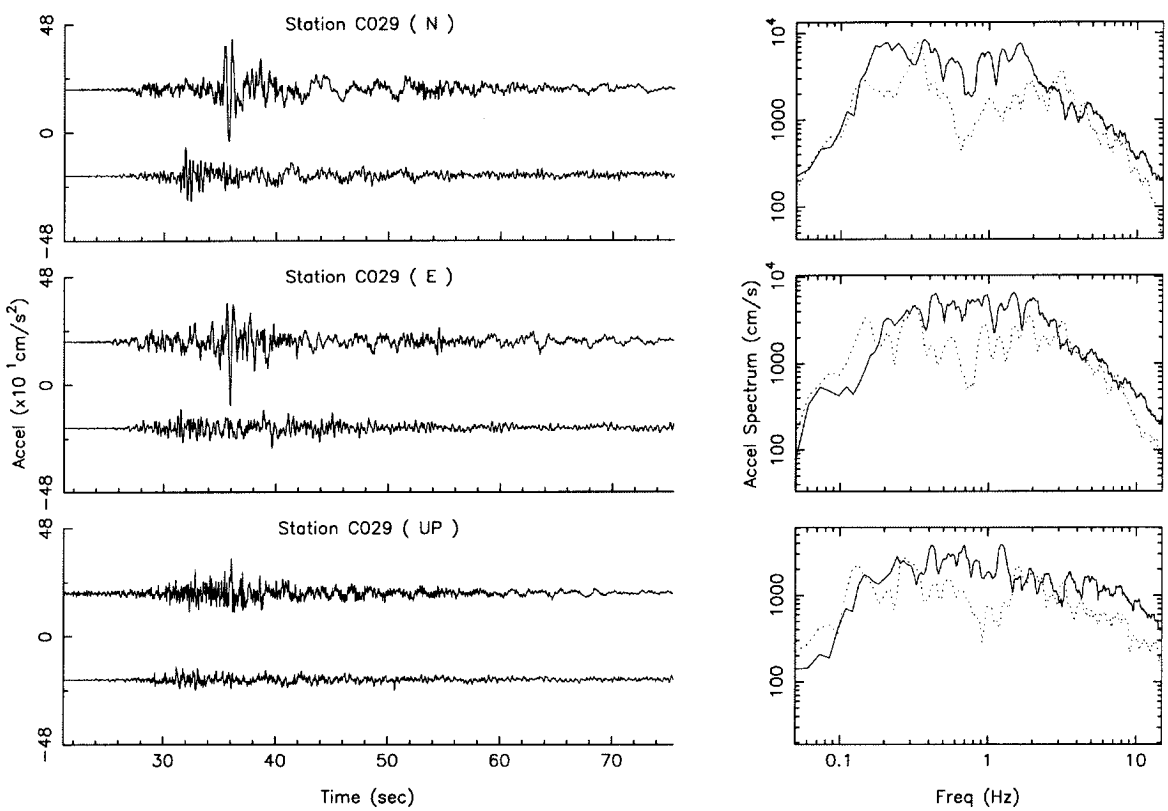

Figure 20. Continue.

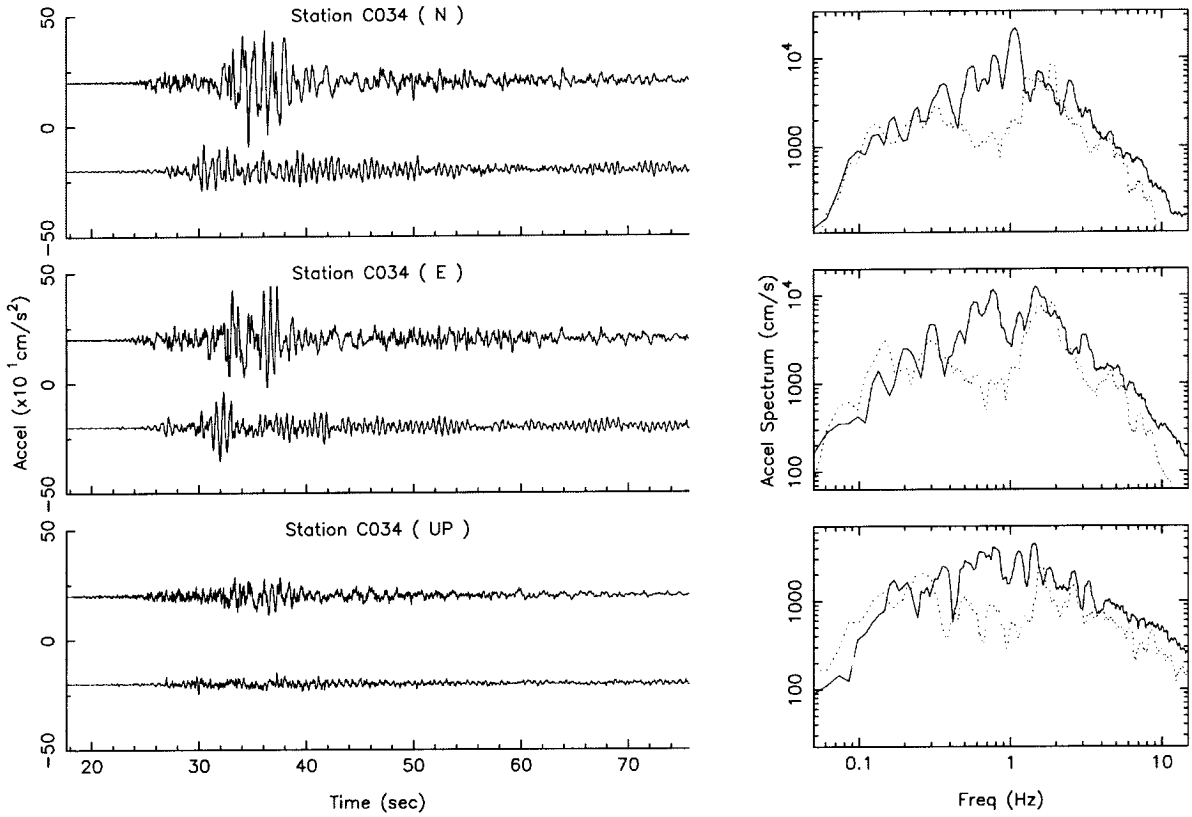

Figure 20. Continue.

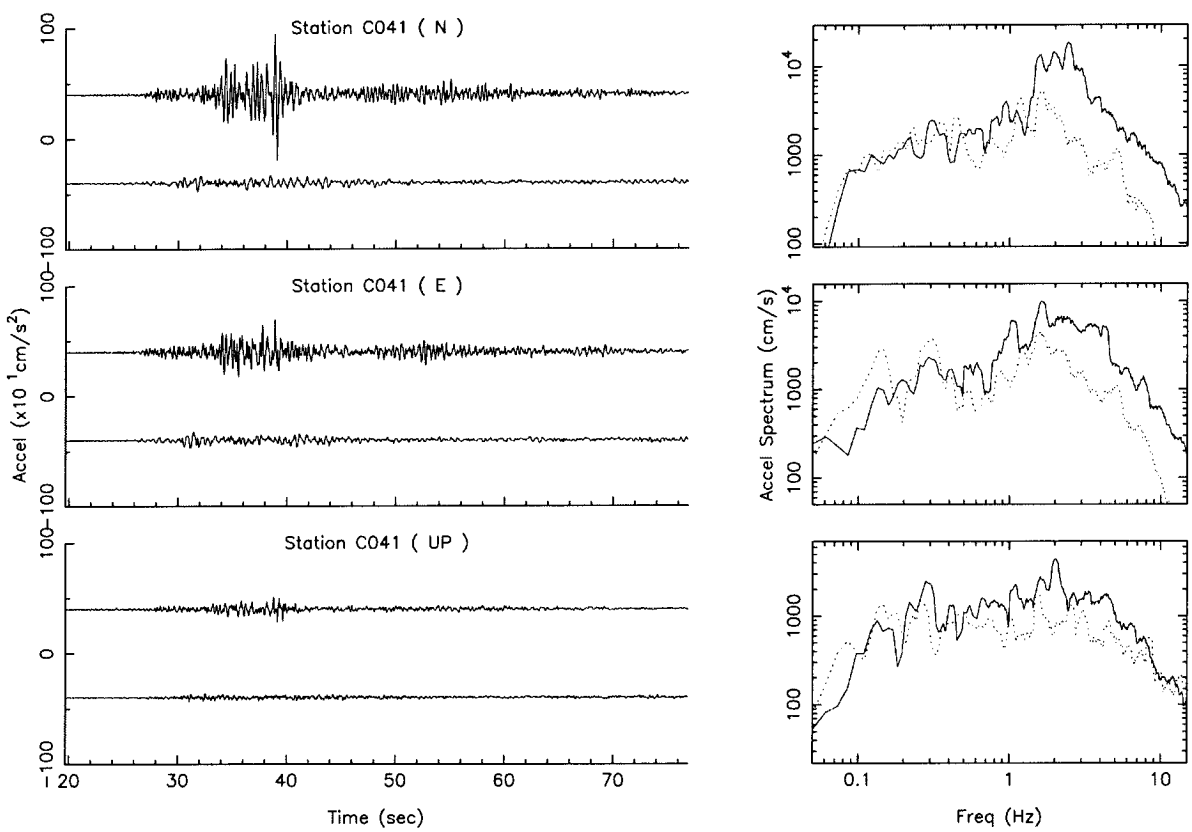

Figure 20. Continue.

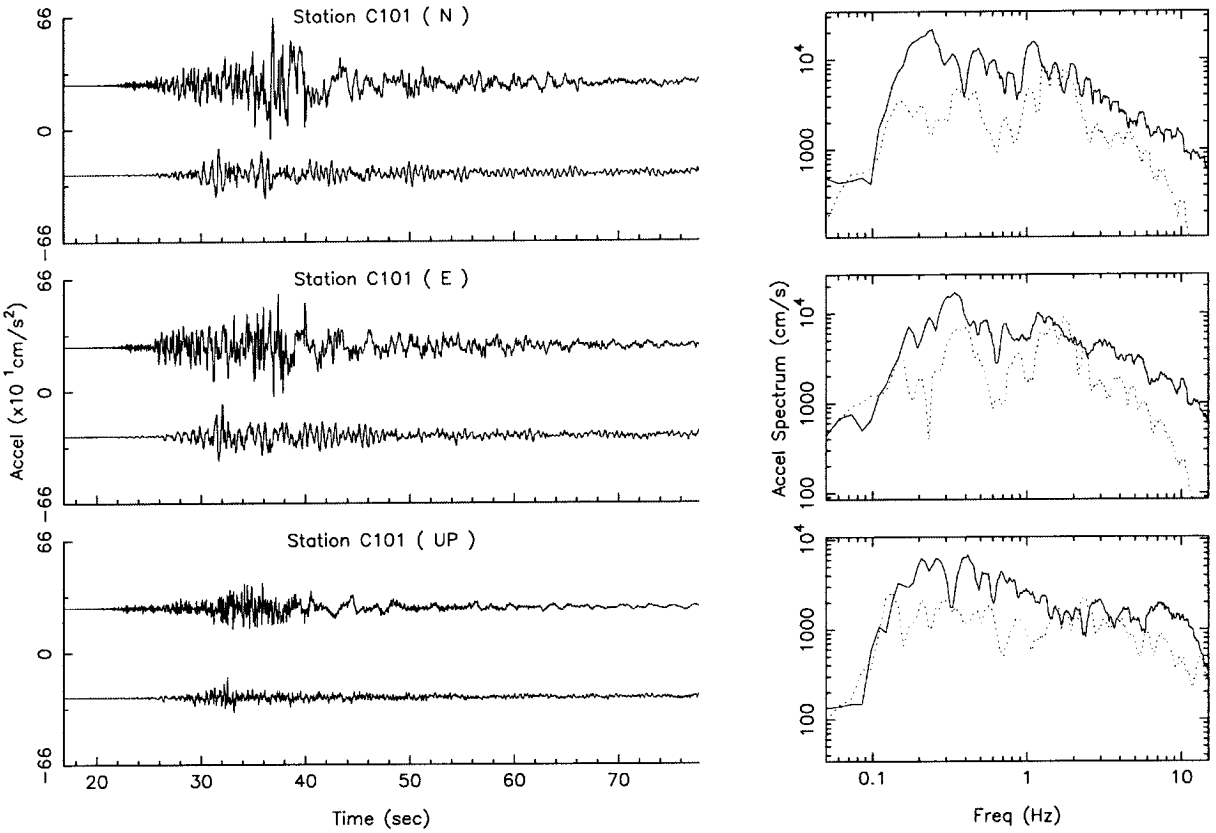

Figure 20. Continue.

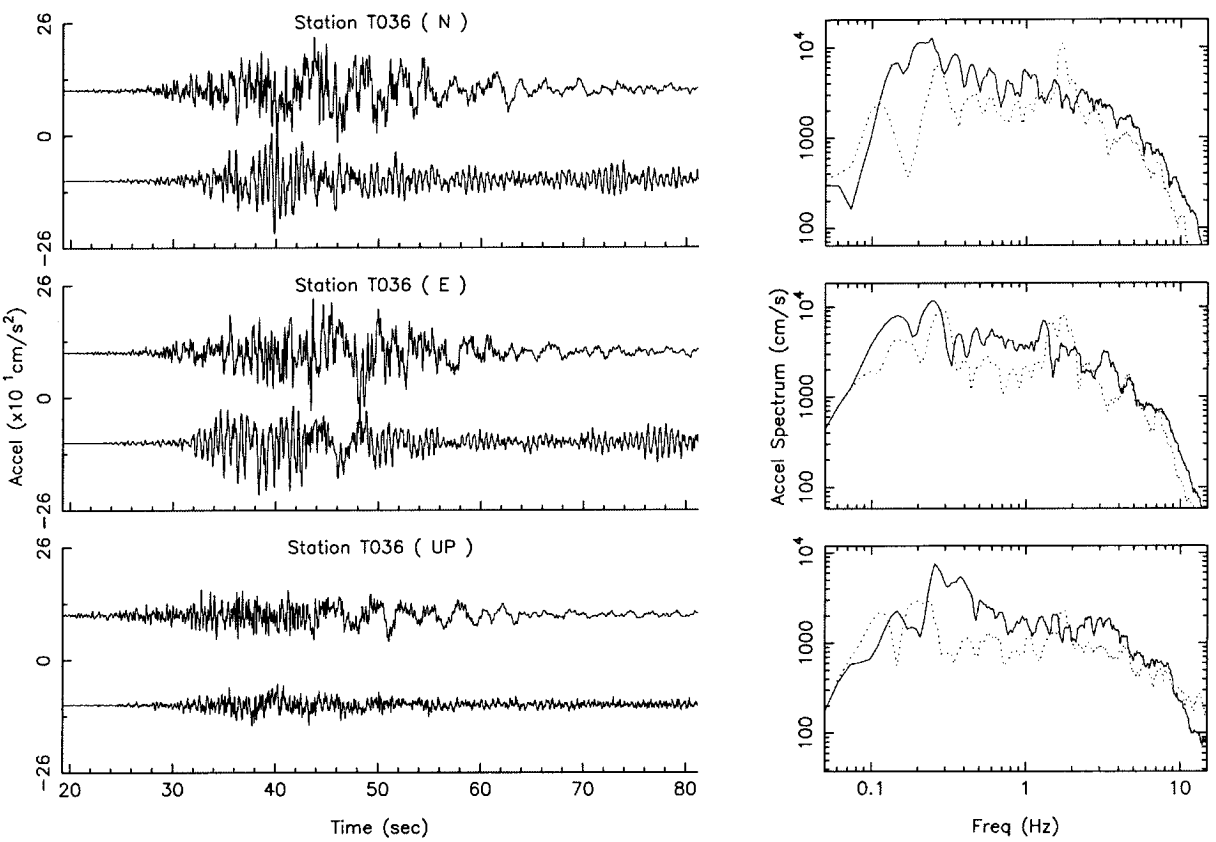

Figure 20. Continue.

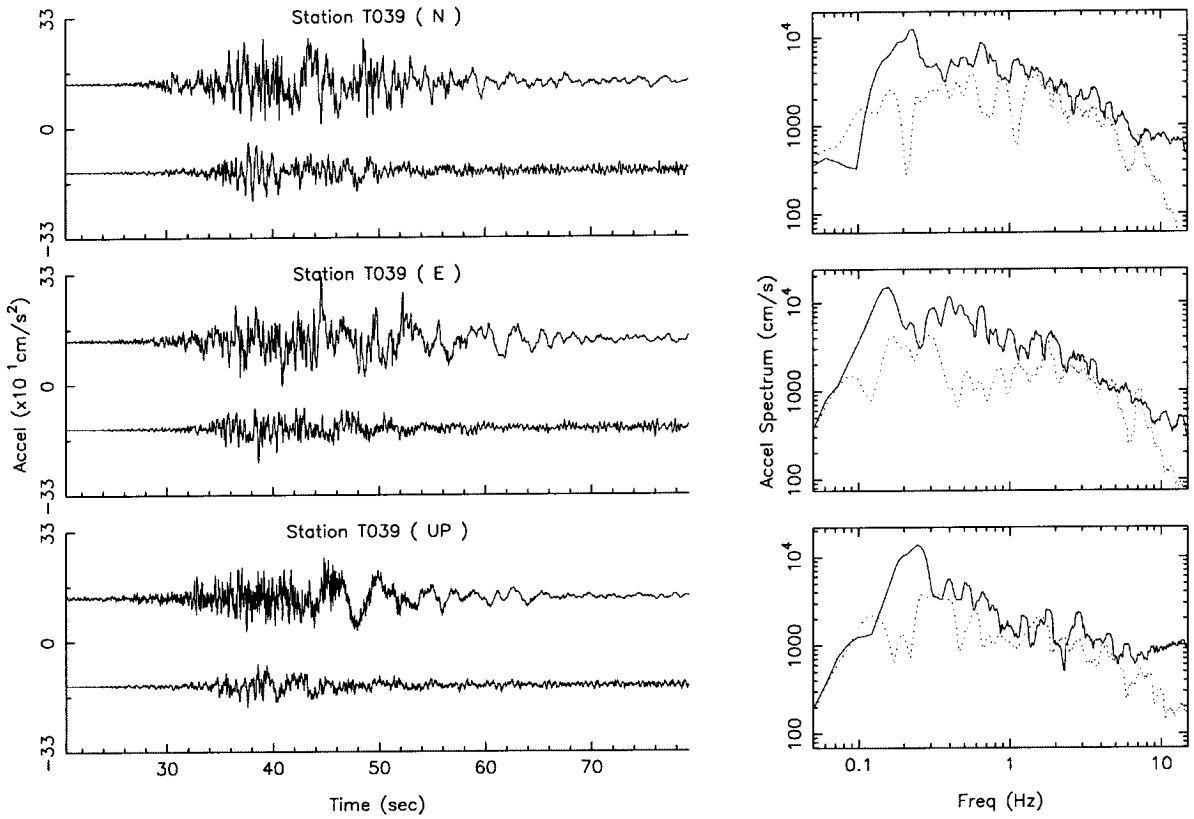

Figure 20. Continue.

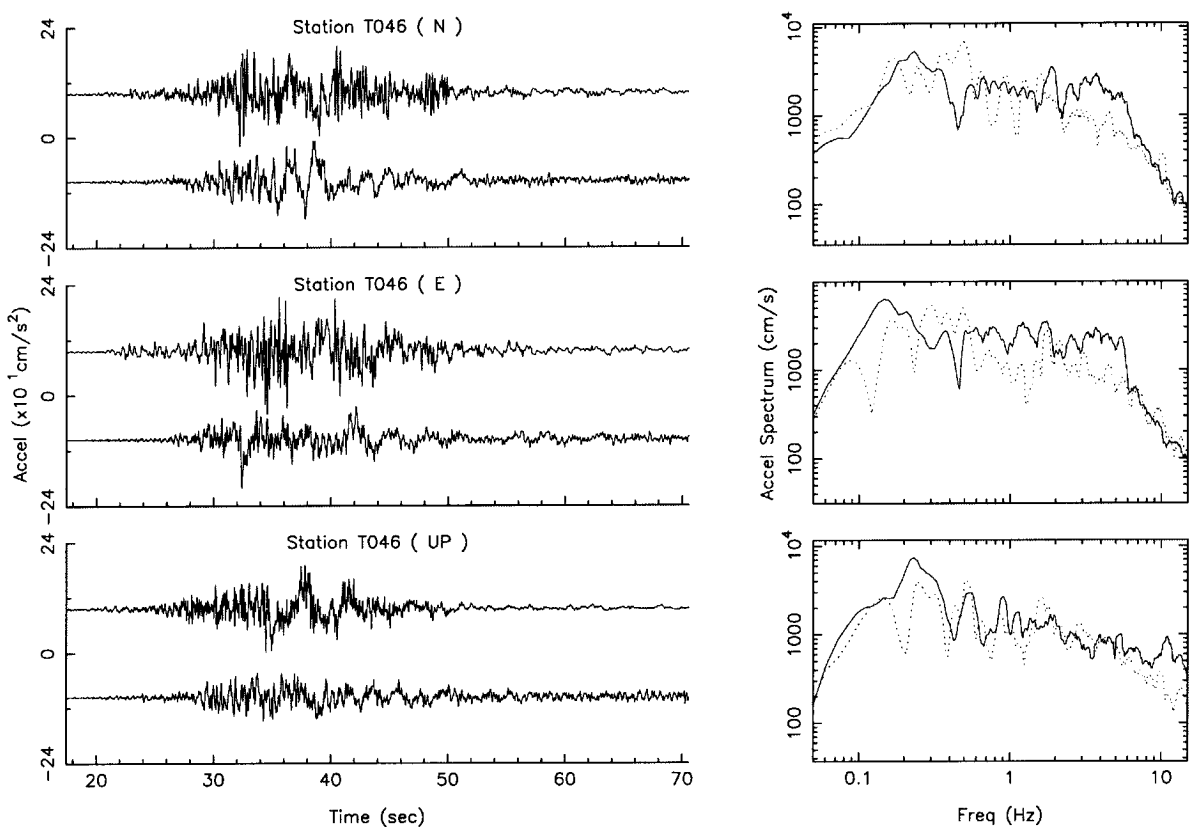

Figure 20. Continue.

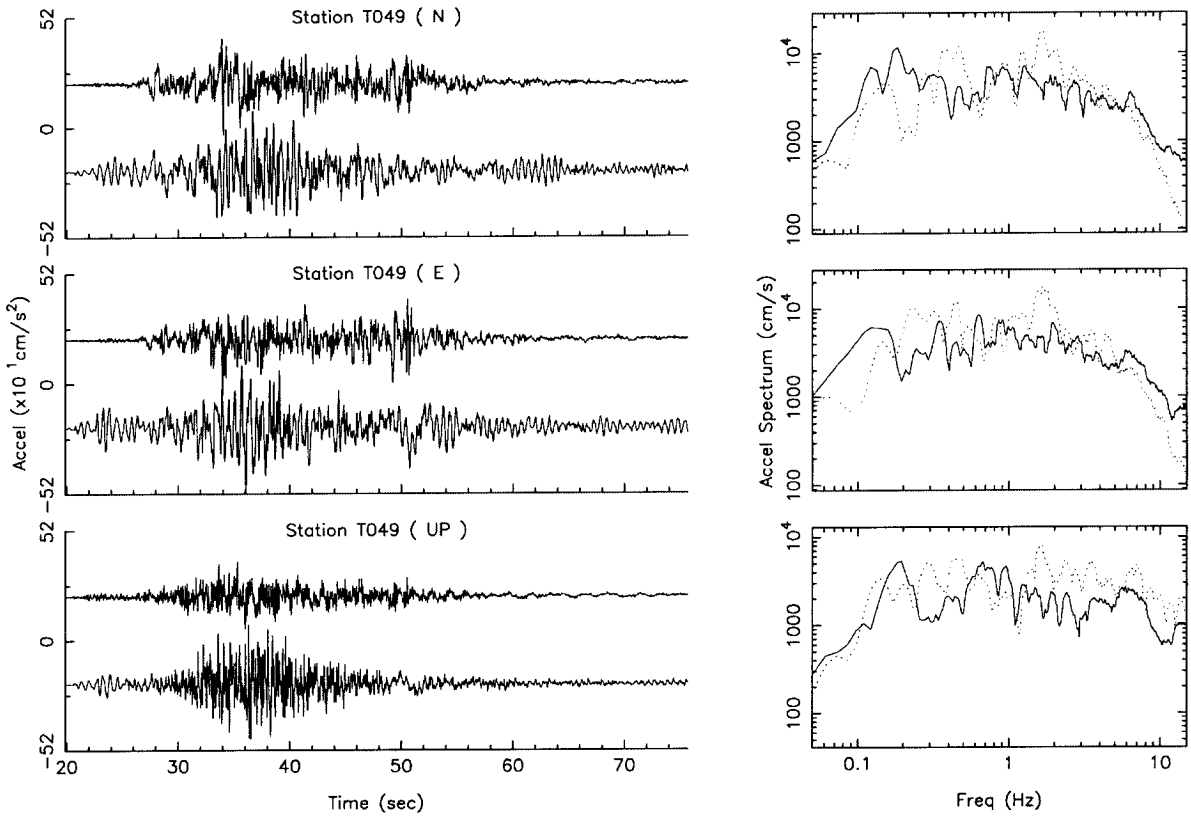

Figure 20. Continue.

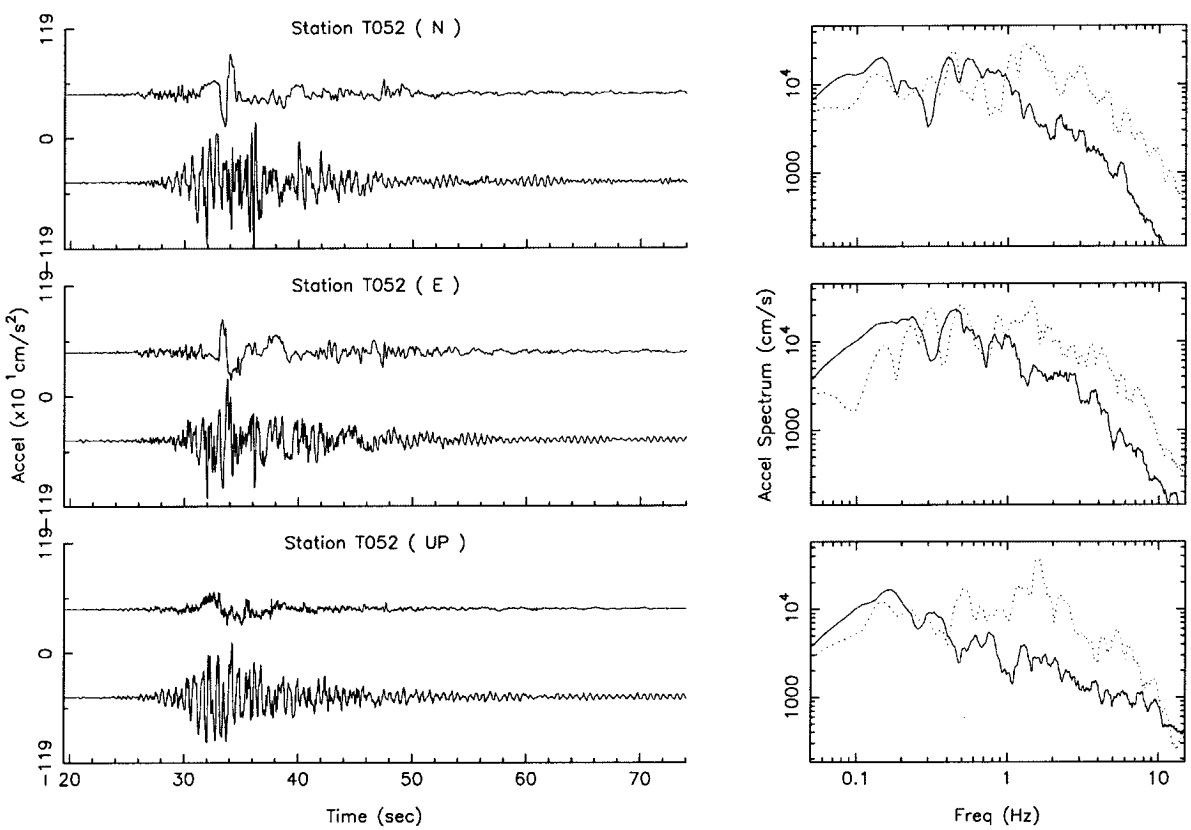

Figure 20. Continue.

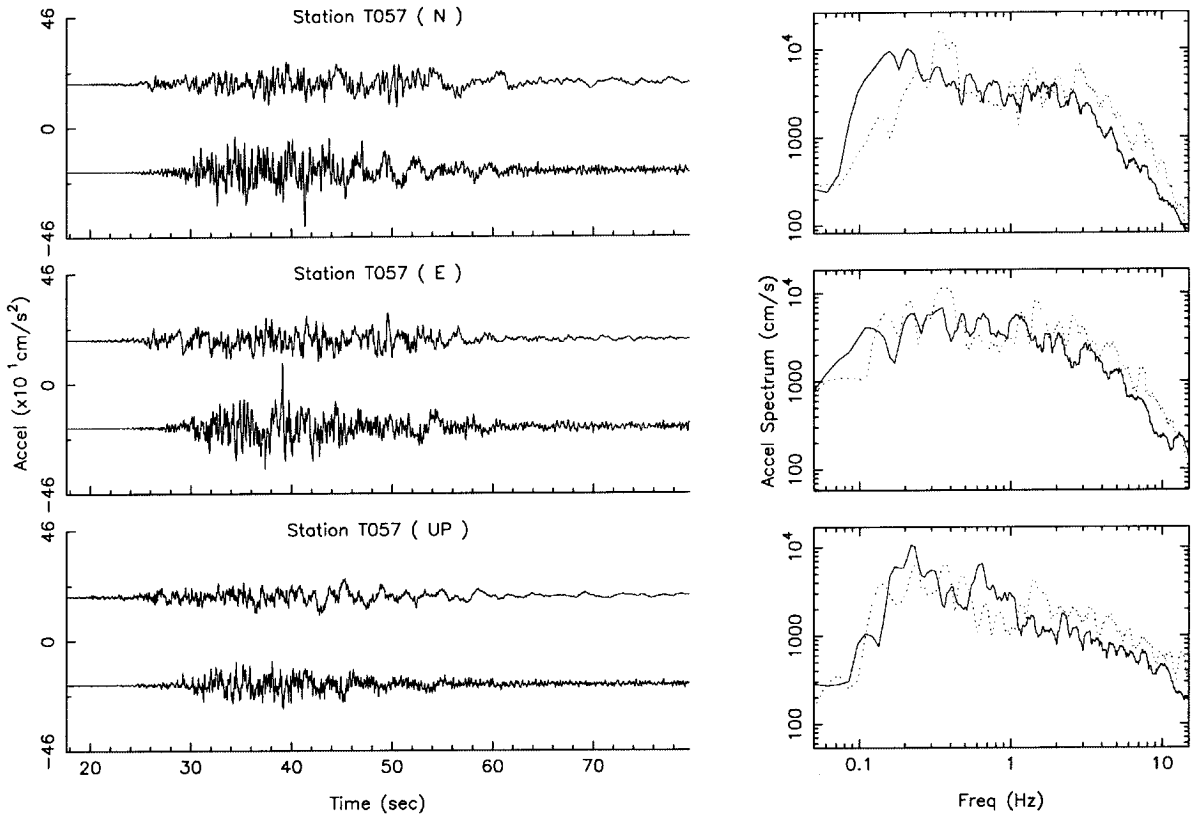

Figure 20. Continue.

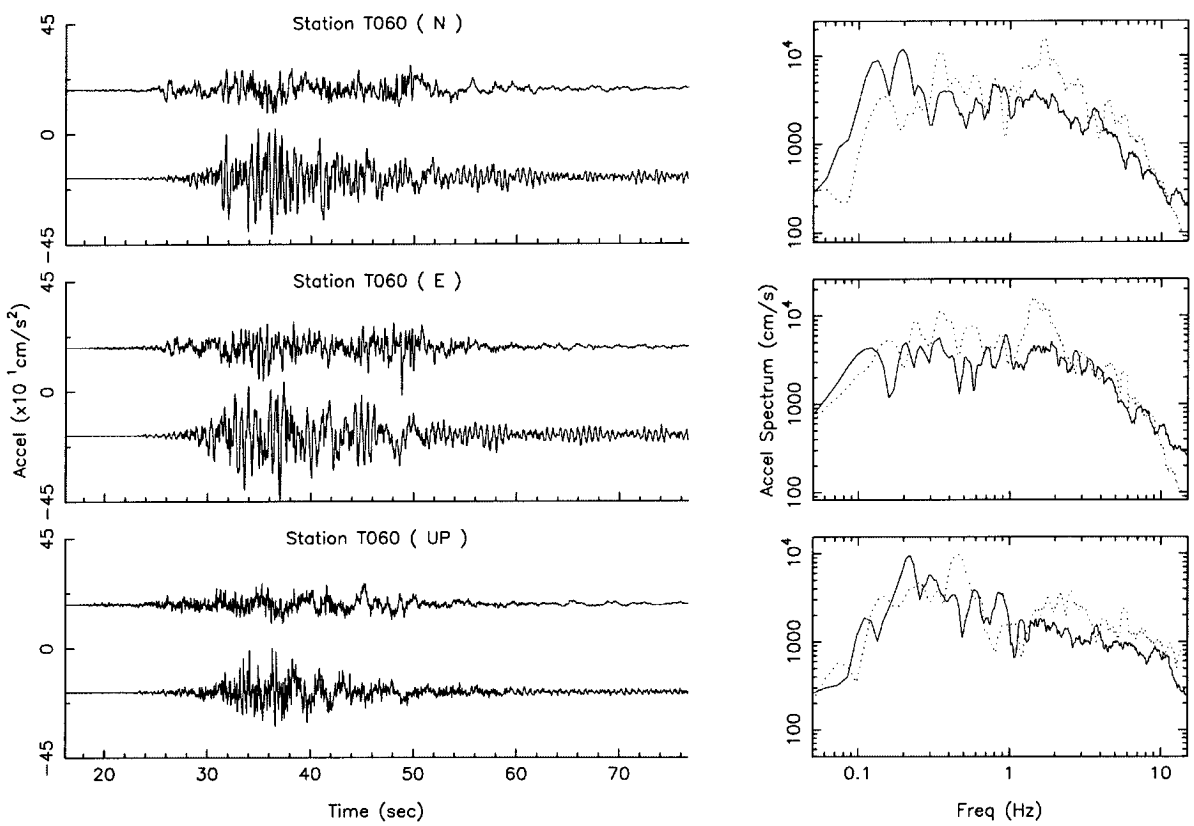

Figure 20. Continue.

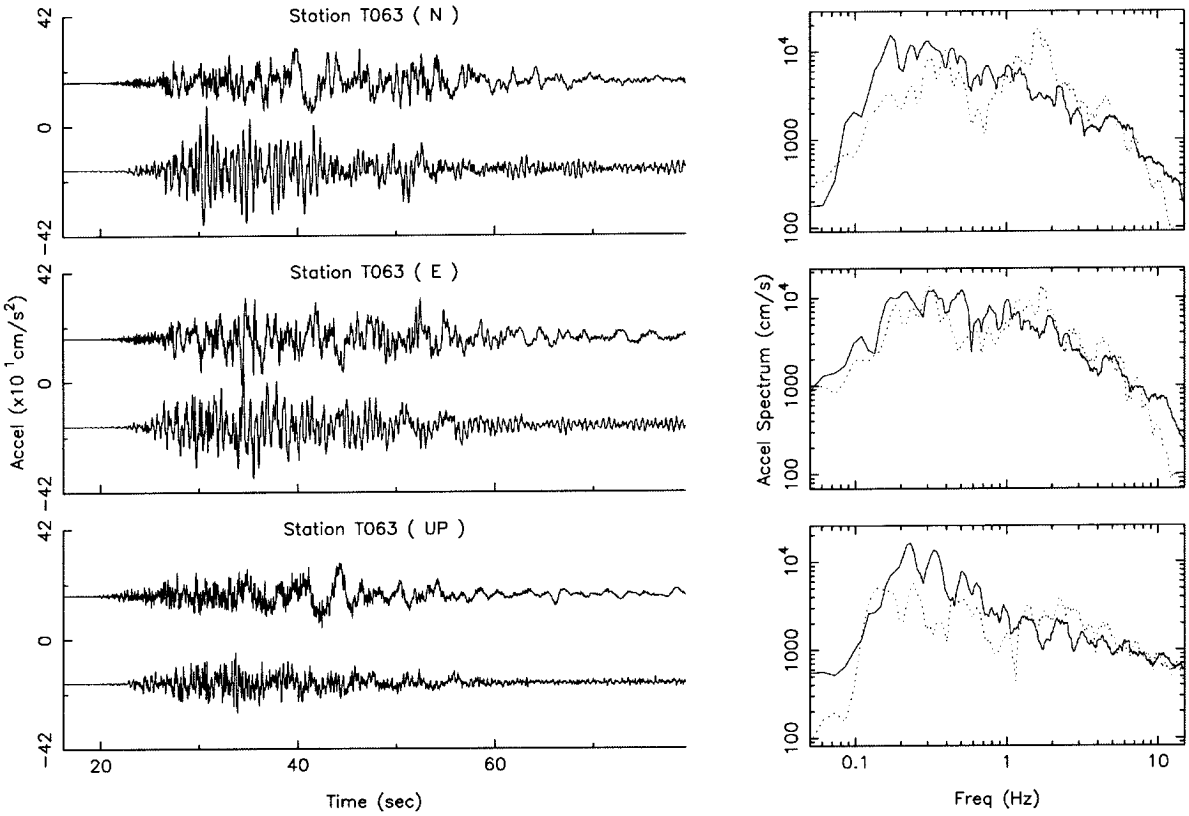

Figure 20. Continue.

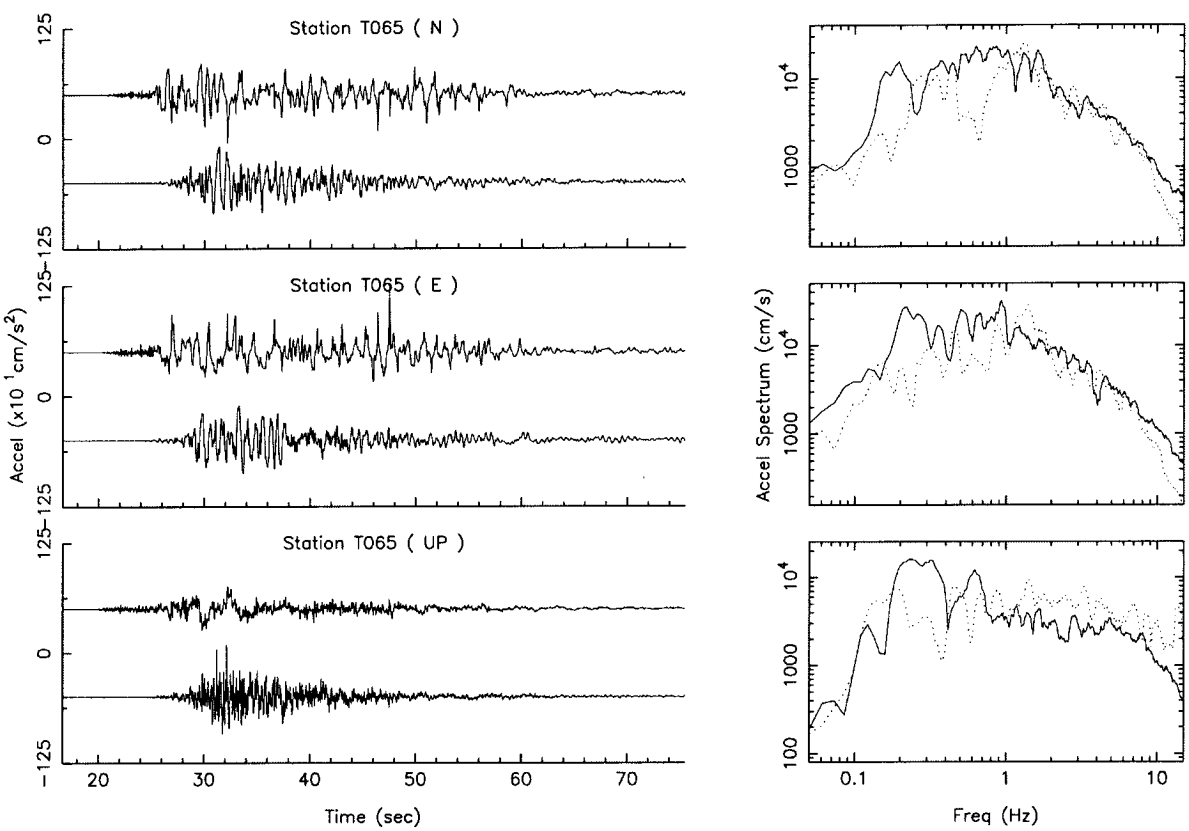

Figure 20. Continue.

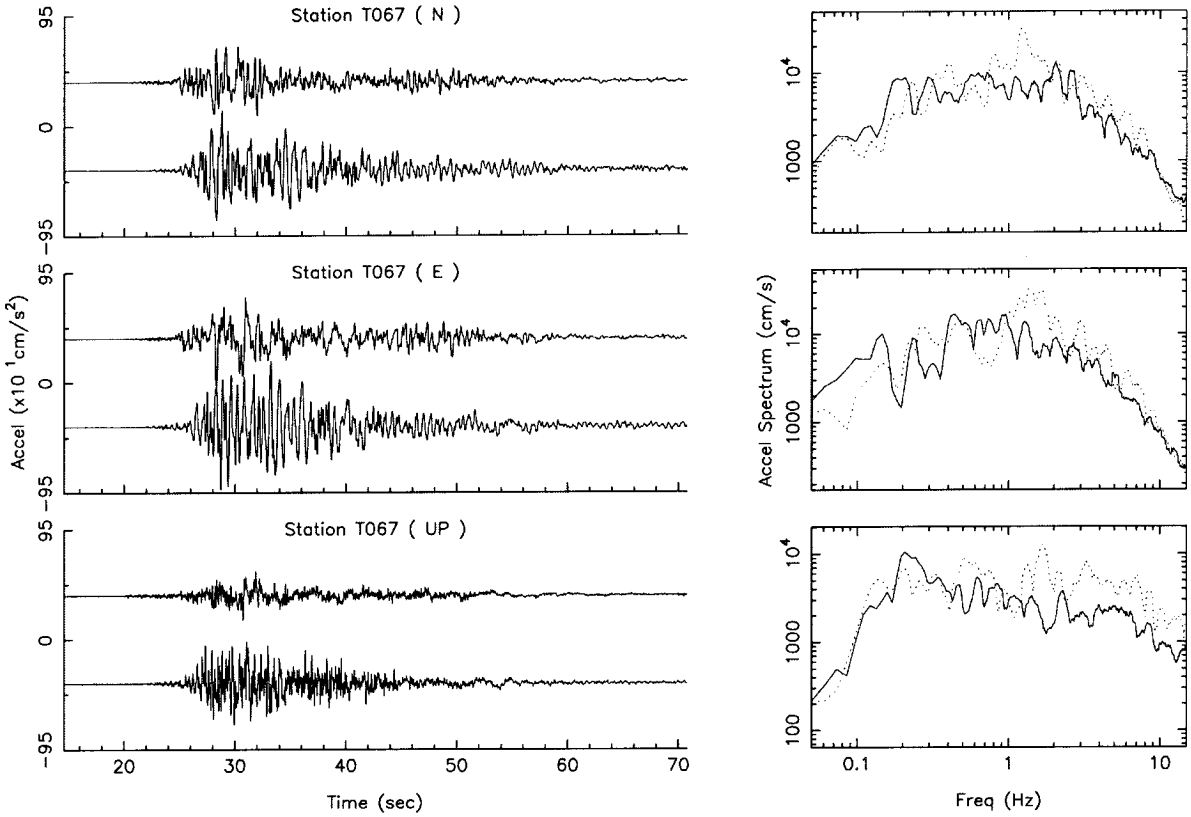

Figure 20. Continue.

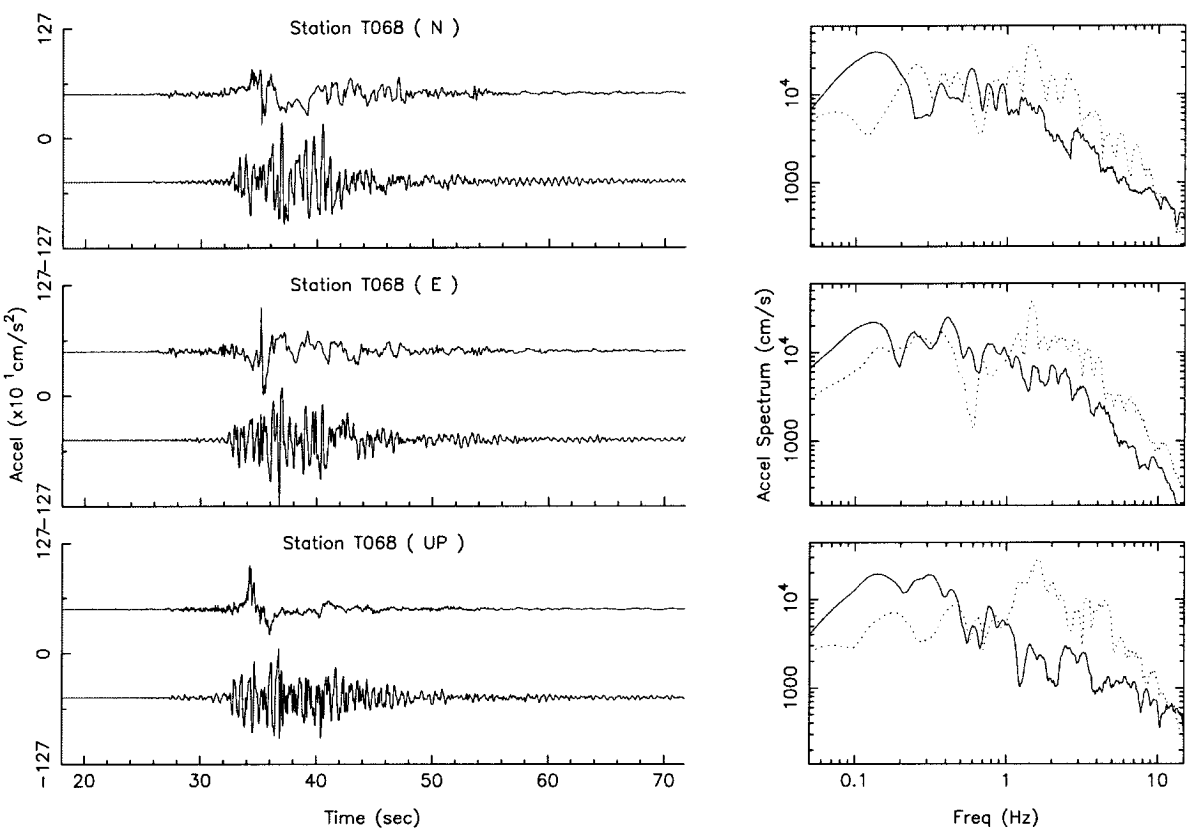

Figure 20. Continue.

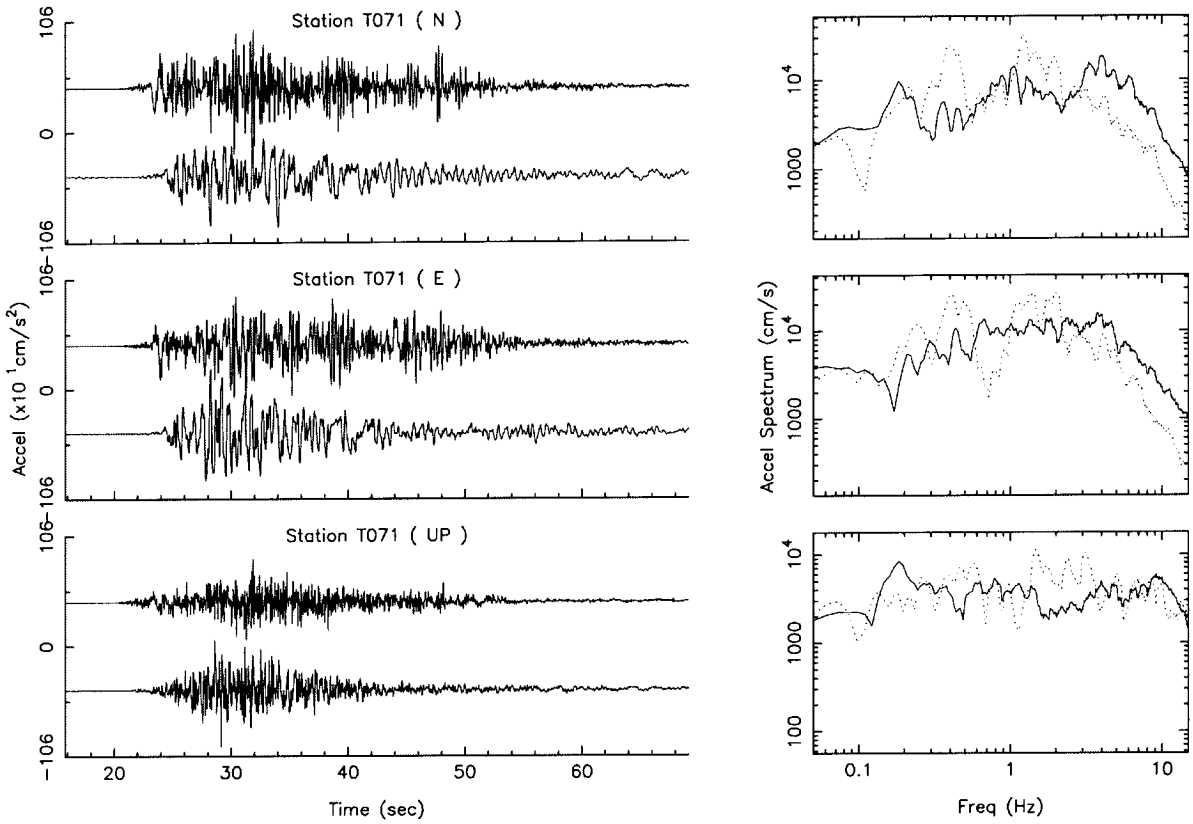

Figure 20. Continue.

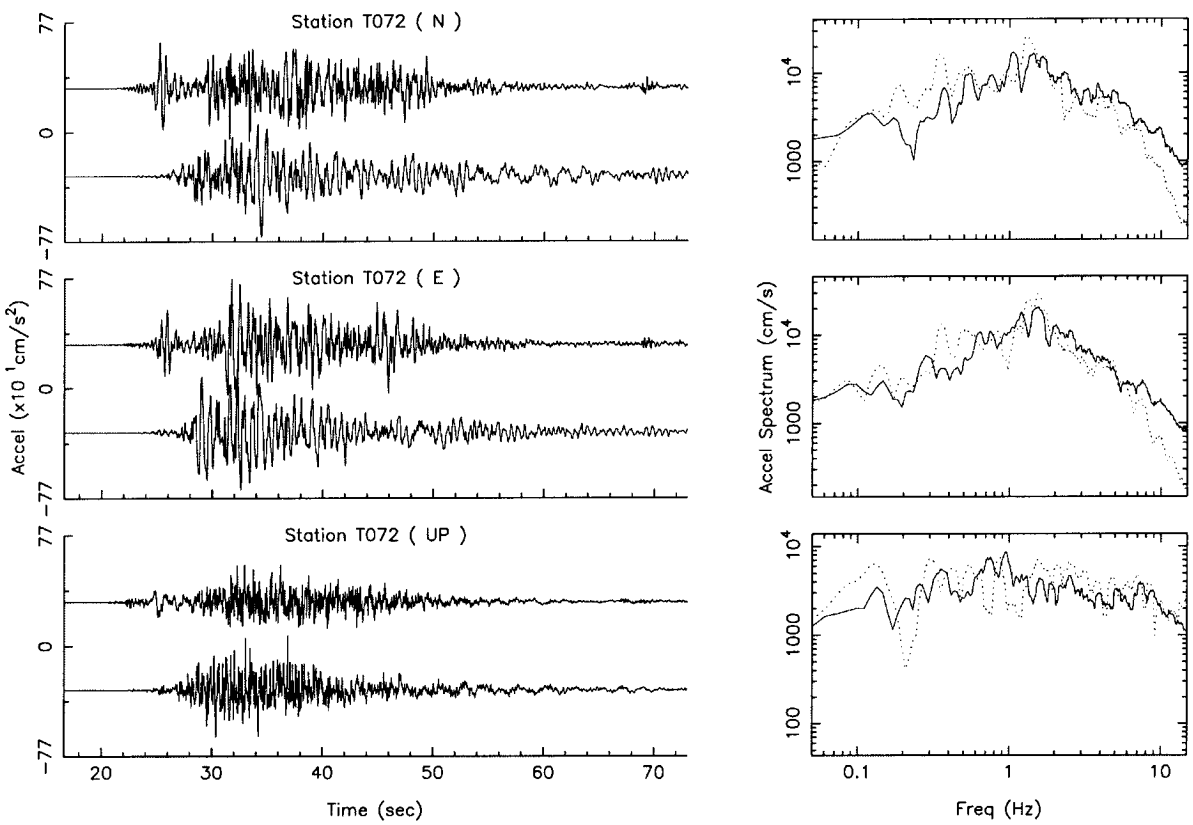

Figure 20. Continue.

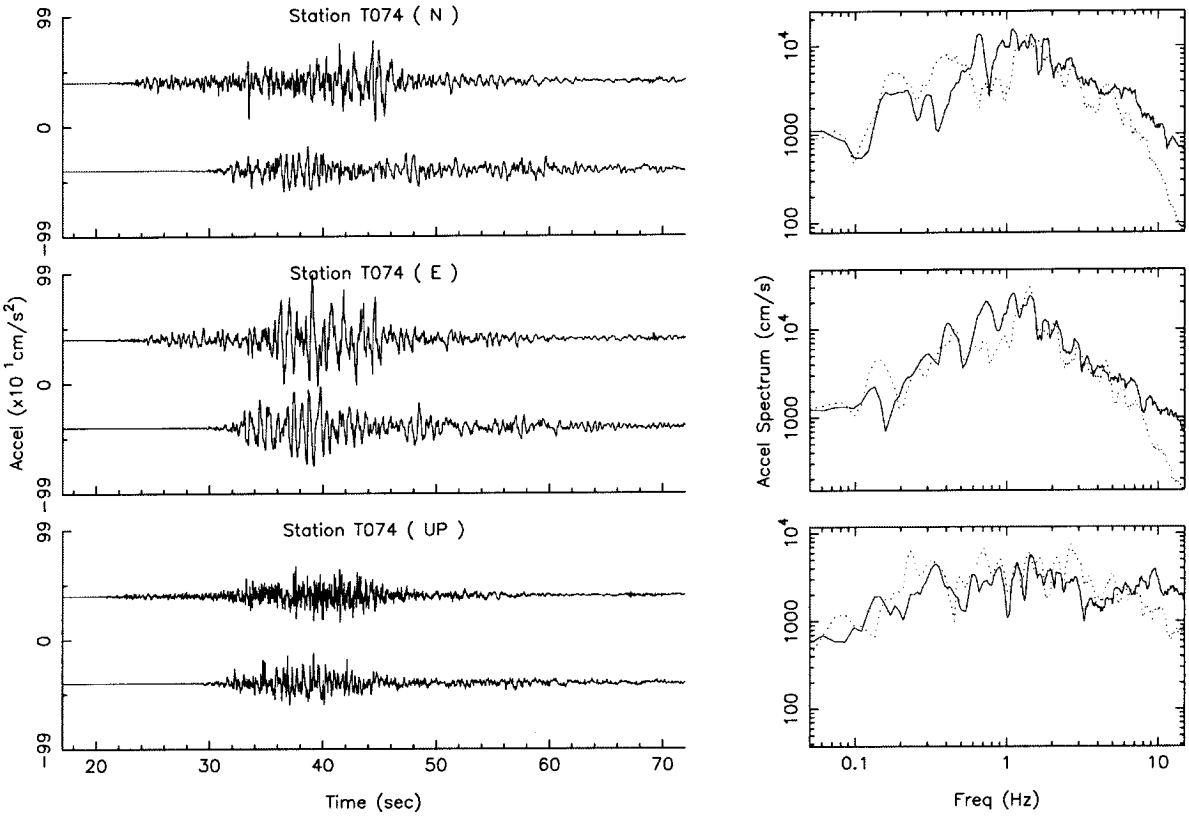

Figure 20. Continue.

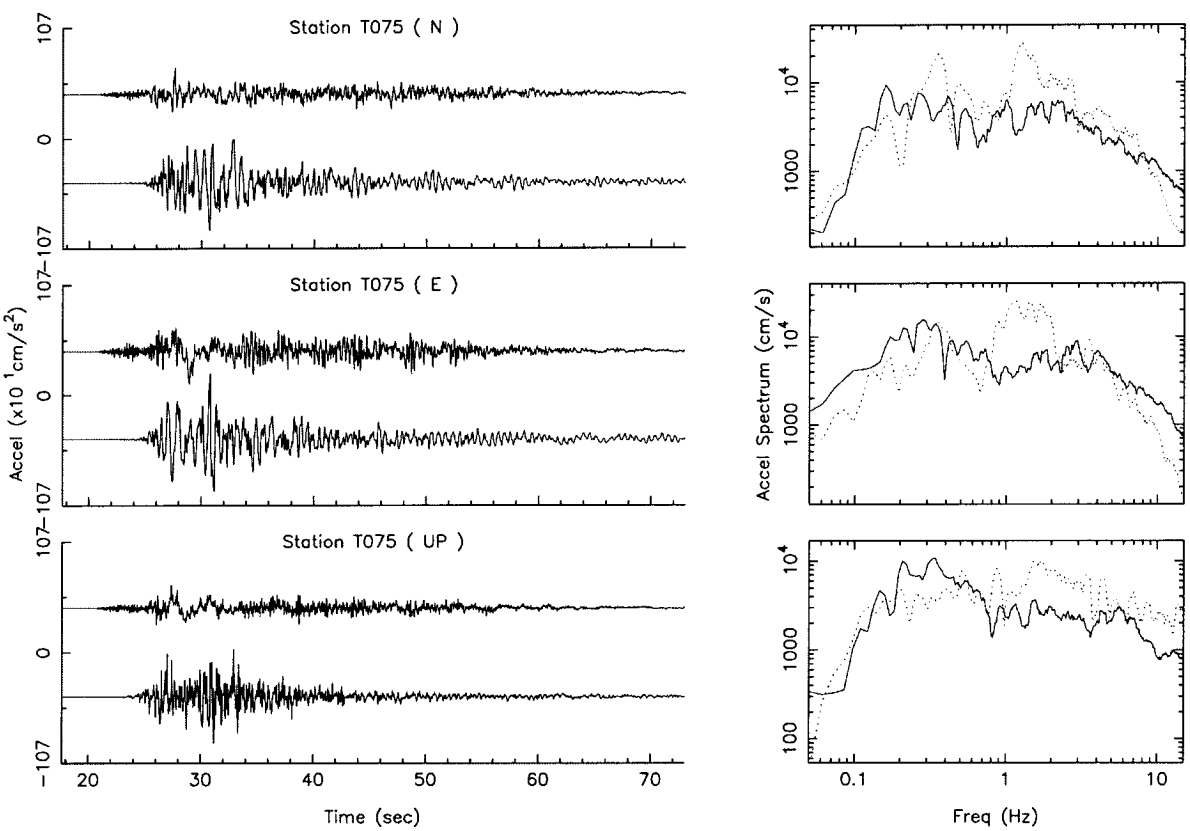

Figure 20. Continue.

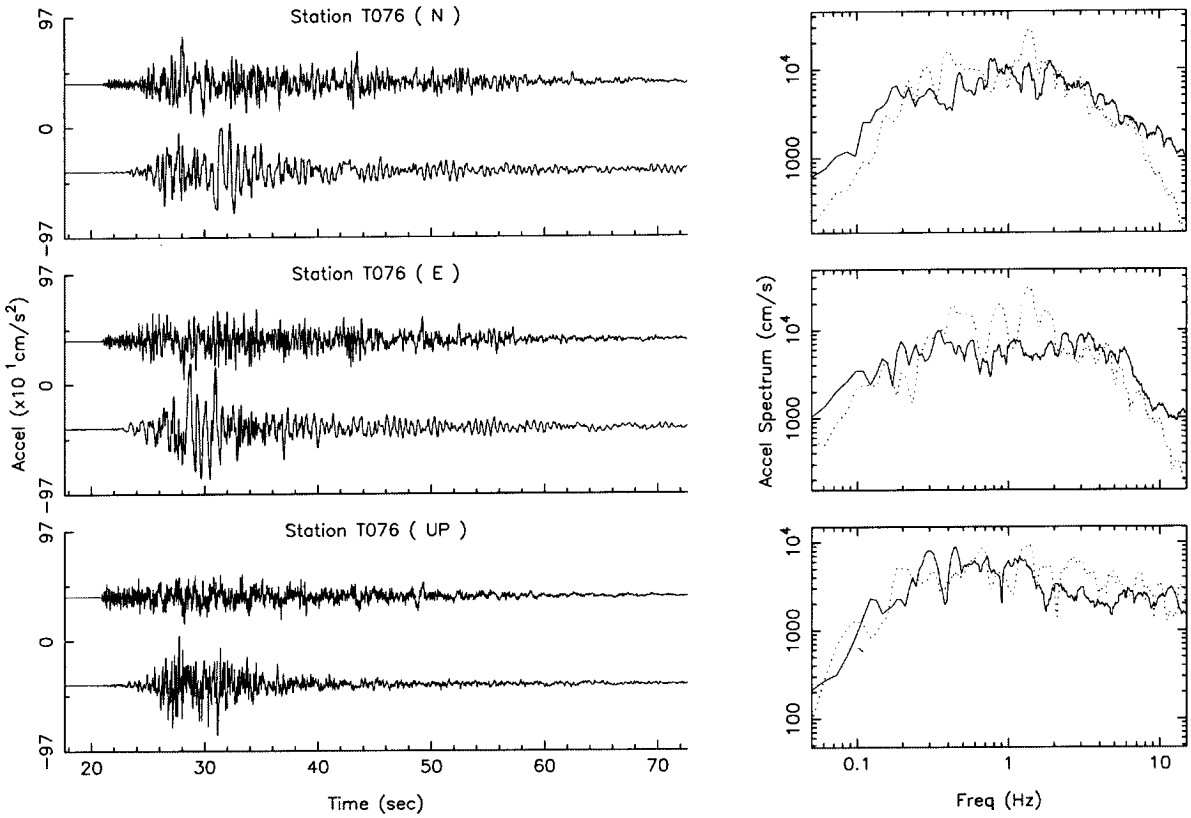

Figure 20. Continue.

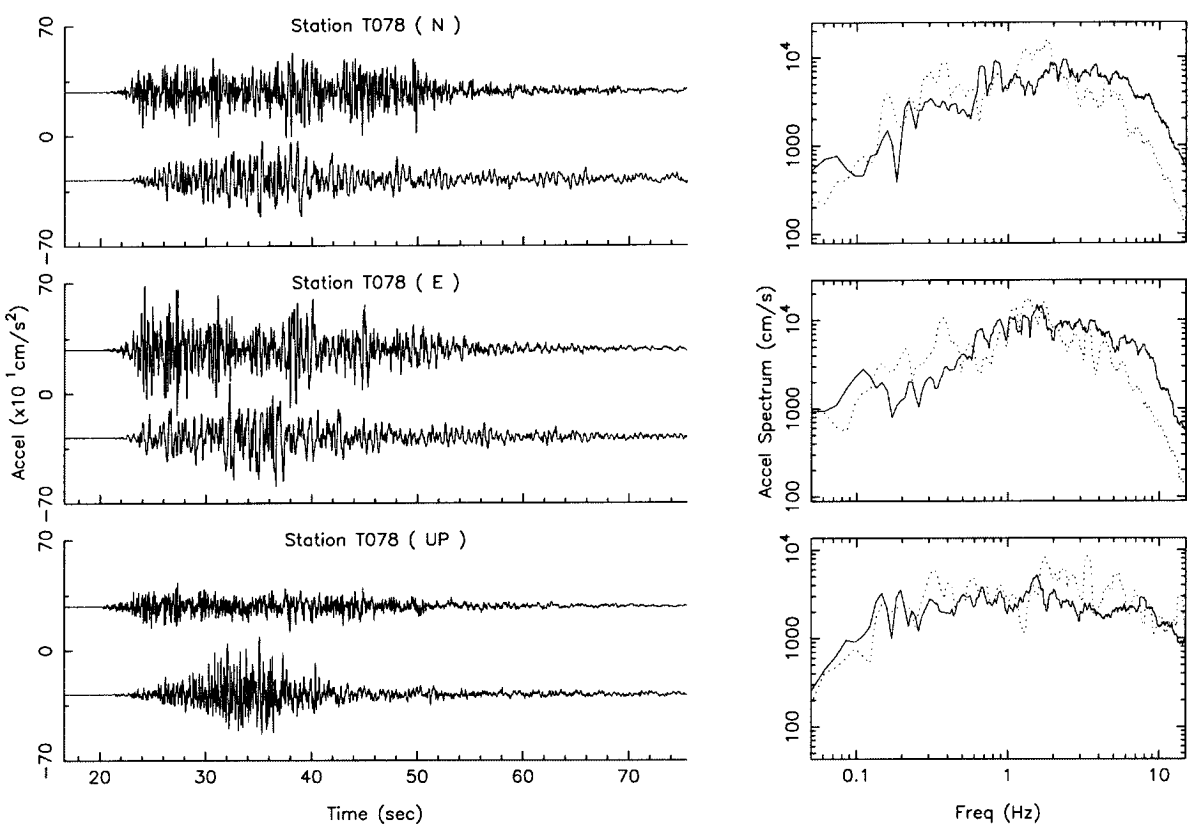

Figure 20. Continue.

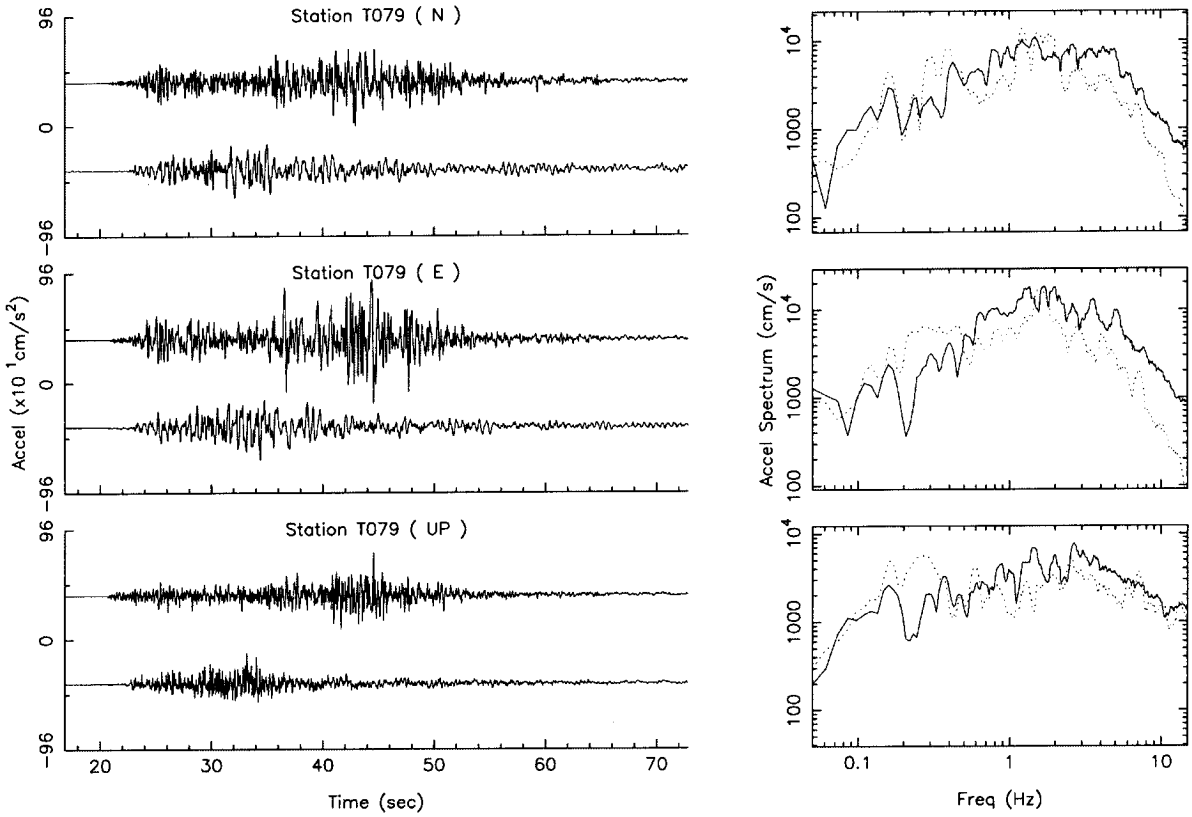

Figure 20. Continue.

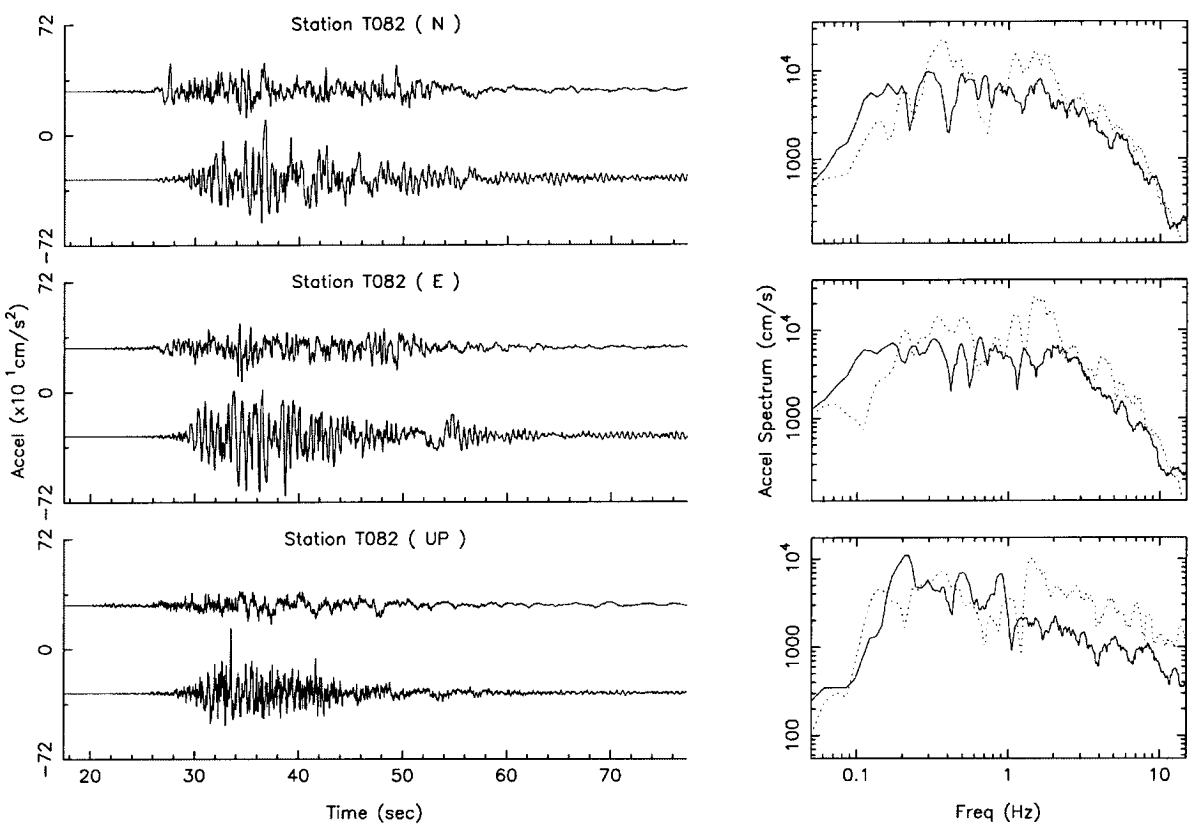

Figure 20. Continue.

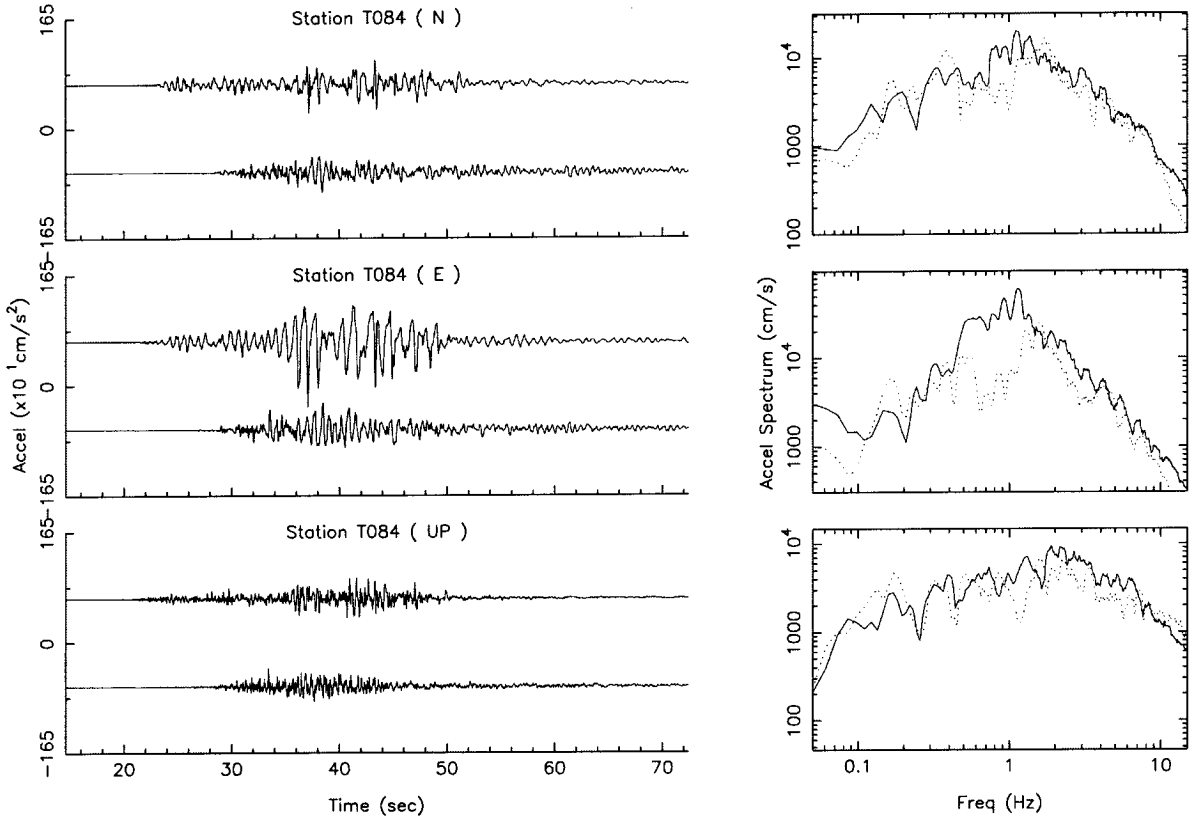

Figure 20. Continue.

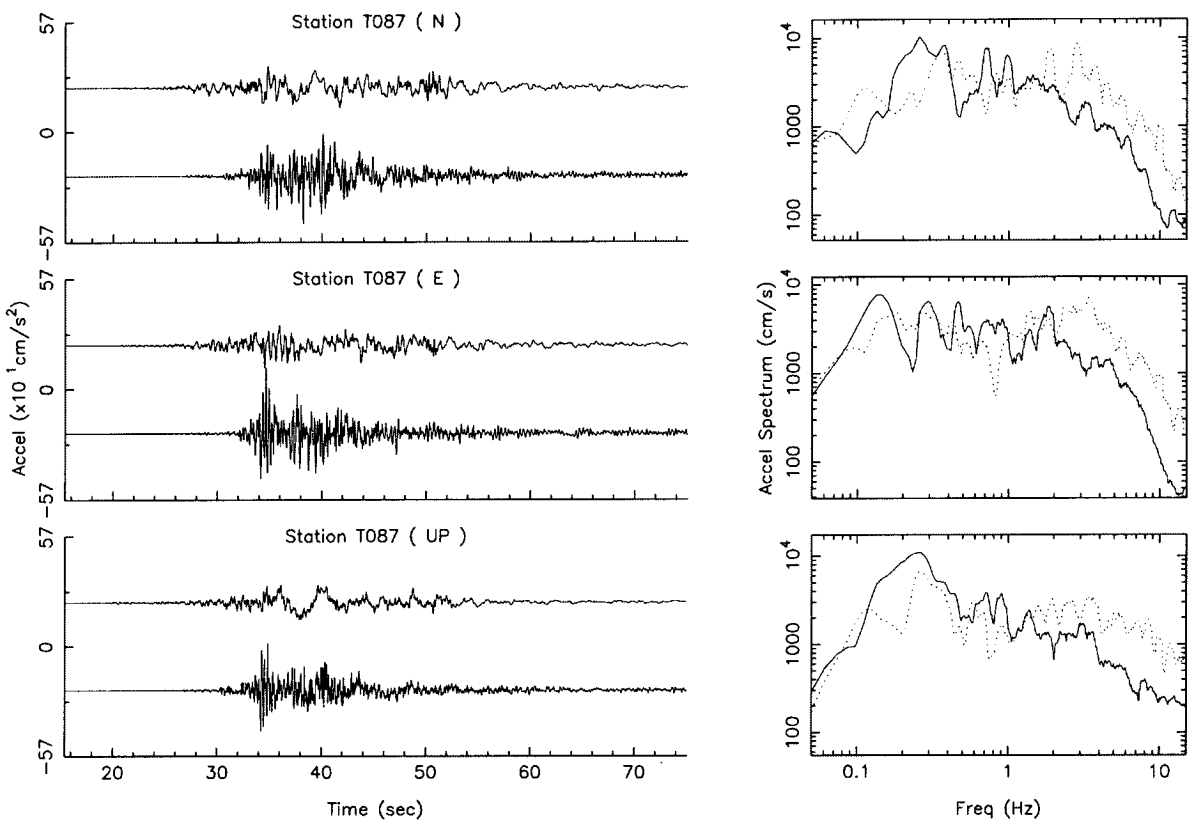

Figure 20. Continue.

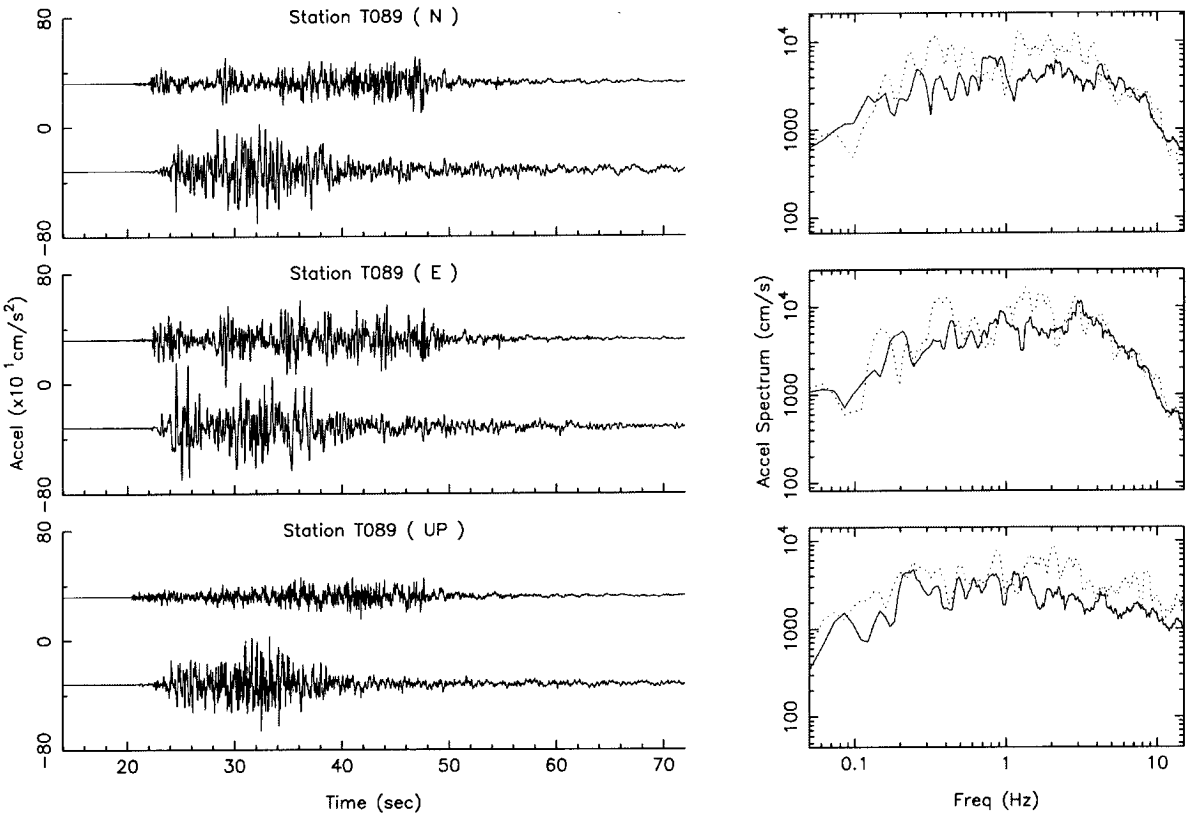

Figure 20. Continue.

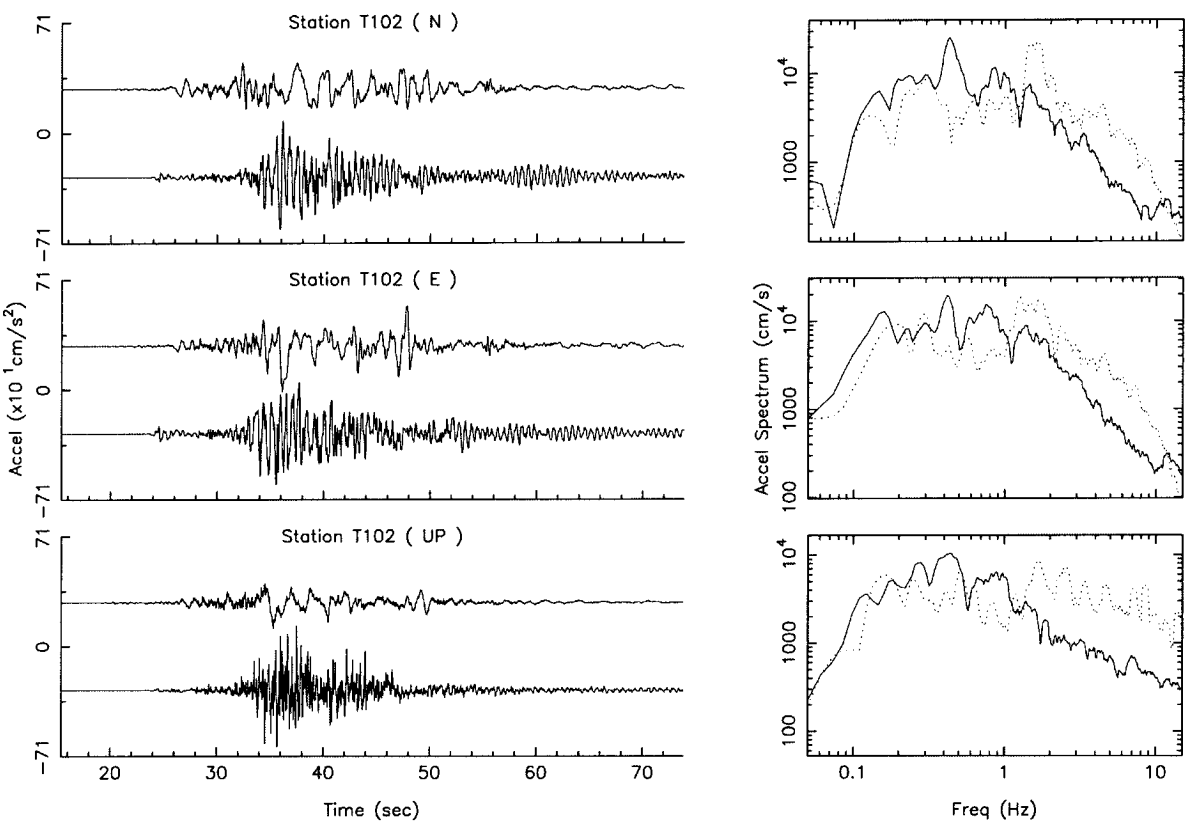

Figure 20. Continue.

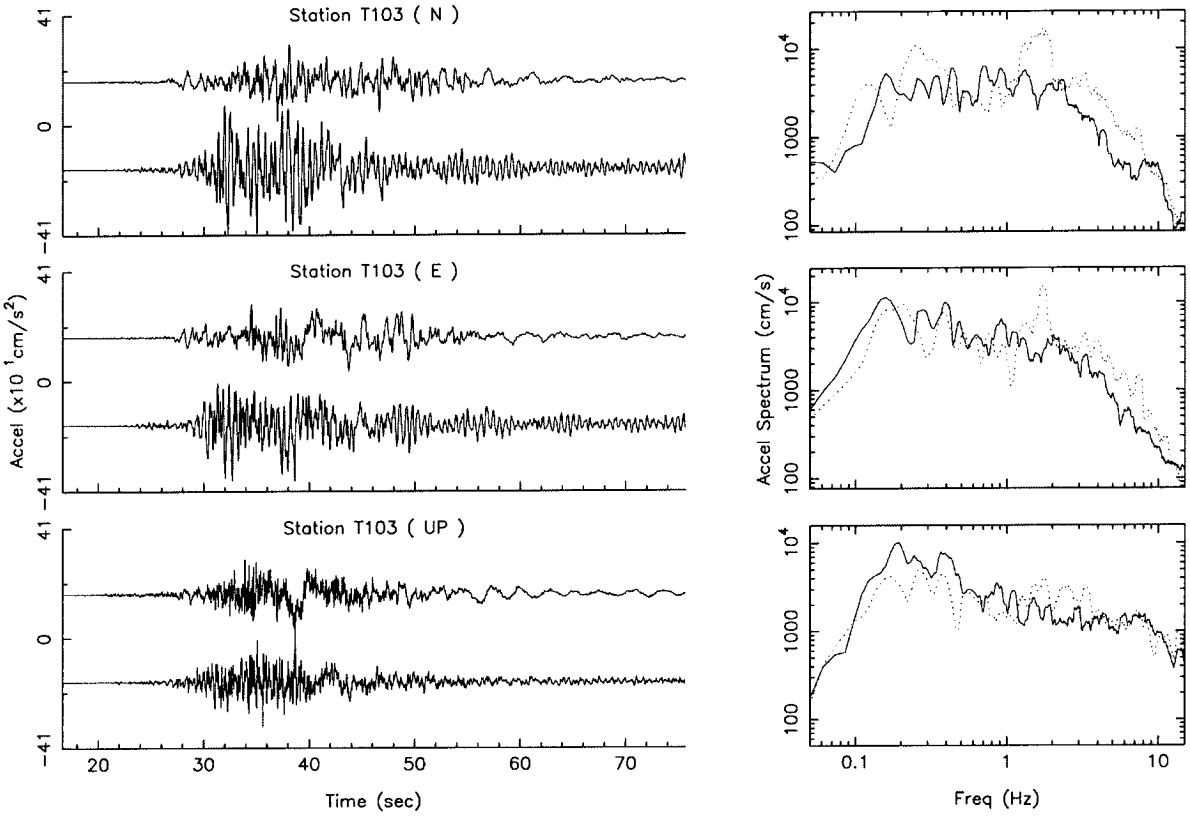

Figure 20. Continue.

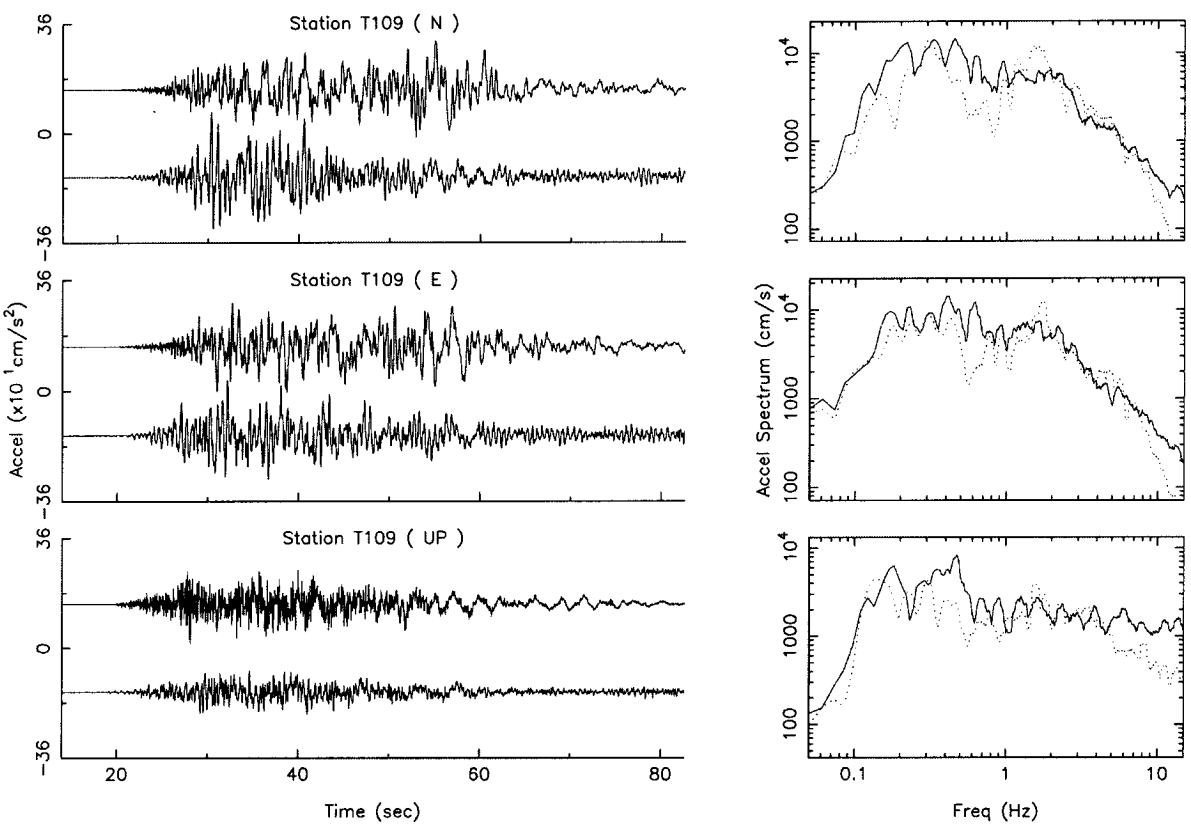

Figure 20. Continue.

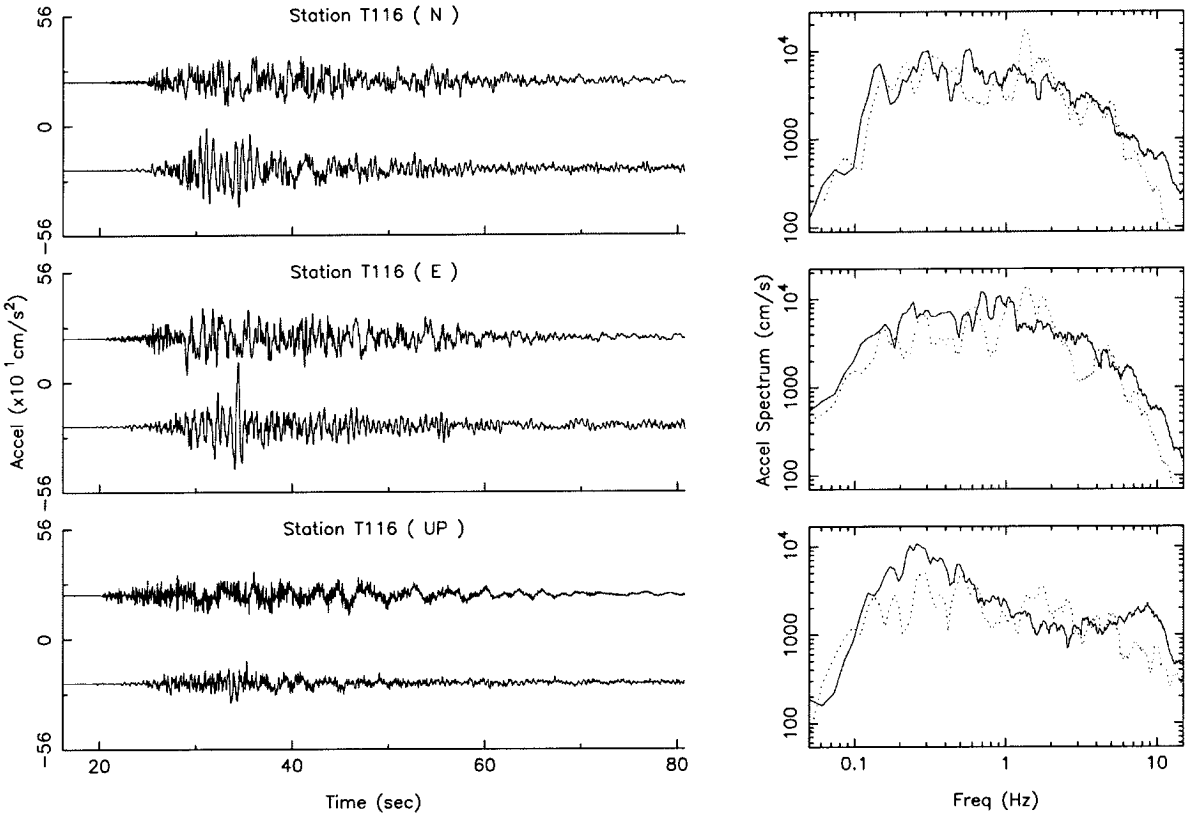

Figure 20. Continue.

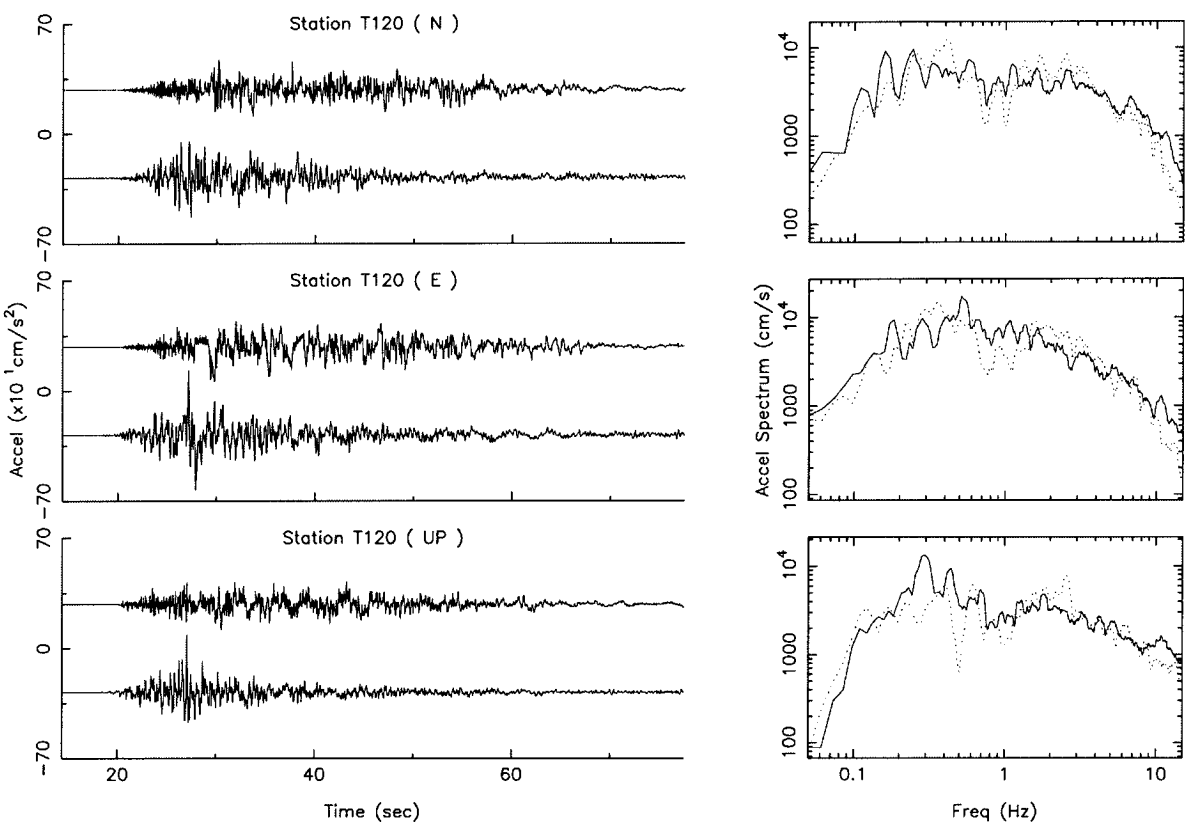

Figure 20. Continue.

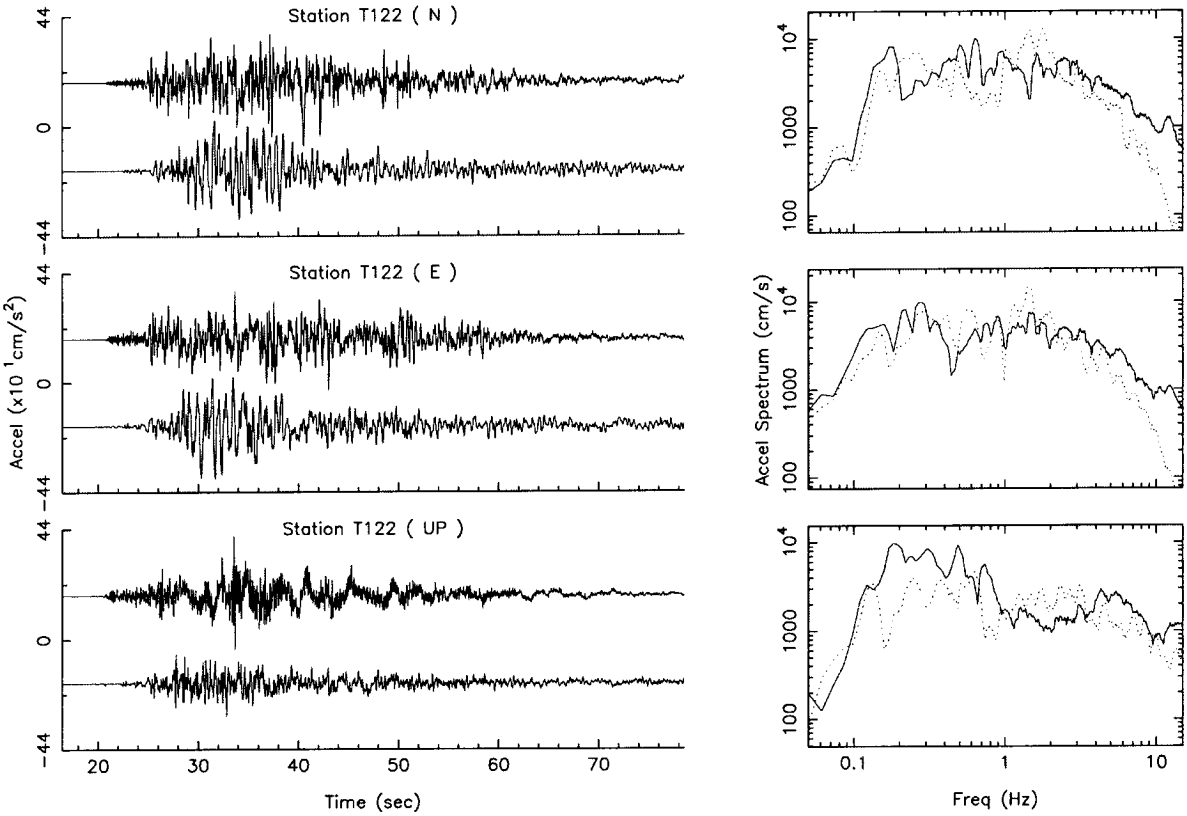

Figure 20. Continue.

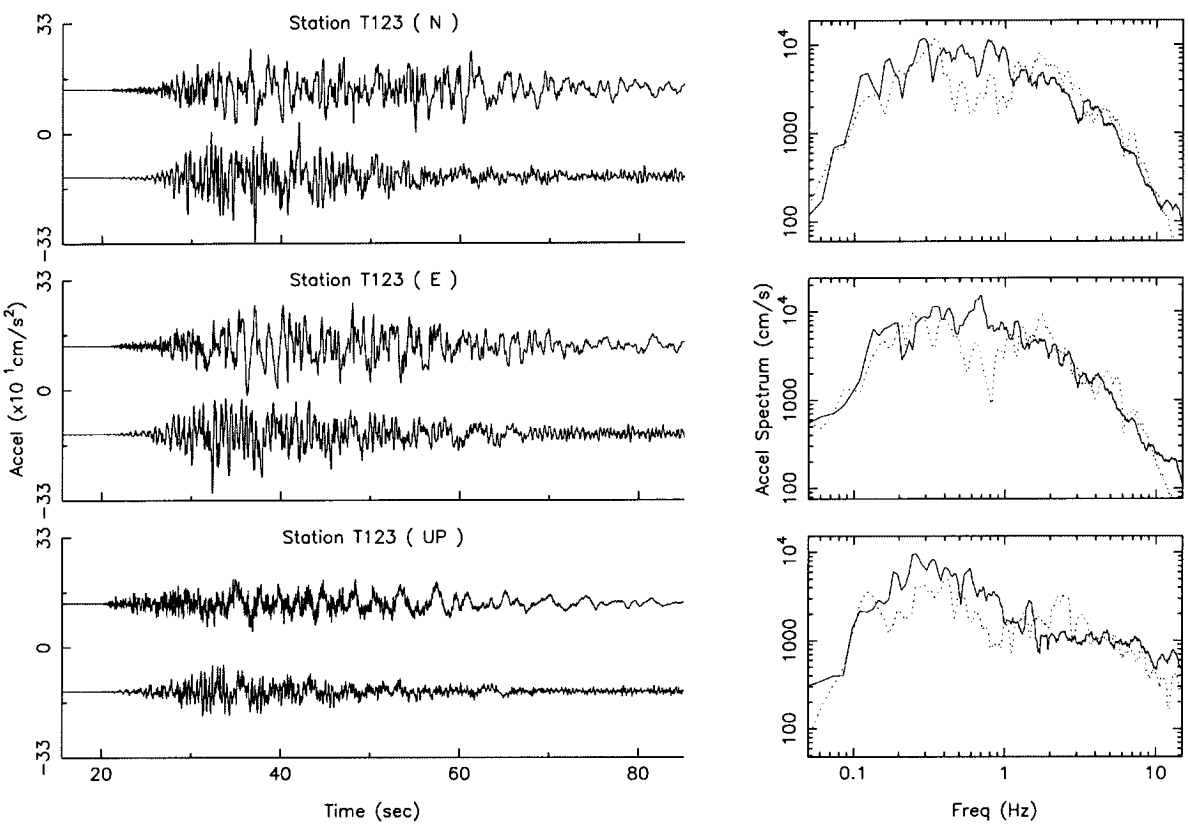

Figure 20. Continue.

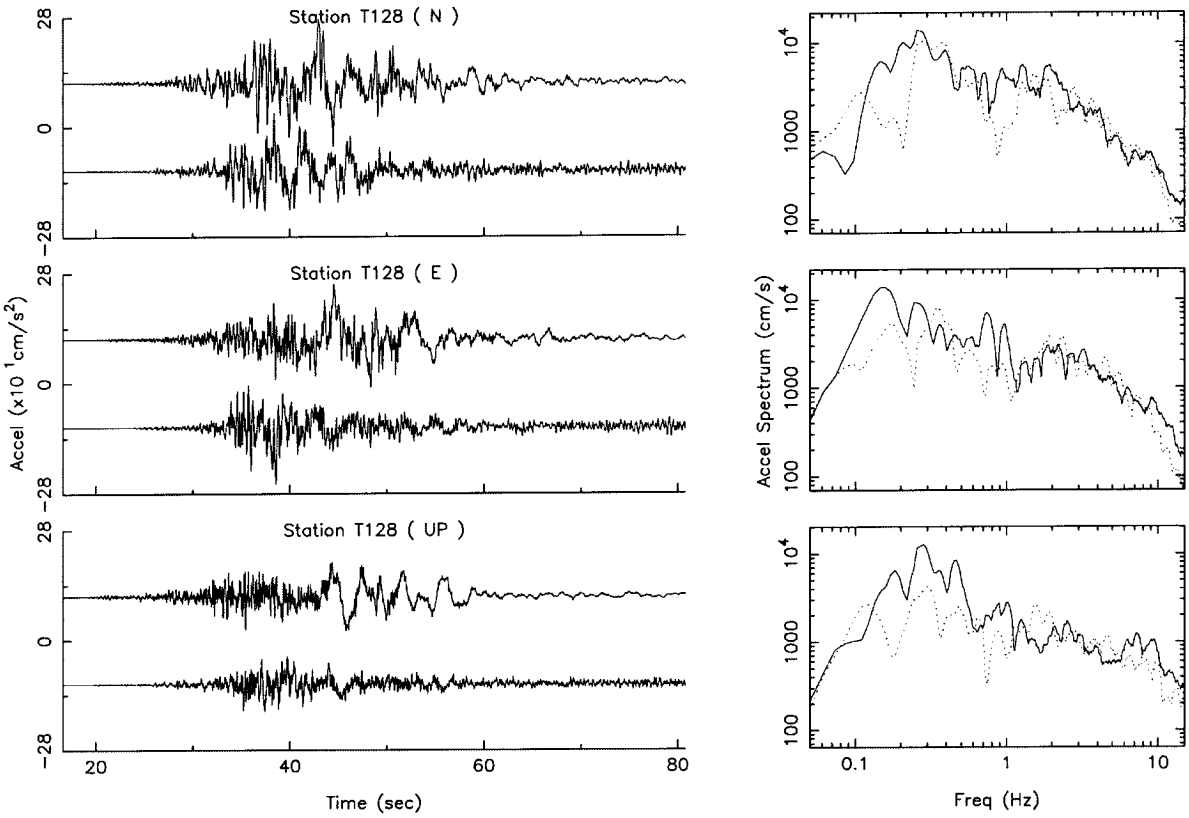

Figure 20. Continue.

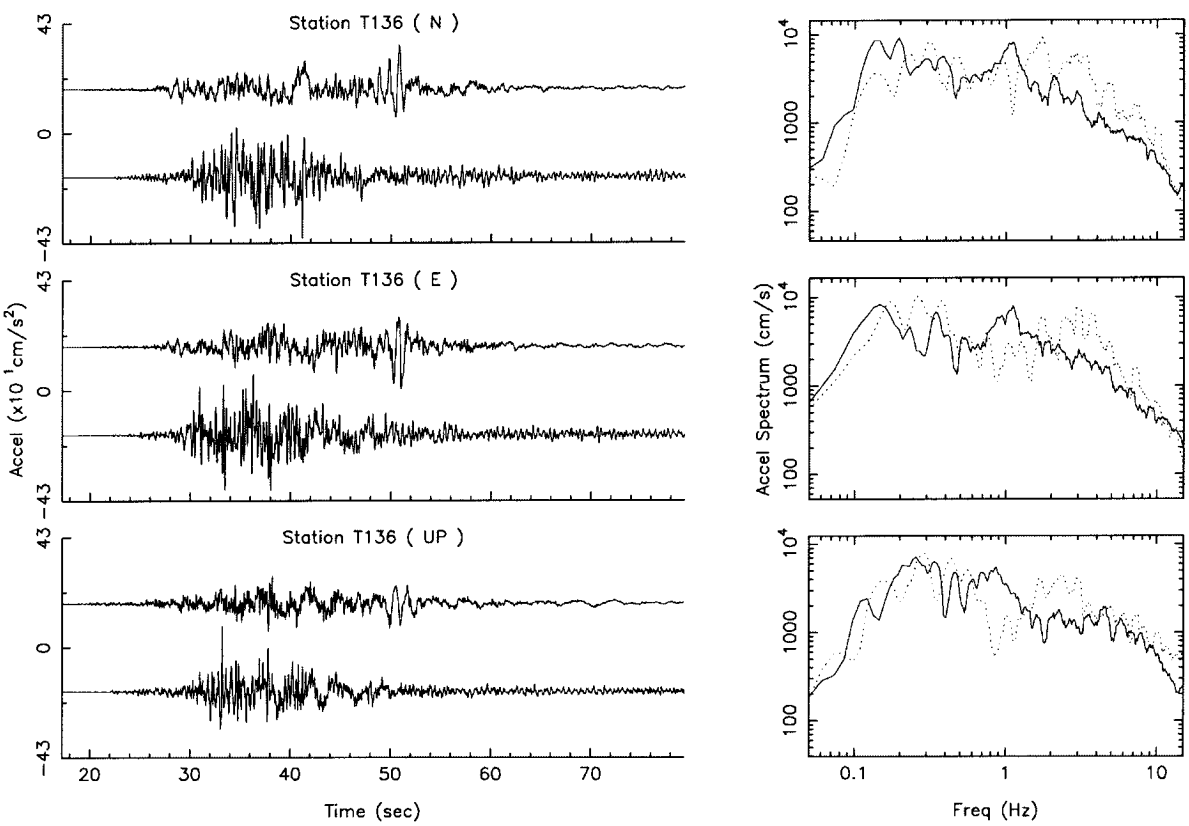

Figure 20. Continue.

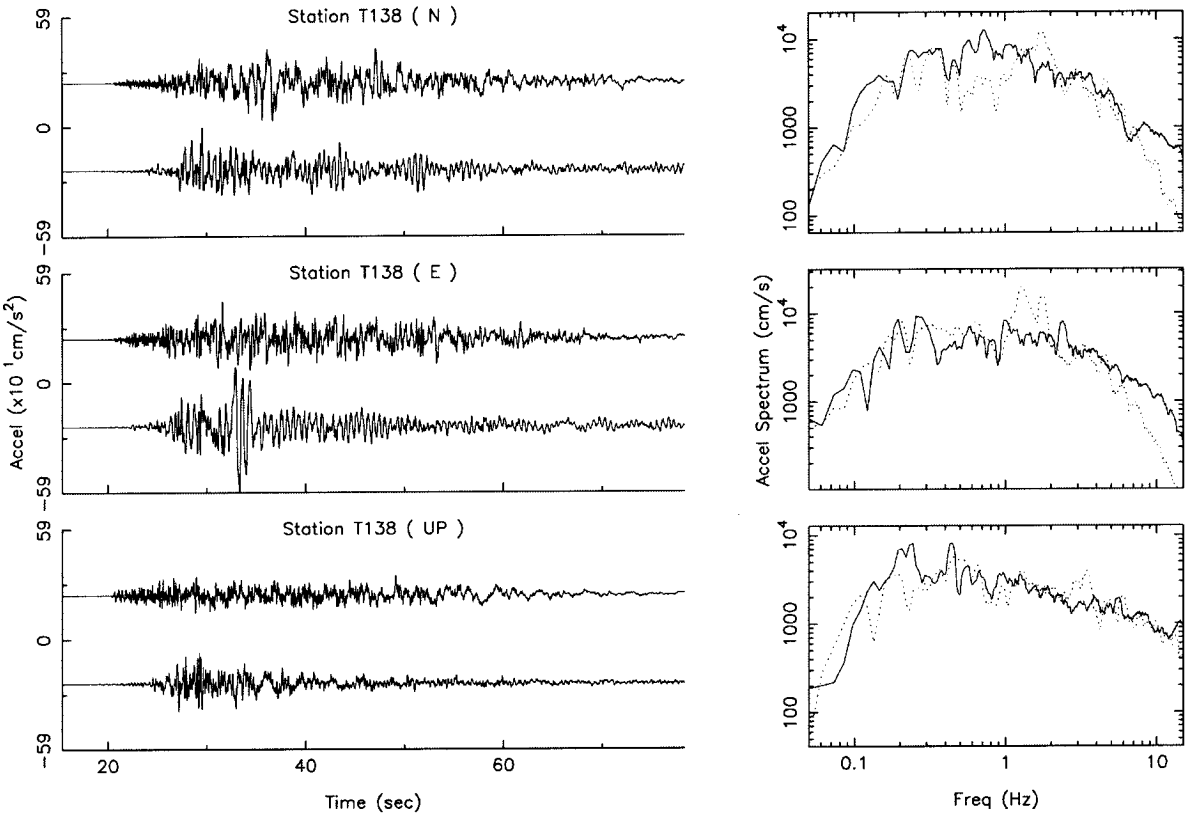

Figure 20. Continue.

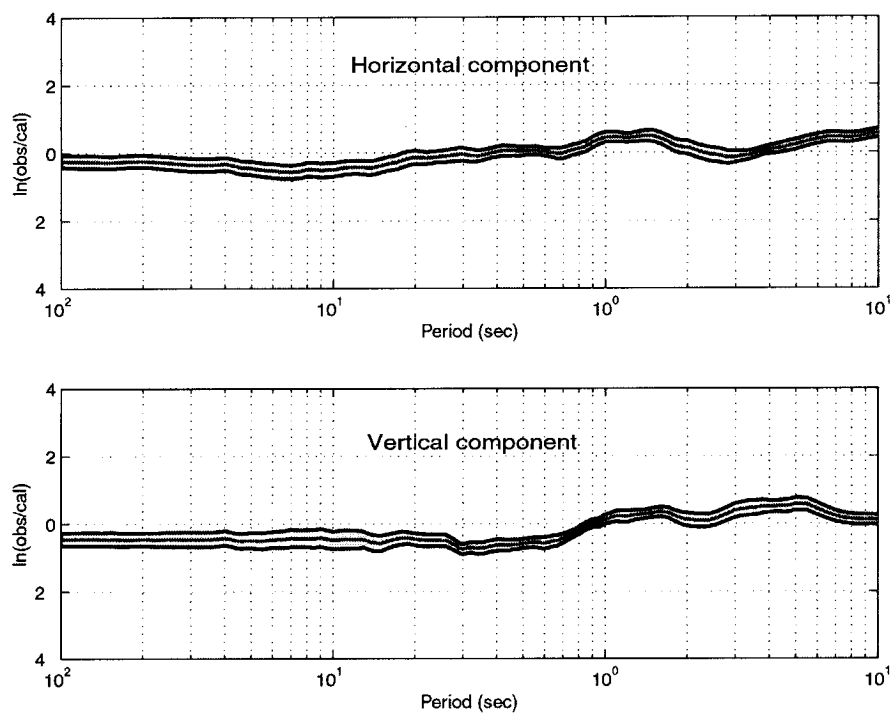

Figure 21. The upper panel plots biases (red) and its 90% confidence limits (black) of the prediction for the horizontal component. The lower panel plots that for the vertical component.